Enriching architectures for biosensing and motor-filament systems through the programmability of DNA

Thesis by

Matteo Michele Guareschi

In Partial Fulfillment of the Requirements for the
Degree of
Doctor of Philosophy

CALIFORNIA INSTITUTE OF TECHNOLOGY
Pasadena, California

2025
Defended January 27th 2025

Matteo Michele Guareschi
ORCID: 0000-0002-5197-3158

ACKNOWLEDGEMENTS

I have felt the support of my advisor, Paul Rothemund, before I even met him, from his first email to me. The way he approaches even the most minute experimental hiccup with the same passion he shows for the large picture scientific questions has shown me the key to unlocking true understanding and discovery. Good people are more important and rare than good scientists, and I will always be grateful to Paul for creating a supportive and engaging environment, in a way that was apparent both in front of my rushed slides on the projector and in front of World Series-worthy BBQ.

In the wonderful community of our super group I found two more mentors in Lulu Qian and Erik Winfree. Lulu is a model of how to do incredibly thoughtful, but also beautiful science, making research shine and reaching a much wider audience through a universal language. Erik has shown me how to do reasoned, thorough science, one that often does not need an experiment to answer a question. Having their constant input and perspective has been an absolute joy and a highlight of my work.

Working in a smaller research group can be socially challenging, and doing it over the lockdown years could have amplified that. If that was not my experience, it is entirely thanks to Olivia Zou, as we shared our ups and downs throughout the last five years. Together, we graduated from grueling problem sets to just as grueling layouts of Bananagrams tiles. She is an engaging lab mate, a thoughtful friend, and a wonderful human.

Among my first mentors in science were the members of the Rothemund lab that welcomed me six years ago. Byoung-jin Jeon, who taught me all the techniques in the lab and patiently explained and corrected all my mistakes. Mentors like him are rare, and I am very aware of how lucky I have been, thank you. Jaimie Marie Stewart has been an incredible example in dedication and determination, in making one's own fortune and achieving anything she set out to. Vishal Maingi showed me how to be an independent thinker and scientist, and how to thrive scientifically through the obstacles of bureaucracy.

I want to acknowledge the DNA nanotechnology community at large for creating such a welcoming and collaborative environment. This is where I was born academically and scientifically and I did not realize how different other fields can be until I stuck

my nose out. During my studies, instead, I have never been afraid to reach out for a collaboration or to share my results, and I owe it to the wonderful people I collaborated with and to everyone else in the field.

For the first few years in graduate school I struggled to reconcile my life in an extremely supportive research group with the experience of many of my friends. I finally found an outlet for that by joining our Graduate Student Council. Meeting a group of people that were already working selflessly to improve the life of graduate students was a pleasant diversion from the forcibly self-centered life of scientific research. I learned so much about activism, diplomacy, negotiation, and so much more from people that were as incredibly passionate as they were effective, but I also found a group of friends. Rachael, Melissa, Matt, Sahangi, Anne, Seneca, Levi. This work is never easy and it is most often thankless, but I hope that younger students will be inspired to keep it up.

It takes a village to raise a graduate student and I relied more than I let on on the support system I found around me. The Sotto Troie team, Khalil, Linlin, Mike, and Tom, a group of friends that is worth its weight in overly chewy pretzels and very unlikely SGV eats. All the other Flubber Ducks, Andy, Drew, Laura, Victor, who got me out the house and into a unicorn floatie, among the many adventures. Martin, who became a way better tennis player than I ever was, for some incredible food and being, I have to admit it, very good at games. Tess who is never around, but always there in a way very few are.

There is a common thread in everything I have done throughout the last few years, one person has inspired it all, she has pushed me to grow, she has challenged and supported me at every step. Thank you, Victoria.

The support system extended over a continent and an ocean to my closest friends, Enri, Gio, Jaco, Petro, Luca, Micaela; with them home is still home. The support of my family, my parents and my brother, has been generous and tireless, throughout many years and many countries. The more I grow up, the more I realize how hard their job has been, and how I owe everything I am to them.

ABSTRACT

Since its inception, the field of DNA nanotechnology has focused on studying the fundamental behaviors and capabilities of engineered nucleic acids. A deep understanding of this toolkit has enabled advancements in several fields, for research tools and in translational applications. Together with its programmability and nanometric resolution, the great promise of DNA nanotechnology lies in the incorporation of structure and function in a single molecule. In this work, we show how these advantages can be leveraged to expand the capabilities of two different systems: a sensor for biomarkers and a motor-filament architecture. During our exploration, we also discover and work to overcome some of the less obvious limitations of the technology, shining light on more foundational questions.

We demonstrate an electrochemical biosensor based on a DNA origami that can detect and quantify nucleic acids and proteins in a package easily adaptable to different analytes by simply replacing the binder molecules. Upon target binding, the structure undergoes a large conformational change, bringing a multitude of redox reporters to the electrode surface where an electric current can be measured. The high number of reporter molecules on a single detector results in improved signal gain per binding event, allowing for the detection of low analyte concentrations, while the conformational change yields an unprecedented gain between the off and on state. We demonstrate how the system can be readily adapted to different analyte molecules and reused over several cycles to analyze multiple samples. We then run simulations of the detector molecule to understand structural deformations intrinsic to this design, in order to optimize the number and placement of the redox reporters. We discover and investigate a phenomenon that causes significant curling of the DNA origami, possibly limiting the contribution of many of the reporter molecules. We explore experimental directions to mitigate the issue by changing the configuration of the redox molecules and by designing stiffer sensors.

We then set out to integrate DNA origami-based nanostructures with an engineered dynein protein that can bind to and kick double-stranded DNA instead of tubulin. Motor-filament architectures have been studied as the main mechanism for cellular transport and as a system that can exhibit mesoscopic active matter behaviors in biology, but the relative difficulty of engineering microtubules has hindered the exploration of their properties. The high-resolution programmability of DNA nanostructures makes them prime candidates to overcome this obstacle and this

study has been enabled by the recent development of new protein motors where the tubulin binding domain is replaced by a DNA binding domain. We first look at DNA nanotubes, structures that resemble microtubules, but that retain a level of programmability that is typical of DNA nanotechnology. By exploiting the DNA strand displacement technique, we incorporate machinery that enables new behaviors, with a focus on different ways to turn gliding on and off by stopping the DNA nanotubes. We then turn our focus to more complex gliders designed with DNA origami. We explore the space of DNA origami polymers in order to assemble superstructures that can be detected under light microscopy, encountering again issues of deformations due to the addition of overhangs. We then assess the gliding capabilities of DNA origami, designing ways to incorporate motor binding sequences on them, but we find that DNA origami sticks nonspecifically to the engineered dynein motors. After testing several different hypotheses, we gather evidence that this interaction might be caused by the large sequence variability of the scaffold strand in DNA origami, coupled with the recognition of spurious binding sequences by the motor proteins.

PUBLISHED CONTENT AND CONTRIBUTIONS

Jeon*, Byoung-jin, Guareschi*, Matteo M., Stewart, Jaimie Marie, Wu, Emily, Gopinath, Ashwin, Arroyo-Currás, Netzahualcóyotl, Dauphin-Ducharme, Philippe, Plaxco, Kevin W., Lukeman, Philip S., and Rothemund, Paul W. K. (2025). "Modular DNA Origami–Based Electrochemical Detection of DNA and Proteins". In: *Proceedings of the National Academy of Sciences* 122.1, e2311279121, DOI: 10.1073/pnas.2311279121.

* Equal contribution

B.J., M.M.G., J.M.S., A.G., N.A.-C., P.D.-D., K.W.P., P.S.L., and P.W.K.R. designed research; B.J., M.M.G., J.M.S., and E.W. performed research; B.J. contributed new reagents/analytic tools; B.J., M.M.G., and P.W.K.R. analyzed data; and B.J., M.M.G., J.M.S., E.W., A.G., N.A.-C., P.D.-D., K.W.P., P.S.L., and P.W.K.R. wrote the paper.

TABLE OF CONTENTS

Acknowledgements . . . iii
Abstract . . . v
Published Content and Contributions . . . vii
Table of Contents . . . vii
Chapter I: Introduction . . . 1
1.1 A Primer on DNA as a Structural Molecule . . . 1
1.2 DNA Nanotubes . . . 5
1.3 DNA Origami . . . 8
1.4 Motor-Filament Systems in Biology . . . 10
1.5 Engineering Motor-Filament Systems . . . 11
Chapter II: Modular DNA Origami-based Electrochemical Detection of DNA and Proteins . . . 13
2.1 Introduction . . . 13
2.2 Lily pad DNA origami device . . . 18
2.3 Lily pad origami design . . . 20
2.4 Optimizing the number of MB per origami . . . 21
2.5 Chip preparation and electrochemical measurement . . . 23
2.6 DNA detection . . . 24
2.7 Optimizing a Multimeric Protein Detector . . . 25
2.8 Lily pad sensor regeneration . . . 30
2.9 PDGF-BB detection . . . 31
2.10 Discussion . . . 32
2.11 Methods . . . 37
Chapter III: Simulations of Large DNA Origami Structures . . . 48
3.1 Introduction . . . 48
3.2 Simulating DNA Origami with oxDNA . . . 50
3.3 Initial Model Design . . . 51
3.4 Effects of Overhangs on DNA Origami . . . 54
3.5 Effect of Overhangs on Rigid Double-Layer Structures . . . 56
3.6 Explaining the Curling of the Hairygami . . . 58
3.7 Consequences and Experimental Evidence . . . 59
Chapter IV: Expanding the Capabilities of DNA Nanotube Gliders . . . 63
4.1 Introduction . . . 63
4.2 Launch Control . . . 65
4.3 Halting Gliding . . . 74
4.4 Releasing DNA Nanotubes . . . 75
4.5 Discussion . . . 86
4.6 Methods . . . 87

Chapter V: Towards Robust Gliding of Arbitrary DNA Nanostructures on Engineered Motor Proteins 90
5.1 Introduction 90
5.2 DNA Origami Arrays 93
5.3 Designing a Boundless 1D DNA Origami Array 94
5.4 Tubular origami design 98
5.5 Effect of single-stranded DNA domains 102
5.6 Specificity of binding sequence recognition 103
5.7 Discussion 105
Chapter VI: Conclusions 108
Bibliography 112
Appendix A: Square wave voltammetry 124
Appendix B: Notes on translating electrical currents to concentrations 125
Appendix C: Synthesis of double-stranded DNA linkers for lily pad stalks . . 127

Chapter 1

INTRODUCTION

The overly ambitious goal of this chapter is to serve as an introduction to DNA nanotechnology and my thesis work, meant to prepare a layperson who has heard of DNA as the molecule of life for swarms of DNA nanomachines and fields of DNA lilypads.

DNA nanotechnology is a peculiar field that encompasses a large space in a Venn diagram that includes biology, chemistry, physics, computer science, and more depending on the desired application. This is reflected in the different affiliations and backgrounds of the members of the amazing and tight-knit community of scientists I have met in the last years. As an electrical engineer turned bioengineer, I have struggled to describe my work to my colleagues and friends in a way that was relevant to biological research. And similarly, it took me some time to become acquainted with a world that was so far from the silicon chips I knew.

1.1 A Primer on DNA as a Structural Molecule

Ned Seeman is credited as the first person to think of DNA not just as the molecule of life, but as a building block that could be used to design physical structures that are unrelated to its role in the central dogma. From a structural tool, DNA nanotechnology was expanded to dynamic design: reconfigurable molecules capable of computation, data storage, and sensing.

We will start by describing the two pillars of structural DNA nanotechnology and dynamic DNA nanotechnology, respectively the Holliday junction and the DNA strand displacement reaction. These two concepts originated an entire field and, more modestly, they are behind much of the research and discoveries that we will present in the next chapters of this work.

Holliday Junction

The Holliday junction was proposed in 1964 (Holliday, 1964) as one of the first deviations from the canonical double helix structure of DNA. Holliday hypothesized that this junction could be found in recombination mechanisms in fungi, in order to explain a phenomenon called gene conversion where one allele would appear

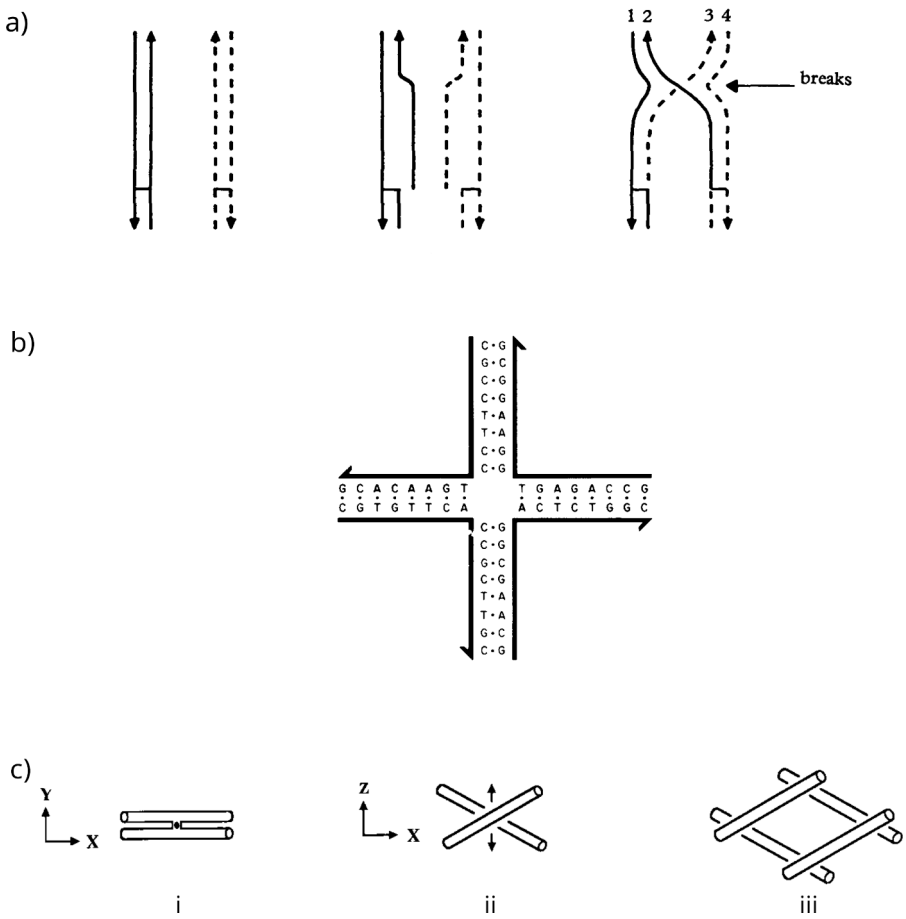

Figure 1.1: a) Original model of a Holliday junction for DNA recombination in fungi, showing how two double helices with similar sequences can recombine into a four-strand complex, with a Holliday junction in the middle. Reprinted with permission from Holliday, 1964. b) Design of a stable artificial Holliday junction with oligonucleotides. The stability of the junction comes from using completely different sequences for the four arms, which makes the initial configuration of two separate double helices seen on the left in a) impossible, as these strands are not pairwise complementary. Reprinted with permission from Seeman, 1982. c) Holliday junction as seen on the xy plane (i) and on the xz plane (ii), showing a 60° angle between helices. (iii) Rhomboidal motif used as a building block for larger lattices. Reprinted with permission Mao, Sun, and Seeman, 1999. Copyright 1999 American Chemical Society.

three times, while the other one only once. As shown in Figure 1.1a, two duplexes of similar sequence A1-A1* and A2-A2* might recombine into A1-A2* and A2-A1*. This process would start with a few basepairs of both complexes breaking up and recombining through the other complex, temporarily forming a four-strand structure with a junction in the middle. From two separate and seemingly inert DNA

duplexes, we obtain a single molecule where each strand bridges over to a different one, creating a junction between them. The reaction could then proceed and the new complexes A1-A2* and A2-A1* could separate and open the junction again, but we will stop before this step for the scope of this work.

It took several years before experimental evidence of Holliday junctions became available through electron microscopy (Doniger, Warner, and Tessma, 1973), and Holliday's model of recombination was updated in Meselson and Radding, 1975 by introducing the concept of branch migration, which we will describe in Section 1.1. Seeman, 1982 envisioned how such a junction could be designed as a stable complex formed by synthetic oligonucleotides, instead of as a temporary product of biological DNA recombination and a year later the first artificial Holliday junction was demonstrated (Kallenbach, Ma, and Seeman, 1983). This work opened the door to larger designs of DNA lattices and other types of junctions, birthing the entire field of DNA nanotechnology. The importance of this construct as the cornerstone of the field lies in the idea that it can be used to combine more than two DNA strands in a shape that goes beyond the canonical double helix: as we bring together two molecules to form one, we can do the same with four, or maybe even two hundred, as we will see in DNA origami.

Before moving on to larger complexes, the structural properties of the Holliday junction need to be investigated more in depth. Of particular interest is the angle between the two helices, shown as 0° in the parallel conformation of the original model in Figure 1.1, and experimentally measured to be 60° in the stacked configuration in Duckett, Murchie, and Lilley, 1990; Mao, Sun, and Seeman, 1999; Zettl et al., 2020 or closer to 40° in Eichman et al., 2000; Watson, Hays, and Ho, 2004. While the literature is not unanimous on a single value, an angle of 60° seems to find more of a consensus. For the purpose of our discussion, the most interesting feature here is that the angle is rigid enough to be consistently measured (within a given experiment) and to yield well-formed lattices, meaning that the Holliday junction can be used as a structural building block to confer rigidity to DNA nanostructures. Conversely, it is flexible enough to warrant a degree of freedom when designing these structures, often releasing the stress of these constraints as twist or torsional strain on a larger scale.

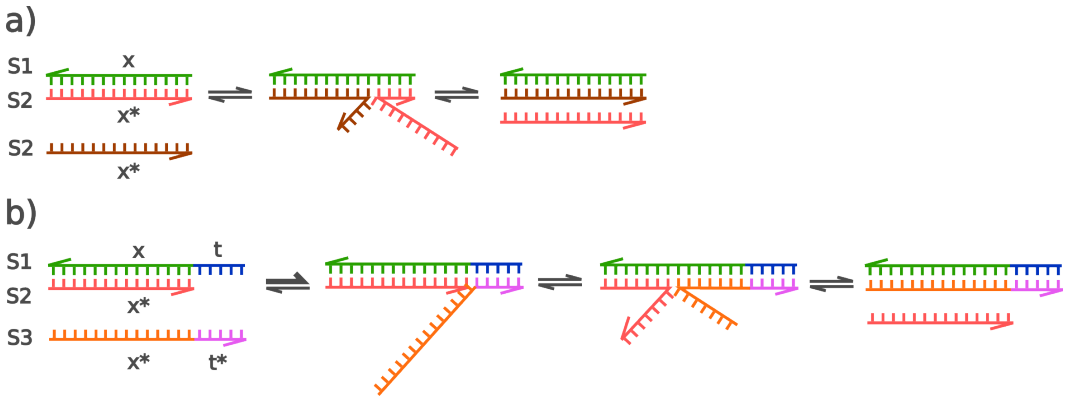

Figure 1.2: a) Strand displacement reaction. Notice that S2 is shown in two different colors to highlight the two copies, but they are effectively identical molecules. The duplex S1-S2 is not formed irreversibly and thermal fluctuations stochastically start unzipping it at either end. If a second copy of S2 is present, it might bind to where S1 has opened up, and over time possibly displace the original S2. Importantly, the process can move in either direction, and there is no energetic bias towards the initial or final state. b) Toehold-mediated strand displacement. The different thickness of the arrow in the first step of the reaction highlights that the reaction is biased forward, as the free energy of the system is lower when more basepairs are formed. Thus the addition of the toehold biases the reaction forward. Figure inspired by Simmel, Yurke, and Singh, 2019

DNA Strand Displacement

The hybridization of two DNA strands into a single double-stranded DNA molecule should not be thought of as an irreversible process: even after the duplex has been formed, nucleotides will unbind and bind again, and the process will follow a random walk such that any single nucleotide unbinding could be followed by more and more unbinding events, up to the point where the two strands might be released. The random walk could proceed either way, promoting hybridization or dehybridization, but it is biased towards the lower free energy state, that is to say the fully double-stranded complex. Let us imagine a single complex formed by strand S1 with one domain x, and by strand S2, the perfect reverse complement for S1 with domain x*, as shown in Figure 1.2a. This complex might start unzipping and another copy of the molecule S2 might start hybridizing to the nucleotides of S1 that are now free. Through the random walk the new copy of S2 might end up replacing the old one in the complex S1-S2. This is an example of DNA strand displacement, where one of the two strands has been displaced and replaced by a new one. The reaction we have described is not biased in any direction, given that the free-energy of the initial complexes is the same as the free-energy of the final complexes (they are virtually

identical, just different copies of the same molecule).

It is more interesting to look at a slightly more complex example, such as the one in Figure 1.2b where strand S1, with domains *t* and *x* is bound to strand S2, with a single domain *x**. Thus the domain *t* will remain single-stranded in the complex S1-S2. Now we can add a third strand S3, with domains *x** and *t**, which is the reverse complement of S1—notice that the domains are listed in the reverse order, as they are conventionally written in the 5'-3' orientation. The domain *t**, which we will call toehold, can bind to *t* and, following again a reversible process, S3 can completely replace S2, forming complex S1-S3. The difference from the previous example is that S1-S3 has a higher number of paired nucleotides than S1-S2, leading to a state with lower free-energy. This means that the strand displacement is biased forward, i.e. after introducing S3 we expect to see S2 be completely replaced by S3, not a mixed population of S1-S2 and S2-S3. While branch migration has been seen in biology starting from the 1970s (Lee, Davis, and Davidson, 1970; Radding et al., 1977), the addition of toeholds in what is called toehold-mediated strand displacement has had a transformational impact on DNA nanotechnology becoming the foundation to design DNA machines (Yurke et al., 2000), DNA logic (Qian, Soloveichik, and Winfree, 2011), structures capable of conformational changes (Andersen et al., 2009), and countless more systems.

The reaction we have described, involving three DNA strands, is called three-way branch migration; it should be noted that there is another important mechanism of toehold-mediated strand displacement that happens between two double-stranded complexes, usually with two toeholds. It is called four-way branch migration and it is considerably slower than three-way branch migration. A good example of the reaction with intermediate steps can be found in Simmel, Yurke, and Singh, 2019, but we will not describe it in detail here. However, one notable property of this reaction is that the four strands form a Holliday junction, the pillar of structural DNA nanotechnology.

1.2 DNA Nanotubes

In the methodically designed world of DNA nanotechnology, DNA nanotubes seem to be the exception, and likely first appeared as an undesired competing product in 2D array design[1]. This is not just a coincidence, but it stems from the fact that, when we try to constrain DNA helices through junctions, we are straining them, and that

[1]Two such examples are found as personal communications, cited as references 14 and 15, in Rothemund et al., 2004

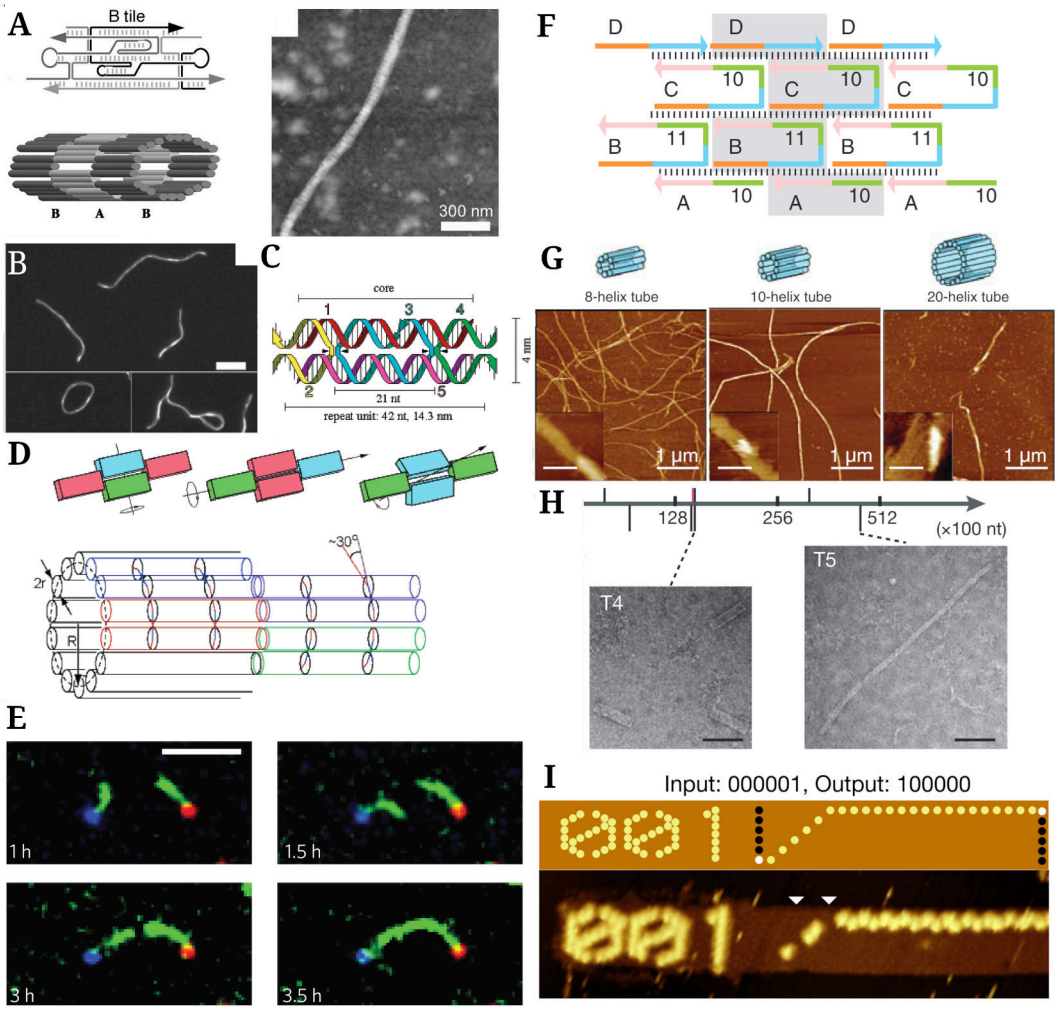

Figure 1.3: DNA Nanotubes (A) Triple-crossover tile nanotubes from Liu, Park, et al., 2004. (B) Double-crossover tile nanotubes imaged under light microscopy. Scale bar 5 µm. (C) Design of a single double-crossover tile. (D) Twist in the double-crossover tiles causes the structure to fold as a DAE nanotube. B-C-D Reprinted with permission from Rothemund et al., 2004. Copyright 2004 American Chemical Society. (E) DAE nanotubes seeded from molecular landmarks and grown to connect them in Mohammed, Šulc, et al., 2017. Scale bar 5 µm. Reproduced with permission from Springer Nature. (F) Design of a single-stranded tile (SST). (G) AFM images of SST nanotubes programmed with different circumferences. Inset scale bars 50 nm. F-G From Yin et al., 2008. Reprinted with permission from AAAS. (H) SST nanotubes with up to 1000 individually specified tiles. Scale bars 100 nm. Reproduced with permission from Springer Nature from Wei, Dai, and Yin, 2012. (I) Algorithmic assembly of SST tiles that compute a sorting function from Woods et al., 2019. Reproduced with permission from Springer Nature.

stress is often released through a larger scale twist of the structure, which in this case leads to curvature and tube formation. The first published DNA nanotubes (Liu, Park, et al., 2004; Yan et al., 2003) were designed using tiles with triple crossover motifs (LaBean et al., 2000), which provide higher flexibility compared to previously demonstrated double crossover motifs (Fu and Seeman, 1993). Shortly thereafter, double crossover tiles forming DAE nanotubes were described in Rothemund et al., 2004. We will first focus on this design, as we will use it extensively throughout Chapter 4.

DAE Nanotubes

The name of the DAE tile comes from **d**ouble crossover **a**nti-parallel **e**ven half-turns, meaning that each tile contains two crossovers, that the two strands at the top and bottom of the tile are anti-parallel (looking at the tile, one runs 3'-5', the other one 5'-3'), and that it spans an even number of half-turns of the DNA helix, i.e. its length in basepairs is a multiple of 10.5, equivalent to one helical turn. Figure 1.3C shows the scheme of a DAE tile, highlighting its properties, and specifically the presence at its four corners of short single-stranded sequences, called sticky ends, that bind to other tiles, forming superstructures of multiple tiles that can grow endlessly, as shown in Figure 1.3B-D. From the cartoon model and initial understanding of the system, these tiles seem planar and could be expected to form boundless 2D crystals. However, the formation of tubes suggests that the DAE tile has intrinsic stress due to the location of its junctions. This stress is relieved in solution through curvature, and this curvature adds up over a few tiles, making them wrap around and close on each other as a tube, rather than extend throughout the plane. Designing sticky ends and tile-tile interactions leads to different types of nanotubes, as shown in Figure 1.3B. While these designs are structurally identical under a microscope, the ability to use different DNA sequences in different tiles leads to higher modularity and programmability for the applications of interest in this work. DAE nanotubes can be seeded with a DNA origami to control their growth through the presence of a template seed (Mohammed and Schulman, 2013), and they can be programmed to connect different locations (Mohammed, Šulc, et al., 2017 in Figure 1.3E). It has been shown that some degree of strand displacement is possible within isolated DAE tiles (Zhang, Hariadi, et al., 2013), but strand displacement within a DAE DNA nanotube has never been demonstrated, and it is considered to be likely hard, given steric constraints and the presence of two double crossovers. We will discuss this in further detail in Section 4.4.

SST Nanotubes

A different design of DNA nanotubes was demonstrated in Yin et al., 2008, using a simpler and more flexible single-stranded tile (SST). Here the tiles are composed of a single DNA strand that is folded on itself, forming a half-crossover as shown in Figure 1.3F. Thanks to the simplicity of this design, each helix can use a different tile and it is possible to program the number of helices in a nanotube, thus changing its circumference from small 4-helices tubes to large and stiff 20-helices tubes, as in Figure 1.3G. Due to the lack of strong double crossovers, SST tiles are more flexible than DAE tiles and can be easily used to design planar and complex systems (Wei, Dai, and Yin, 2012), including structures where all the tiles are individually specified, up to a thousand tiles, forming both nanotubes (Figure 1.3H) and 2D designs. Combining structural and dynamic DNA nanotechnology, algorithmic self-assembly of SST tiles has led to ribbons that are capable of computing logic functions (Woods et al., 2019 in Figure 1.3I).

1.3 DNA Origami

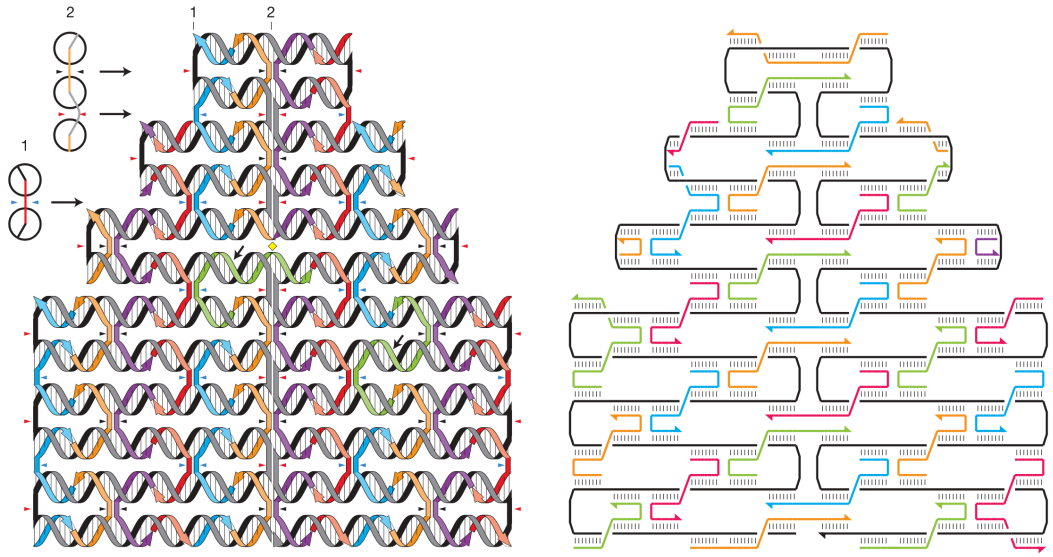

Figure 1.4: Model of a simple DNA origami design. The scaffold strand, shown in black on both sides, is folded and held in place by staple strands (various colors) that are designed to bind to different locations on the scaffold, stapling them together. While the right side shows the conceptual design we describe, the left side gives a more realistic model, where the DNA helices need to be oriented correctly so that crossover junctions can be formed without the staple strands being too strained.

A leap forward in DNA nanotechnology happened with the introduction of DNA origami in Rothemund, 2006 that pushed the field from simple and crystal-like

structures to extremely complex and programmable designs of 10^3 individually addressable basepairs, using hundreds of DNA strands. While DNA origami exploits the same concepts of Holliday junctions and double crossovers as the structures we have mentioned before, it is conceptually useful to look at it under a different paradigm. The first necessary component of a DNA origami is a long single strand of DNA, called the scaffold, which is usually the genome of a viral bacteriophage, approximately 7k bp long. We can imagine the design of a single oligonucleotide, with two short (~20 bp) domains, one complementary to a given region A1 of the scaffold, the other one complementary to a different region B1 of the scaffold, where these two locations do not need to be adjacent or near each other. We will call this oligonucleotide "staple" as it will bind to both regions and bring them together, stapling them to each other. The junction can be seen as half of a Holliday junction, or a half-crossover. We can then design a second staple that binds to regions A2 and B2, which are found immediately next to A1 and B1, bringing them together, and forming the other half of the crossover, or a complete junction. The process is then repeated throughout the scaffold to staple all the desired locations together and confer shape and rigidity to the structure, resulting in a design comparable to the one shown in Figure 1.4. A more realistic model also needs to consider the orientation of the helices, as the staple strands can only bridge them in locations where a crossover is possible. Computer software has been written to significantly automate the design of DNA origami (Douglas, Marblestone, et al., 2009, Doty, Lee, and Stérin, 2020, Levy and Schabanel, 2021), almost to the point where entire sets of staple strands can be automatically generated from an ideal shape or structure. The literature on DNA origami has exploded in the last 20 years, it has been generalized from 2D to 3D structures (Douglas, Marblestone, et al., 2009), it has been used to build multilayer shapes (Thubagere et al., 2017), and it has been skeletonized to wireframe DNA origami (Zhang, Jiang, et al., 2015). Multiple DNA origami have been used to build larger structures using them as stacking blocks (Ke et al., 2012), as crisscrossing slats (Wintersinger et al., 2023), and as interlocking units (Wagenbauer, Sigl, and Dietz, 2017).

The technique has found research applications in nanofabrication (Gopinath et al., 2021; Maune et al., 2010), modeling of biological systems (Shen, Feng, et al., 2023), crystallography (Liu, Matthies, et al., 2024), especially for protein modeling (Aissaoui et al., 2024; Khoshouei et al., 2024), therapeutics (Oktay et al., 2023; Zeng et al., 2024), and more.

1.4 Motor-Filament Systems in Biology

The idea of self-organizing active matter is of particular interest in biology to explain how complex behaviors can arise from the convergence and cooperative behavior of ensembles of relatively simple active molecules. In response to external stimuli, these units can perform mechanical work and organize around the cell, sustaining complex processes such as cell division.

In the cell, the most studied active matter system is the one of protein motors and microtubules, an example of a motor-filament system. During cellular division, the cell is stretched by the spindle formed by microtubules and two copies of the genome are brought to the extremities, so that the genetic material inside the mother cell gets spatially separated and two new cells can be formed. This behavior happens through the interaction of not just filaments and motors, but many other signaling molecules. Many of the components of this system have been studied thoroughly and they individually should not be thought of as an active matter system, which only results from their collective behavior.

I will briefly describe the molecules of interest for our work, focusing on the ones involved in molecular transport. Microtubules play different and important functions in the eucaryotic cell, being largely responsible for its structural properties. Aside from their dynamic role in cell division, they are an important component of the cytoskeleton and flagella. They are long and stiff tubes formed by a protein called tubulin which is found in microtubules as a dimer with α and β subunits. A few copies coalesce together forming a nucleus and more and more are added, creating a tube-like structure that can grow rapidly and exert forces on the cell membrane, stretching it. As quickly as these units come together, they can disassemble, with tubulin dimers falling off based on the concentration of free tubulin in solution and on the action of other proteins. Importantly, due to the differences between α and β subunits, tubulin dimers are not symmetric molecules and microtubules exhibit a polarity from a plus end to a minus end. As a dimensional reference, microtubules have an external diameter of 25 nm, formed by 13 actin dimers, and they can grow up to 50 µm, with a very high persistence length, measured between 1.4 and 8 mm (Jia et al., 2004; van Mameren et al., 2009).

Two main families of motor proteins bind to microtubules: dyneins, which walk in retrograde direction, from the plus to the minus end, and kinesins, which mostly walk in the opposite anterograde direction and have historically been characterized more extensively. Motor proteins can often be loaded with a cargo and they are

thus responsible for most of the active transport within the cell, for example by carrying the chromosomes to the ends of the mitotic spindle during mitosis. Our work will focus on dynein, which are larger molecules compared to kinesins, and are composed of several subunits. We will consider the human version of dynein, which exhibits a mean step size of ~8 nm (Kinoshita et al., 2018) and an average speed of ~1.2 μm/s (Verma, Wadsworth, and Maresca, 2024). The head of the protein is a large spherical (or donut-shaped) subunit where the activity of dynein happens, with ATP being hydrolyzed and converted into the mechanical motion of the kick. Two subunits intertwined in a helical chain form the stalk or leg of the motor, which acts as a lever amplifying the kick. At the end of this chain, the foot of the motor can bind to the tubulin, in order to perform its walk. The foot of the motor protein binds to the tubulin on the microtubule and the head kicks it forward, then the foot gets detached and falls off before taking the next step. In the cell, dynein is found as a dimer, with two heads and two legs, so that the motor stays anchored to the microtubule with one leg after each kick and does not simply fall off. This type of motion is called processive. In our work, we will use a monomer dynein that falls off the microtubule with every step it takes, as it is commonly done in a set of experiments called gliding assays. In these non-precessive conditions, the stalling force of human dynein has been measured to be ~2 pN (Brenner et al., 2020).

1.5 Engineering Motor-Filament Systems

As mentioned above, we will focus on a specific experimental setup, which is generally called a gliding assay. Here motor proteins are attached to a glass slide and filaments move or "glide" on top of them. This is intuitively the opposite of what happens in the cell, where the motors are the moving units, carrying cargo along the mostly still filament, but it results in a fairly simple setup where mesoscale motion of fluorescent microtubules can be studied. Motor proteins can be labeled with a tag that binds them to a functionalized glass surface, for example through a biotin-streptavidin conjugation, and their leg and foot side, which binds to the tubulin and performs the kick, will be sticking outwards. If the density of motors is sufficiently high, several of them will be moving the filament at any given time, but the average velocity recorded is equal to that of a single motor protein, given that their interaction is not cooperative (Hancock and Howard, 1998). As the glider is propelled forward by the kick of the motors, its head will look for and bind to a new motor, and Duke, Holy, and Leibler, 1995 developed a theory to explain how this happens. If the surface density of motors is sufficiently high, this search is posited

to be dominated by the capture radius of the motor, 80-90 nm for kinesin. If the density is lower, or if the filaments are especially floppy, the head of the tube will have time to move around diffusively and explore the area that surrounds it before binding to a new motor protein. Most gliding assays with microtubules and kinesin seem to be performed in the first regime, as the gliders appear to move straight, with almost no diffusive component. This is due both to the density of motors and to the millimetric persistence length of the microtubules.

Due to the difficulty in mutating and engineering tubulin, there have been relatively few attempts to expand gliding systems beyond studies of external conditions. They have mostly focused on creating bundles of microtubules and looking at their gliding properties. Kawamura et al., 2011 achieved it by labeling microtubules with biotin, which Liu, Spoerke, et al., 2008 then used to create novel gliding behaviors of rings of microtubules. One example that incorporates DNA nanotechnology is shown in Keya et al., 2018 where two populations of microtubules are labeled with azides to attach a DNA strand with an azobenzene modification. Azobenzene acts as a light switch for the hybridization of the two DNA strands conjugated to the two populations, creating swarms of microtubules held together by DNA. The use of a light switch allows for a first level of external control over the behavior of the system, switching between a swarm state and a traditional gliding state.

The development of motor proteins for DNA tracks (Ibusuki et al., 2022) and the desire to expand on this system to demonstrate new behaviors and more complex DNA nanomachines led us to incorporate new control machinery in DNA nanotubes in Chapter 4 and then to explore the interactions between motor proteins and DNA origami in Chapter 5.

Chapter 2

MODULAR DNA ORIGAMI-BASED ELECTROCHEMICAL DETECTION OF DNA AND PROTEINS

2.1 Introduction

DNA nanotechnology (Jones, Seeman, and Mirkin, 2015; Seeman and Sleiman, 2017) enables the design and construction of artificial structures with nanometer precision via sequence-specific assembly of DNA oligonucleotides. Such structures (*e.g.* branched DNAs and tetrahedra, (Idili et al., 2022; Li, Hu, et al., 2017; Pei et al., 2011; Xuan et al., 2023)) are often used as scaffolds for biosensors, wherein DNA-coupled binding components, such as aptamers, antibodies, or small-molecule ligands produce a signal upon introduction of a cognate analyte molecule. DNA origami (Douglas, Dietz, et al., 2009; Rothemund, 2006), provides an architecture for making 100-nanometer scale structures of arbitrary geometry, with hundreds of attachment sites for active components such as binders or reporters. Thus DNA origami is of particular interest for biosensors (Pitikultham et al., 2022; Shen, Wang, and Ke, 2021; Wang et al., 2020) because it allows the synthesis of reconfigurable structures that undergo large conformational changes (tens or hundreds of nanometers, (Andersen et al., 2009; Chandrasekaran et al., 2021; Endo et al., 2015; Funck et al., 2018; Hansen et al., 2017; Huang et al., 2018; Hudoba et al., 2017; Koirala et al., 2014; Kuzuya, Sakai, et al., 2011; Kuzuya, Watanabe, et al., 2014; Kuzyk et al., 2014; Schickinger, Zacharias, and Dietz, 2018; Selnihhin et al., 2018a; Shrestha et al., 2021; Tang et al., 2018; Zhou et al., 2018)), rearranging large numbers of reporters (tens or hundreds) (Selnihhin et al., 2018a) that amplify molecular binding events to the point that they can be reliably detected.

Reconfigurable origami sensor platforms can be divided into broad classes based on their readout mechanism, with each mechanism having advantages and disadvantages. Atomic force microscope (AFM)-based platforms, for example, such as "DNA forceps" (Kuzuya, Sakai, et al., 2011; Kuzuya, Watanabe, et al., 2014) or "picture frames" (Endo et al., 2015) enable the direct visualization of single molecule reconfiguration as a function of protein binding (Kuzuya, Sakai, et al., 2011), pH (Kuzuya, Watanabe, et al., 2014), or ionic conditions (Endo et al., 2015) but they require expensive AFMs and time-consuming measurements. Single-molecule flu-

orescence, optical tweezers, and magnetic tweezers-based platforms (Hudoba et al., 2017; Koirala et al., 2014; Schickinger, Zacharias, and Dietz, 2018; Shrestha et al., 2021) exhibit extraordinary temporal resolution for the reconfigurations of single molecules, and enable the dissection of sensor states that could otherwise not be resolved. But, as for AFM, the required equipment is expensive and the measurements time-consuming. Gel electrophoresis-based platforms (Hansen et al., 2017) for protein or nucleic acid detection are relatively inexpensive, and can be multiplexed (Chandrasekaran et al., 2021). However, these measurements are slow, at best taking tens of minutes. Fluorescence resonance energy transfer (FRET) platforms have provided simple bulk measurements of DNA (Andersen et al., 2009) and protein (Tang et al., 2018) down to the 100 nM range; achieving 100 pM has required expensive single-molecule FRET microscopy (Selnihhin et al., 2018b). Chiral plasmonic platforms have enabled simple bulk sensing of nucleic acids (Funck et al., 2018; Kuzyk et al., 2014) and small molecules (Huang et al., 2018; Zhou et al., 2018) achieving 100 pM sensitivity for RNA, but spectrometers capable of measuring circular dichroism are relatively expensive. Layered on top of these concerns, few of these approaches have been shown to work in complex biological sample matrices, and none of the above platforms appear easily extendable to *in vivo* measurements.

In contrast to these techniques, an electrochemical platform based on the conformation-switching of single-stranded DNAs (Arroyo-Currás, Dauphin-Ducharme, et al., 2020) enables real-time measurements of analytes using inexpensive potentiostats (Scott et al., 2022). By using miniaturized electrode implants, analytes can be quantified in challenging environments such as living animals (Arroyo-Currás, Somerson, et al., 2017; Gerson et al., 2023). This platform uses a gold electrode, protected with an alkanethiol monolayer—the electrode is further functionalized with a target-binding oligonucleotide that displays a gold-binding thiol on one end of the oligonucleotide, and a redox-reporter (most commonly methylene blue, "MB") distal to the thiol. Upon interacting with its target, for example during DNA hybridization ("E-DNA sensors" (Fan, Plaxco, and Heeger, 2003; Xiao, Lubin, Baker, et al., 2006; Zwang, Tse, and Barton, 2018)) or aptamer-molecule binding ("E-AB sensors" (Hu et al., 2012; Pellitero, Shaver, and Arroyo-Currás, 2019; Xiao, Lubin, Heeger, et al., 2005)), the oligonucleotide undergoes changes that affect the rate of electron transfer between the reporter and the electrode surface. When the electrode is brought to the reduction/oxidation potential of the reporter, current is thus measured as a function of binding state of the oligonucleotide.

In the most common model of E-AB sensor operation, analyte binding-induced reconfiguration of the aptamer structure changes the collision frequency of the redox reporter with the electrode surface, changing the electron transfer rate and thus measured current (White, Rowe, and Plaxco, 2010). Analyte binding in E-AB sensors is transduced into a signal by a unique and idiosyncratic binding-induced nanometer-scale movement; this conformational change *differs between different aptamers* (*e.g.* see differences between thrombin and IgE aptamers in White, Rowe, and Plaxco, 2010) and it is evident that binding and signal transduction depend on each other in complex ways. Thus, making sensors for new analytes with both good signal gain (relative change in signal upon target saturation) and appropriate affinity and selectivity often requires optimization, with multiple rounds of semiempirical redesign and resynthesis of expensive modified oligonucleotides (White, Rowe, and Plaxco, 2010). Spectroscopy-guided approaches to aptamer probe redesign (Wu, Ranallo, et al., 2023) shorten, but do not eliminate this onerous process. Special "capture SELEX" techniques that select for conformational change of the aptamer (Stoltenburg, Nikolaus, and Strehlitz, 2012; Yang, Pei, and Stojanovic, 2016) rather than simple binding, can increase the likelihood of obtaining suitable switching aptamers but cannot guarantee success.

The question arises: might the advantages of reconfigurable DNA origami and E-DNA/E-AB systems be combined? Several recent publications explore DNA origami in the context of electrochemical sensing. For example, the capacity of origami to display multiple binders has been used for an electrode-bound miRNA sensor, wherein origami acts as a substrate that presents multiple miRNA binding sites (Han et al., 2019). Likewise, a pH sensor has been reported that employs a reconfigurable DNA origami "zipper" bound to a gold electrode (Williamson, Ijäs, et al., 2021), and electrode-bound origami were used to probe the spatial dependence of redox-active enzyme activity (Ge et al., 2019). Free DNA origami rectangles have been used to amplify signal from DNA analytes (Williamson, Piskunen, et al., 2023); the detection of free origami rectangles themselves represent an elegant demonstration of nanoimpact electrochemistry (Pensa et al., 2022). Unlike E-AB/E-DNA systems, however, these origami-based systems are not reagentless; they all require the addition of redox mediators to the analyte solution to generate electrochemical signals, which limits their use *in vivo* or in other environments where these mediators are not available. And aside from the pH-responsive zipper (Williamson, Ijäs, et al., 2021), none of the above systems use large-scale conformational reconfigurations for signal transduction.

One reconfigurable origami-based electrochemical sensor that uses MB reporters instead of added redox mediators has been reported (Arroyo-Currás, Sadeia, et al., 2020). Intended to detect 100 nm scale analytes such as viruses, this system requires significant modification for analytes of different sizes. Furthermore, as configured, it is a "signal-off" device, for which analyte binding results in a lower current; this limits both the signal gain (at best, -100%; see formula for gain below) and confidence that signal change is not caused by sensor degradation.

In this work, we introduce a reconfigurable DNA origami sensor whose modular architecture overcomes the redesign and optimization challenges posed by E-DNA and E-AB sensors. By combining a flat, two-dimensional DNA origami with a double-stranded DNA (dsDNA) linker, we create a "lily pad" structure wherein origami, decorated with numerous MB redox reporters are tethered to an ultra-flat gold electrode via a long and flexible dsDNA linker (Figure 2.1). This open conformation is converted to a closed conformation by the presence of analyte biomolecules when they bind and form a bridge between a pair of probes on the origami and on the electrode surface. The resulting conformational change is detected via square-wave voltammetry (SWV, Figure 2.1B, inset), in which the current, which is a function of the rate of electron transfer between MB molecules and the electrode surface, increases with proximity.

The lily pad architecture described above is reminiscent of a classical sandwich assay, in which a pair of affinity binders is used to localize a signaling system to a surface if and only if the target analyte attaches to both binders: the first binder, or "capture" reagent, is attached to a surface; addition of sample results in target analytes being bound to capture reagents via a first epitope; further addition of a labeled "detect" reagent that binds the analyte at a second orthogonal epitope provides a mechanism to generate signal. Simple binders, rather than the structure-switching binders of E-AB systems, are all that is required; industry has generated many thousands of capture-detect antibody pairs for commercial assays. Indeed, antibody pairs have been incorporated into a number of electrochemical assays—yet these systems are not reagentless, typically requiring both (1) a step involving physical addition of the detect reagent and (2) incorporation of an amplification system (typically attached to the detect reagent) such as an enzyme (Neupane and Stine, 2021), or hybridization chain reaction (Sun et al., 2018).

Given their success elsewhere in biosensing, it is interesting to ask why pairs of sandwich antibodies have not proven amenable to reagentless electrochemical

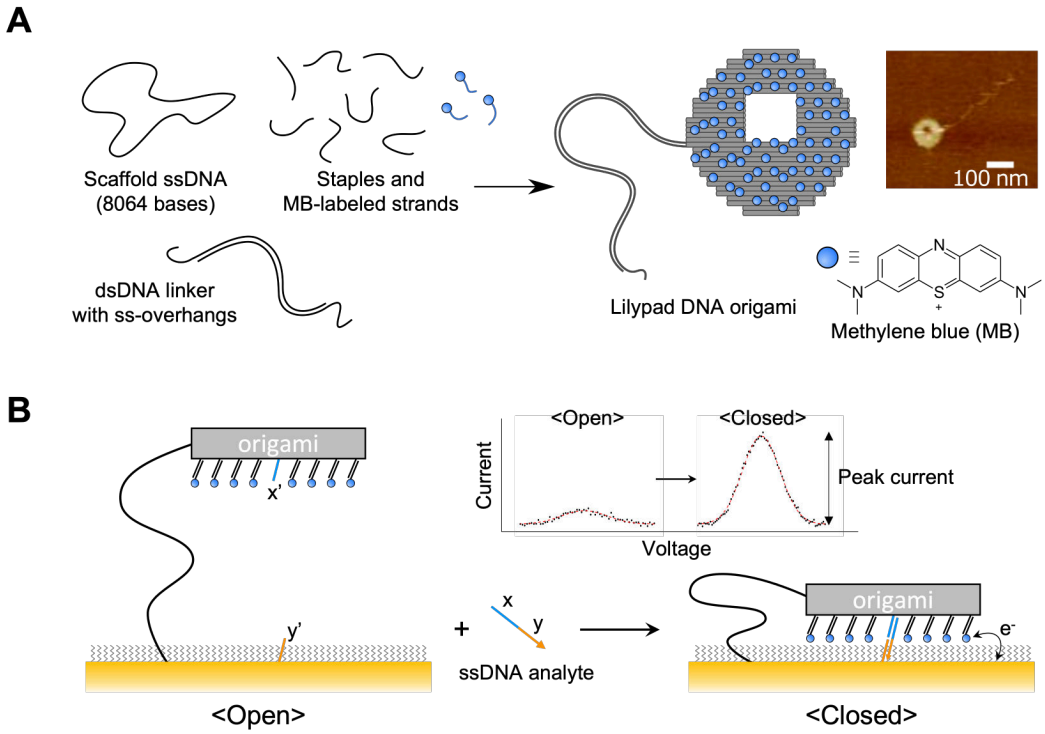

Figure 2.1: **Lily pad sensors can be used for the electrochemical detection of biological analytes, here a DNA single strand.** (A) A flat, disk-shaped DNA origami with a square hole (Gopinath et al., 2021) carrying a long dsDNA linker is assembled from a mixture of long ssDNA scaffolds, ssDNA staples, 70 staples with 5′-extensions for MB reporters and for analyte binding, 20 nt MB-modified DNA oligos, and long dsDNA linkers with ssDNA overhangs at both ends. Inset shows AFM of a lily pad. (B) Two types of thiol-modified ssDNA are immobilized on a template-stripped gold surface: one for tethering the lily pad origami via hybridization with one of the linker overhang sequences, and the other for analyte binding to the gold surface. Closing events occur when a DNA analyte binds both to the binding site on the origami and the binding site on the surface, enabling electron transfer between MB reporters and the gold electrode. Inset shows an exemplary square wave voltammogram of a sensor in the open state (left), and a voltammogram in the closed state after DNA analyte addition (right). The peak current is calculated as the heights of the peaks relative to the underlying baseline.

sensing. Reagentless sensors require (1) that all of their components, from the binders to any detection system to be built into a single, intramolecular device, which reconfigures upon analyte binding and (2) that the reconfiguration be able to work with the detection system to create a signal of sufficient magnitude. The first requirement might in principle be solved by a simple linker between the binders, but the second requirement turns out to be a more fundamental problem. In typical sandwich immunoassays, the stack formed by the capture reagent, analyte, and detect reagent is at least several nanometers in height, *e.g.* 10 nm in the case of bovine serum albumin with two antibodies (Murphy et al., 1988). To render the device reagentless, some component has to be directly labeled with a redox reporter; labeling either antibody would result in a geometry for which electron transfer to the surface is too slow for sensitive detection (for E-AB sensors, electron transfer rates drop off significantly a few nm from the electrode surface) (Dauphin-Ducharme, Arroyo-Currás, Adhikari, et al., 2018). This length scale problem has limited development of reagentless electrochemical sandwich immunoassays. A cleverly-designed system (Dauphin-Ducharme, Arroyo-Currás, Adhikari, et al., 2018) utilizes a combination of DNA linkers with an antibody pair, in a geometry that positions a MB reporter at the very base of the sensor in the analyte-bound state. This results in an antibody sandwich acting as a highly sensitive, amplification-free, electrochemical sensor whose performance does not depend strongly on the size of the binders or analyte. However, that sensor still requires addition of DNA-labeled antibodies in solution and thus does not operate in a reagentless mode.

Here, our lily pad design overcomes the problem of large binder-analyte sandwiches through its use of numerous MB reporters which project down from the origami in a flexible "curtain" around the sandwich that extends at least 5 nm towards the surface. Like E-DNA/E-AB systems, our lily pad incorporates all components in a single, intramolecular construct rendering it reagentless. Unlike the E-DNA/E-AB systems the lily pad is more easily adapted to other analytes—by simply exchanging unmodified strands for linkers and curtain length we demonstrate the detection of DNA and two different proteins.

2.2 Lily pad DNA origami device

E-DNA/E-AB sensors often use roughened gold electrodes to maximize the surface area for their small ssDNA sensing molecules (Arroyo-Currás, Scida, et al., 2017; Mahshid, Mepham, et al., 2016), despite the resultant structural heterogeneity of such electrodes. Here, in contrast, we use ultraflat, template-stripped gold chips

(Hegner, Wagner, and Semenza, 1993) to minimize the distance between the entire bottom face of the origami disk and the electrode surface upon analyte binding. Our lily pad sensors use 70 MB molecules as reporters to transfer electrons to the electrode; they are attached to one side of each origami via 20 bp-long ssDNAs hybridized to overhangs on 70 modified staple strands (Figure 2.1B)—this forms a curtain of MB-modified DNA strands hanging from the origami. Detection of a ssDNA analyte sequence xy is achieved through binding to two DNA sequences, x' and y', which are complementary to subsequences x and y of xy, respectively. Sequence x' is positioned on the origami as an extension to a central staple, and a thiol-modified version of y' is immobilized on the gold electrode surface via an Au-S bond. When both x and y in a DNA analyte bind to x' and y' on the lily pad and the underlying electrode, the conformation of the lily pad changes from the "open" to the "closed" state. Each closing event brings the 70 MB curtain into proximity with the gold surface, facilitating electron transfer between MB and electrode and increasing voltammetric peak currents (Figure 2.1B, inset).

The distance between MB molecules and the electrodes, which determines the electron transfer rate, is set by the particular probe-analyte binding geometry (Dauphin-Ducharme, Arroyo-Currás, and Plaxco, 2019). We note that in the open, unbound state, the relative average position of the MB redox reporters with respect to the surface is a function of the flexibilities of the dsDNA linker, origami (Lee, Lee, et al., 2021; Ni et al., 2022) and MB attachment; therefore we would expect background signal even in the absence of analyte (see below). Background signal is observed with E-DNA and E-AB sensors for similar reasons (Pandey et al., 2021; Xiao, Lubin, Baker, et al., 2006), and it is observed here (Figure 2.1B, left side of inset).

For the closed, bound state, the same factors should affect electron transfer rate, with the exception that the distance between the lily-pad's reporters and the surface should be independent of the dsDNA linker length. We estimate the reporter-surface distance for the closed state by noting that the length of the bound DNA analyte is 28 bp (~9.8 nm); as the tail length is 20 bp (~6.8 nm) for the reporter strands, this difference leaves the redox reporters nominally ~3.0 nm away from the surface on average (Figure 2.3A, blue inset). Were the MB rigidly held at this position, thirty times the electron-transfer decay distance (Dauphin-Ducharme, Arroyo-Currás, Kurnik, et al., 2017), electron transfer rates would be unmeasurably slow; thus we suspect that bending fluctuations of the origami cause MB to visit

distances less than 3 nm from the surface, enabling electron transfer from the MB curtain to be observed.

In principle, more MB units per lily pad should generate a greater signal upon analyte binding. However, saturation MB modification (1 MB per staple) leads to aggregation of origami during annealing, potentially due to the DNA intercalation of MB, electrostatic DNA backbone-MB interactions, or concentration-dependent dimerization of MB (Bradley et al., 1972; Nordén and Tjerneld, 1982). Optimizing lily pad MB density while minimizing aggregation, we found that the use of 70 MB-modified extensions results in lily pads that run as monomers in agarose gels, while higher numbers of MB reporters lead to poorly formed structures that aggregate and remain stuck in gel wells (for optimization see Section 2.4).

2.3 Lily pad origami design

Lily pads were prepared by adding dsDNA linkers ("stalks") with two single-stranded overhangs to the folding reaction of 2D origami with 70 MB reporters. Using the concentration of the linker measured by Nanodrop spectrophotometer and the concentration of scaffold provided by the manufacturer, we performed a titration to find the optimal [linker] to [scaffold] ratio to prepare Lily pad origami with minimal amount of free, unbound dsDNA linkers left so that we can use the annealed origami samples without further purification. Lily pad origami mixtures were prepared as in Table 2.1 and annealed from 90 °C to 20 °C at -1 °C/min.

Contents	Concentrations
scaffold (p8064)	5 nM
Staple strands (70 5'-extended)	10 nM (each)
MB reporter strand	1.05 µM
1 kbp linker	(i) 10 nM (ii) 5 nM (iii) 2.5 nM
TAE	1×
$MgCl_2$	12.5 mM

Table 2.1: **Titration to optimize the amount of 1 kbp dsDNA linker for Lily pad synthesis.**

Addition of the linker results in appearance of a new, higher molecular weight band in gel as seen in the middle lane in Figure 2.2a, corresponding to full Lily pads. For comparison, 1 kbp linker and origami only without the linker were run next to the Lily pad lane, the lanes 2 and 4 respectively, where the amounts of the linker in

the lanes 2 and 3 are the same, and the amounts of the scaffold (or origami) in the lanes 3 and 4 are matched. We found that when [linker] : [scaffold] = 1, a good amount of Lily pad origami structures are formed and the remaining unbound linker is negligible, as seen in the gel image in Figure 2.2b (left) and in the right panel where the band intensities are plotted for along the DNA migration direction for each sample. For the rest of our Lily pad syntheses we used this 1:1 ratio of linker to scaffold and used the annealed Lily pad origami mixtures without purification, assuming that all the free origami without the linker and the excess staple and MB strands are washed away after lily pads are tethered on gold surface.

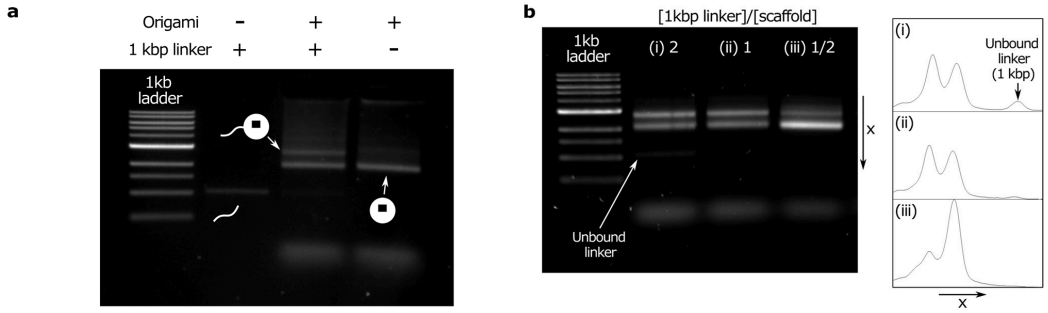

Figure 2.2: **Gel analyses of Lily pad synthesis.** (**a**) Gel image for 1 kbp linker, 1 kbp linker + 2D origami (full Lily pad), and origami only, from left to right. The amount of 1 kbp linker in the lane 2 and lane 3 are same. This gel serves as a reference for the 2D origami and full Lily pad in the gel below. (**b**) Gel image for Lily pad with 70 MB reporters when folded with different amount of 1 kbp linkers. 1%, SYBR-Safe pre-stained agarose gel was run at 75 V for 90 min at 4 °C in TAE with 12.5 mM $MgCl_2$. [linker] : [scaffold] is reported above each lane.

2.4 Optimizing the number of MB per origami

We first tried folding 2D origami with the maximum number of methylene blue (MB) reporters possible, i.e. by extending the 5′ end of all 234 staples with linkers complementary to an MB reporter strand. We observed that these heavily-functionalized origami aggregated, presumably due to MB multimerization (Braswell, 1968; Leaist, 1988) and/or electrostatic interactions between MB and the DNA backbone (Vardevanyan et al., 2013). To find the maximum usable number of MB per origami for electrochemical sensors, we prepared 2D origami with different numbers of 20 bp MB reporters (0, 70, 120, and 200) and ran them in an agarose gel. The concentrations of the scaffolds, staple DNA strands, and MB reporter strands are listed in Table 2.2. 0, 70, 120, and 200 5′-extended staple strands were used to create origami with the corresponding number of MB reporters; in each case the rest of the staples

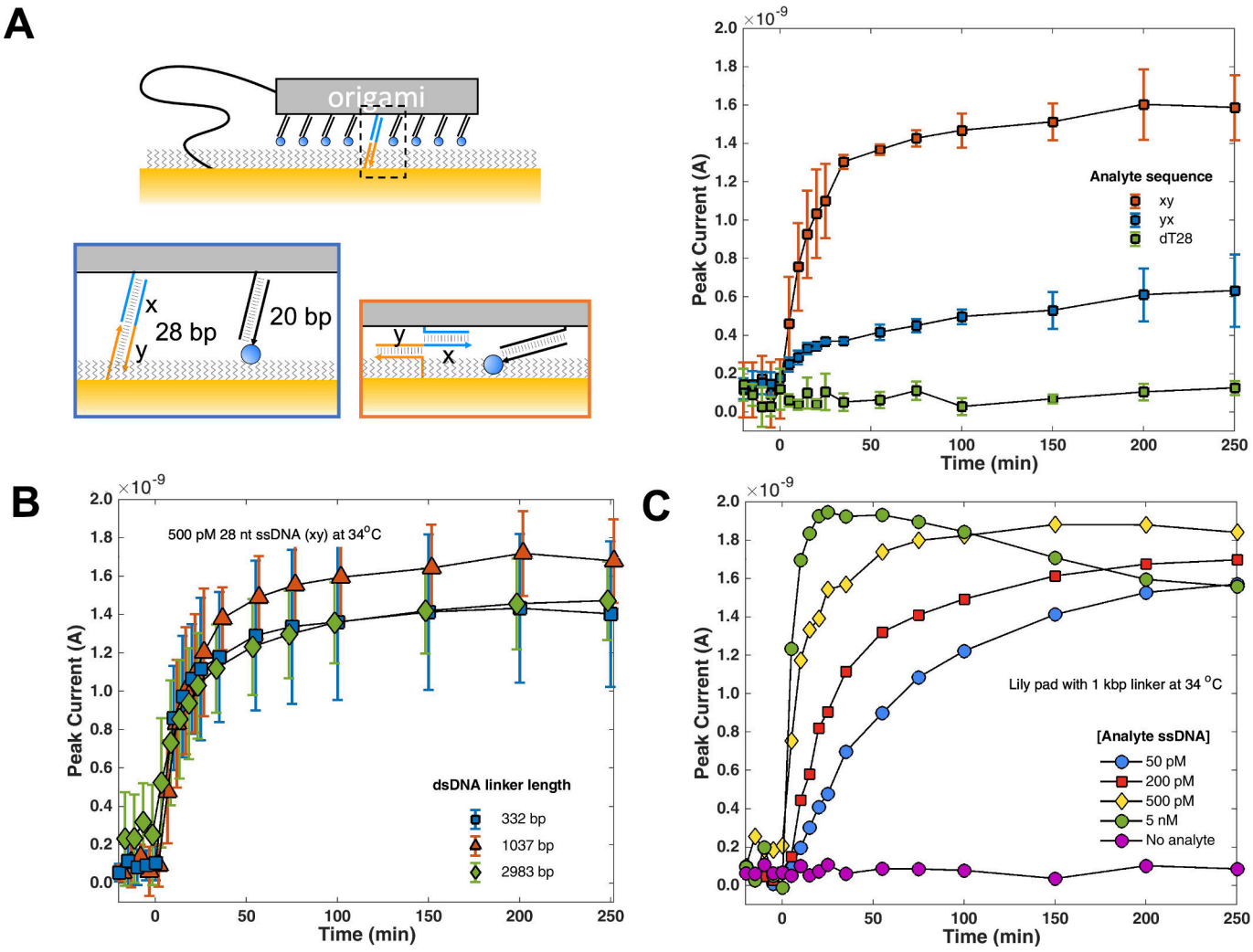

Figure 2.3: **Lily pad closing events can be monitored via voltammetry in real-time.** (C) The functional form of sensor response varies with the concentration of ssDNA analyte. At analyte concentrations up to 500 picomolar (yellow diamonds), sensor response increases monotonically. At nanomolar concentrations (green circles), the system shows saturation effects, and the current decreases after one hour, potentially due to excess free analyte in solution reopening previously-closed lily pads via DNA strand displacement. ssDNA analyte *xy* added at $t = 0$.

did not have single-stranded extensions. Staples were added in a 2× excess relative to the scaffold and the MB-strands were added at a 1.5× excess relative to the total concentration of extended staples. Four mixtures were prepared as in Table 2.2, heated to 90 °C for 5 min, and cooled to 20 °C at -1 °C/min.

A 1% agarose gel in TAE buffer with 12.5 mM $MgCl_2$ was cast with 1× SYBR-Safe staining dye. 5 µL of each of 5 nM origami was loaded after being mixed with 1 µL

Contents	Concentrations
scaffold (p8064)	5 nM
Staple strands	10 nM (each)
MB reporter strand	0, 1.05, 1.8, or 3 μM
TAE	1×
$MgCl_2$	12.5 mM

Table 2.2: **Concentrations of components used to fold origami with different numbers of MB reporters.**

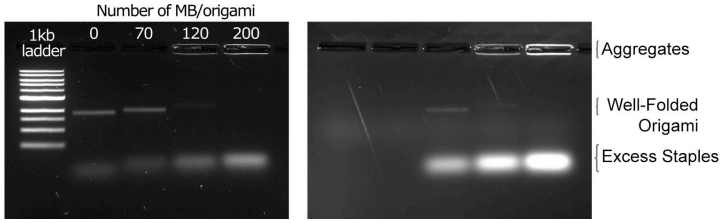

Figure 2.4: **Gel images for DNA origami with different number of 20 bp MB reporters.** From the left, 1 kb DNA ladder (New England BioLabs), disk origami with zero, 70, 120, and 200 MB reporters, evenly distributed. The gel was imaged with blue (left, for stained DNA) and on red (right, for MB fluorescence) LED illumination.

of 6× Gel Loading Dye (New England BioLabs). The gel then was run for 1.5 hours at 75 V at 4 °C in TAE with 12.5 mM $MgCl_2$ and visualized using a gel imaging system (Syngene G:Box) (Figure 2.4).

The origami with 0 and 70 MB reporters are seen as single sharp bands under blue LED illumination with 0-MB origami migrating faster than 70-MB origami; this indicates that both the 0-MB and 70-MB origami are properly folded, monomeric origami structures. On the other hand, both 120-MB and 200-MB functionalized DNA origami are observed as bright bands stuck in the well of the lanes 4 and 5; this suggests that larger numbers of MB reporters (120 and greater) cause origami aggregation. The led us to use 70-MB functionalized 2D origami to construct Lily pads for downstream electrochemical sensing experiments.

2.5 Chip preparation and electrochemical measurement

Ultraflat gold chips were fabricated via template-stripping (Hegner, Wagner, and Semenza, 1993; Weiss et al., 2007). This approach had the added benefit of revealing an extremely clean surface upon removal of the template. Two different thiol-modified ssDNA were immobilized on gold surfaces, one that binds the DNA origami linker and one that binds the analyte molecule. The surface was then

backfilled with a passivation layer of 6-mercapto-1-hexanol in order to minimize a current from oxygen reduction (Shaver, Curtis, and Arroyo-Currás, 2020). The chip was incubated with lily pad DNA origami structures and then used as the working electrode in a three-electrode cell.

2.6 DNA detection

observed for all the SWV presented in this work, and was observed to be stable for over 6 hours and up to 4 sensor regenerations (Figure 2.7). In general, the baseline provides a reference state from which the occurrence of binding events can be inferred.

Upon challenging the sensor with the fully complementary ssDNA analyte *xy*, an increase in SWV signal from baseline was observed (Figure 2.1B, inset), resulting in sensorgrams (Figure 2.3A, blue curve) similar to those resulting from other real-time surface-bound, DNA hybridization biosensors that use surface plasmon resonance (SPR), biolayer interferometry (BLI) and the E-DNA platform (Arroyo-Currás, Dauphin-Ducharme, et al., 2020; Arroyo-Currás, Sadeia, et al., 2020; Lubin and Plaxco, 2010; Xiao, Lubin, Baker, et al., 2006; Xiao, Piorek, et al., 2005; Zhang, Huang, et al., 2005). For reference, benchmark *optimized* E-DNA ssDNA-detecting sensors displayed gains of 260% (White and Plaxco, 2010); optimized E-AB sensors have reached 430% (Dauphin-Ducharme and Plaxco, 2016). Encouraged by these unprecedented gains, we proceeded to test the effects on sensor response of varying the lily pad and analyte structure.

For DNA analytes oriented perpendicularly to the surface, like *xy* (Figure 2.3A, blue inset), we expected that longer analytes (up to duplex DNA's persistence length) could decrease signal gain by preventing close approach of the 20 bp MB curtain. By switching the positions of the *x* and *y* to yield a sequence (*yx*), the orientation of the analyte was changed to be parallel to the surface (Figure 2.3A, orange inset), without significantly affecting predicted thermodynamics. We originally hypothesized that using this orientation could make signal gain independent of length. However, we observed (Figure 2.3A, right) slower on-signal kinetics (the rate of signal increase upon addition of analyte) and lower signal at the end of the experiment compared to the *xy* analyte, presumably due to the length of the MB curtain which appears to be a significant steric obstacle for the origami to successfully close. For practical reasons we did not pursue this approach further, but note that shorter MB curtains might recover signal gain and achieve the goal of DNA length-independent signal.

To explore the effect of the lily pad linker length on sensor performance, we synthesized and tested double-stranded DNA linkers of three different lengths: 332, 1037, and 2983 bp (Figure 2B). Given these results, we arbitrarily chose to use the 1037 bp linker for all subsequent experiments.

Figure 2C shows the sensor response to increasing concentrations of DNA analyte. For times less than an hour, both signal and signal kinetics (the rate of signal growth) increase monotonically with concentration. After an hour, two behaviors are observed: (1) signal for analyte concentrations less than 5 nM continues to increase, and (2) signal for an analyte concentration of 5 nM undergoes a surprising decrease. This bifurcation in behavior is reminiscent of the "high dose hook effect" (Wild, 2013) which occurs when excess analyte saturates both binders of a sandwich sensor, preventing sandwich formation and decreasing signal. Because the present hook effect emerges over the course of a time-based sensorgram, we term it the "kinetic hook effect".

Unlike the case for the usual high dose hook effect (Wild, 2013), where a single equilibrium binding process operates, the kinetic hook effect requires a second process to convert sensors from the closed, signal-on state, to the open signal-off state. We hypothesize that here this process is DNA strand displacement. Further we hypothesize that analyte binding to the lily pad is slower than intramolecular closure (where the analyte engages a second binder on the sensor). Thus our picture is that fast binding of an analyte molecule to one binder of the lily pad is followed by faster intermolecular closure. At high concentration this results in an out-of-equilibrium situation which can be relaxed by the slow strand displacement of a single DNA analyte within a closed lily pad, and which results in an open lily pad with two bound analytes. On this picture, the kinetic hook effect is likely intrinsic to the DNA analyte rather than our sensor. For analytes that do not have displacement mechanisms it may not be observed; we have not observed this effect for two protein analytes (streptavidin and PDGF-BB) but we may not have examined high enough analyte concentrations. We note that for these DNA-sensing lily pads, the kinetic hook effect limits the upper limit of quantification, rather than signal saturation.

2.7 Optimizing a Multimeric Protein Detector

Because of the lily pad's modularity, it is trivial to modify into a detector for multimeric proteins with multiple identical binding sites. As a proof-of-principle (Figure 2.5), we prepared lily pad sensors for detection of a model multimeric

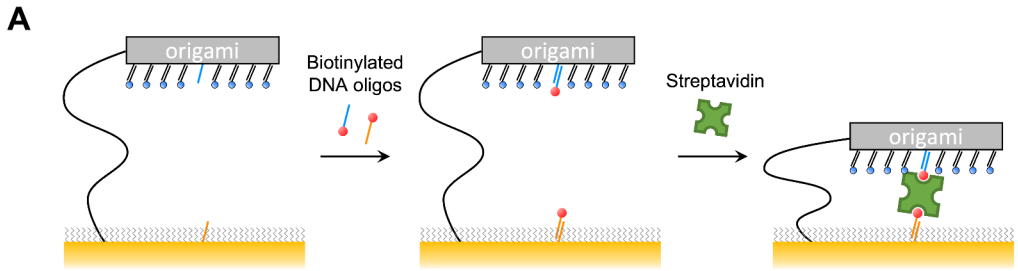
A
origami
Biotinylated
DNA oligos
origami
Streptavidin
origami

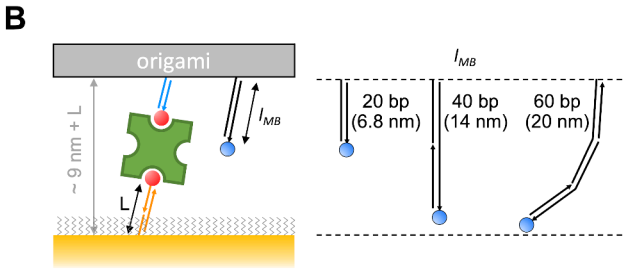
B
origami
~ 9 nm + L
L
I_{MB}
I_{MB}
20 bp
(6.8 nm)
40 bp
(14 nm)
60 bp
(20 nm)

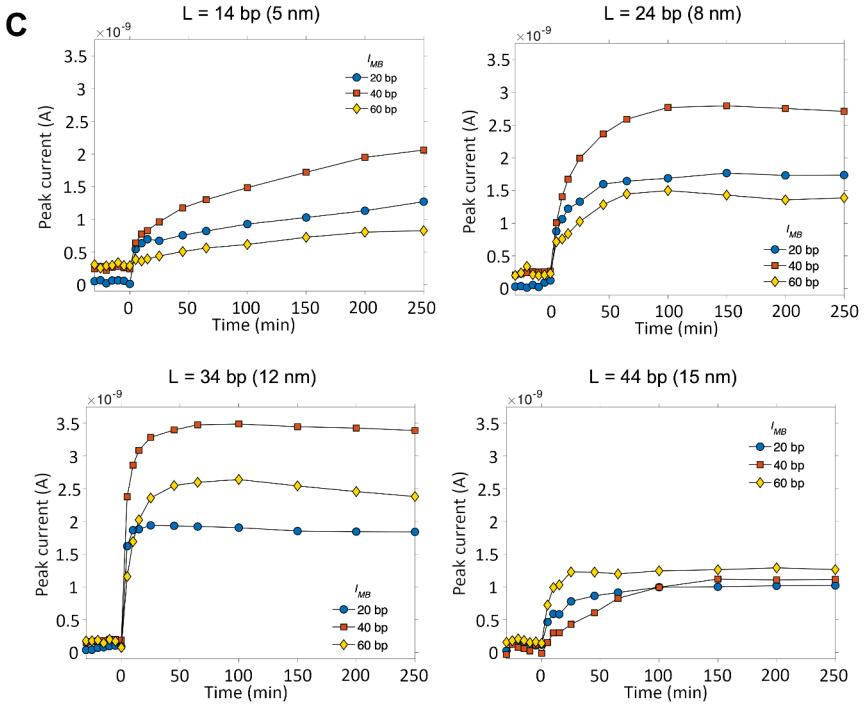
C
L = 14 bp (5 nm)
L = 24 bp (8 nm)
L = 34 bp (12 nm)
L = 44 bp (15 nm)
Peak current (A)
Time (min)
$\times 10^{-9}$
I_{MB}
20 bp
40 bp
60 bp

protein, streptavidin. We achieved this by simply adding two biotinylated adaptor strands to our basic DNA-sensing chips (Figure 2.5A): the first adaptor, sequence x, was complementary to the 14 nt ssDNA tail (x') on the origami; the second, sequence y, was complementary to the 14 nt oligos (y') on the surface. Thus chips with the lily pads used for ssDNA detection were incubated with the biotin-modified adaptors to obtain streptavidin detectors. To optimize sensor design, we measured sensor response as a function of both surface linker length (L = 14, 24, 34, or 44 bp) and MB curtain length (l_{MB} =20, 40, or 60 bp).

Because it is measured before streptavidin addition when the lily pad is nominally open, the baseline was expected to be independent of curtain length. However, the baseline (Figure 2.5C) was almost always higher for l_{MB} = 40 and 60 bp than for 20 bp (only for L = 44 was the 40 bp baseline slightly smaller than the 20 bp baseline). Part of the baseline is thus apparently due to transient sticking of the curtain to the surface. To account for longer curtain's enhanced stickiness, we suggest that either (1) longer curtains access MB configurations which are individually stickier, *e.g.* with more MB contacting the surface or (2) longer curtains have an increased total number of weakly-sticky MB configurations.

When streptavidin was added to l_{MB} = 20 bp sensors, the SWV signal quickly increased, reaching ~50% or more of the final signal change within 5 minutes after streptavidin addition. For each $L \leq 34$, comparatively slower on-signal kinetics were observed for l_{MB} = 40 bp and 60 bp sensors. The slower kinetics observed

---

Figure 2.5 (*preceding page*): **Lily pad sensors for DNA can be readily converted into protein sensors and their response rationally optimized.** (A) Two biotinylated ssDNA adaptors are hybridized to the sequences x and y on the origami and on the surface to create a streptavidin sensor. (B) Different lengths for the MB-modified DNA curtain, l_{MB}, and dsDNA linkers for the surface biotin, L, were created to study the effect of molecular design on sensor behavior. (C) SWV sensorgrams for streptavidin (500 pM) detection with various MB curtain lengths (20, 40, and 60 bp) on origami and dsDNA linker lengths (14, 24, 34, and 44 bp) on the surface. Different l_{MB} and L give qualitatively different results for both on-signal kinetics and endpoint signal. Longer MB curtains increasingly disturb the closing of the lily pads, but at the same time bring MB closer to the gold surface, increasing peak current; the origami shape itself may have a steric clash with the surface that changes with the length of the analyte-binder complex. The maximum in peak current (40 bp for L = 14, 24, 34, and 60 bp for L = 44) as a function of curtain length is likely set by the tensions between these three effects. Overall, a 40 bp MB curtain and 34 bp surface linker yields the largest signal change.

for 40 and 60 bp MB curtains (most noticeably for $L = 14$) was similar to that observed for detection of the 28 nt DNA reversed sequence, *yx* (Figure 2.3A), and we interpret it similarly, *i.e.*, we believe that the longer MB curtains sterically hinder sensor closing. However, at $L = 44$, the analyte-binder complex has moved curtains of all lengths sufficiently far from the surface that steric effects are minimal; $l_{MB} = 60$ bp curtains, extending closest to the surface, gave the fastest kinetics.

We expected to see the largest effect of sensor design in peak current endpoints; some experiments showed small decreases in peak current after extended interrogation and so we compared maximum peak currents (MPC) over the 250 min experimental window. Our goal was to optimize signal change and our hypothesis was that trends in sensor performance should be interpretable in terms of the difference δL between the total size of the binder-analyte complex and the MB curtains. In an optimal sensor design, the closed lily pad conformation should bring the redox reporters as close as possible to the surface without a steric clash. Absent any tilting of the curtain strands, one might expect to see steric clashes for $\delta L < 0$. In our DNA sensor above, a 28 bp analyte-binder complex (9.5 nm) was used with a 20 bp MB curtain (6.8 nm) that was slightly shorter (by $\delta L = 2.7$ nm); in this configuration (Figure 2.3) the DNA sensor achieved an MPC of 2.75 nA. Table S6 gives δL and MPCs for all conditions in Figure 2.5C. For three of the four conditions (cyan and yellow; Table S6A) with δL most similar to the DNA sensor (< 1.8 nm different), MPCs were $\geq 75\%$ that of the DNA sensor. But a fourth condition was only 45%. Further, four pairs of conditions having the same δL (but different L and l_{MB}) had markedly different MPC. This analysis shows that δL alone is not a good predictor of MPC.

Instead, observe that for *all three curtain lengths* (and thus a wide range of δL), MPC has a maximum for $L = 34$ before steeply dropping off for $L = 44$. At this boundary, the ranking of which MB curtain length gives the highest MPC also abruptly changes. Taken together, these observations suggests that there is some other steric effect, which changes sharply between $L = 34$ and $L = 44$, and which couples to the steric effect of the MB curtain length. Otherwise we would expect a stronger correlation between MPC and δL across the boundary. In particular we would expect an increase for the MPC of 60 bp curtains as L changes from 34 to 44, where δL goes from 0.92 nm to 4.3 nm. Rather we see a drop in MPC from 2.6 nA to 1.25 nA—for comparison, a large δL of 14.5 nm still achieves an MPC of 1.9 nA for 20 bp MB curtains at $L = 34$.

We propose that the origami shapes exhibit either large deformations (either static

or dynamic) from a flat disk, on the order of $\sim$ 21 nm in height (the size of the analyte-binder complex for $L = 34$). One possible source of deformation is that the MB curtain causes the origami to curl into a U-shaped cross-section that bends up and away from the surface: simulations of origami with MB curtain-like extensions predict such deformations at the 20 nm scale (see Chapter 3 and Sample et al., 2024); similar-sized fluctuations of 2D origami have been observed experimentally (Ni et al., 2022). Perhaps for $L = 34$ and below, these deformations allow MB curtains of any length to contact the surface, and so increasing L up to 34 decreases steric interference between the MB curtain and the surface. By $L = 44$ (corresponding to an analyte-binder complex of 25 nm), all curtain lengths are held too far from the surface for deformations of the origami to bring them into contact. The longest curtains (60 bp, $\sim$ 20 nm) give the highest MPC at $L = 44$, as they position MB closest to the surface in this "non-contact" regime.

While the dependence of sensor performance on the size of the analyte-binder complex and the MB curtain length is not as simple as we first envisioned, it is nevertheless intelligible. The library of linker and curtain strands we have developed are analyte agnostic. Thus our experiments provide a procedure and map for how sensors for other analytes can be optimized.

Having determined that the optimal (highest MPC) lily pad design for streptavidin detection has a 40 bp MB curtain and $L = 34$ bp linker, we sought to assess the linearity of this sensor and measure its sensitivity (LoD). We thus challenged this design with concentrations of streptavidin, ranging from 1 pM to 1 nM (Figure 2.6). Signal change was plotted as a function of the streptavidin concentration in Figure 2.3 on a semi-log scale. The signal increased monotonically from 2 pM up to 1 nM, with log-linear behavior observed between 5 pM and 1 nM. Using these data, we estimated the limit of detection (LoD) by the conventional, wherein $\mu_0 + 3\sigma_0$ is the signal at the LoD concentration, σ_0 is the standard deviation of the blank ([streptavidin] = 0) and μ_0 is the mean of the blank. Here $\mu_0 + 3\sigma_0 = 8.0\%$, where $\mu_0 = -7.0\%$ is sensor baseline in the absence of streptavidin (Figure 2.6, red dotted line). Because [streptavidin] = 1 pM gives a signal change (17%) that is significantly larger than 8.0%, we infer that LoD < 1 pM.

As observed with the sensor for the ssDNA analyte *xy*, the gains reported for our optimized streptavidin sensor are unprecedented for a reagentless, unamplified, single-step electrochemical sensor. When challenged with 500 pM streptavidin in bulk solution (Figure 2.5C), at steady state measurements past 50 minutes, gains for

the 40 bp MB curtain and L = 34 bp linker system were greater than 1600%. For experiments where the linearity of the sensor and LoD was determined (Figure 2.6), gains at the same streptavidin concentration were calculated to be greater than 500%. We believe this difference is a function of the experimental conditions. For the steady state measurement, the electrochemical cell was left undisturbed with a large volume of bulk analyte solution (1 mL) and repeatedly interrogated over time. For the linearity/LoD measurement we (1) sought to model a situation with smaller, more practical sample volumes and thus used 10 µL rather than 1 mL, (2) sought to recycle chips and thus made multiple repeated measurements on the same chip, (3) sought to model an assay in which spuriously-bound sample molecules are washed from the sensor before measurement, and thus the chip was washed with buffer before each baseline and each streptavidin measurement.

The remarkable size of our sensor's gains becomes clear through comparison with previously-published systems. In comparison to our system, interrogation of other electrochemical streptavidin sensor platforms in buffered solutions gave maximal gains that were *at least an order of magnitude smaller* than our maximal lily pad gains. Furthermore, these other platforms' maximal gains were typically reached at significantly higher analyte concentrations. For example, a duplex E-DNA-like sensor displaying biotin gave maximal (in terms of magnitude) gains from -50% (signal-off) to +50% (signal-on) at 3 nM streptavidin (Cash, Ricci, and Plaxco, 2009). A modified version of this platform that relies on surface-based steric hindrance, gave -60% at 100 nM streptavidin (Mahshid, Camiré, et al., 2015). A DNA junction-based sensor gave -50% at 500 nM (Somasundaram and Easley, 2019), and a modular, bivalent Y-shaped structure gave -43% at 100 nM (Idili et al., 2022). In addition, our sensor's LoD, $<$ 1 pM, represents an improvement of *at least two orders of magnitude* over the LoD of the streptavidin sensors described above. Given these dramatic gain and LoD improvements over existing sensor designs, we believe that the lily pad architecture offers a generalizable platform for high-sensitivity, high-gain measurements of analyte concentration.

2.8 Lily pad sensor regeneration

The biotinylated DNA adapter strands were redesigned to have an additional 5 nt ssDNA toehold (Figure 2.7, Table S3). This enables their removal via toehold-mediated strand displacement (Yurke et al., 2000): a solution containing two 19 nt invading strands (Table S3) whose sequences are fully complementary to the extended adapter strands is applied to the surface; subsequent strand displacement

reexposes the 14 nt DNA-sensing tail (x) on the origami and the DNA sensing thiolated ssDNA (y) on the surface. Using a 100 nM concentration of applied invading strands, the analyte is displaced in 10 minutes; addition of 500 pM biotinylated adapter strands regenerates the sensor for further interrogation.(Figure 2.7B). We conducted four rounds of sensing, displacement, and regeneration in this manner, and the sensor responded to streptavidin with similar kinetics after each cycle.

However, it was observed that this process does not completely restore the sensor to its original state; up to ~5% loss in on-signal was seen after each round of regeneration (Figure 2.7C). To explain this loss, we suggest that either (1) incomplete strand displacement leaves some streptavidin-biotin complex bound either to the origami or on the surface, blocking analyte binding sites in subsequent sensing rounds or (2) thiolated y may desorb from the surface. A third alternative is that (3) MB-strands or even entire lily pads are released with each regeneration; however this is inconsistent with our observation that the raw baseline sensor signal did not decrease through rounds of regeneration. To achieve greater sensor durability, strategies to increase the efficiency of toehold strand displacement (Simmel, Yurke, and Singh, 2019) and improve the robustness (Clark, Pellitero, and Arroyo-Currás, 2023) of gold-bound thiolated sensors to desorption could be applied.

2.9 PDGF-BB detection

To further demonstrate the modularity of the lily pad sensor and to test its capability for detecting larger analytes, DNA adapter strands were designed to display an aptamer that binds (Figure 2.8). Since the design of the sensor requires two binding events, one to the origami and one to the surface, PDGF-BB was chosen as the analyte due to its homodimeric nature, which allows for the same aptamer to be used on both the origami and the surface. Surface preparation and origami folding were performed as for previous designs, and adapter strands were added after origami had been tethered to the surface, as with the streptavidin sensor. The two adapters (Figure 2.8A) were designed to have sequences x' and y', followed by a previously reported 36 nt aptamer with an apparent binding affinity to PDGF-BB of 36 fM (Vu et al., 2017). The resulting sensor achieved detection of PDGF-BB at concentrations as low as 500 pM (Figure 2.8B), with a signal change of 20%. Sensor signals were stable after PDGF-BB addition for over 100 mins of serial monitoring every 5 min, highlighting the functional stability of lily pad sensors. The lowest concentration measured is within one order of magnitude of the best sensitivity achieved for previously reported aptamer-based PDGF-BB sensors (Lai, Plaxco, and Heeger,

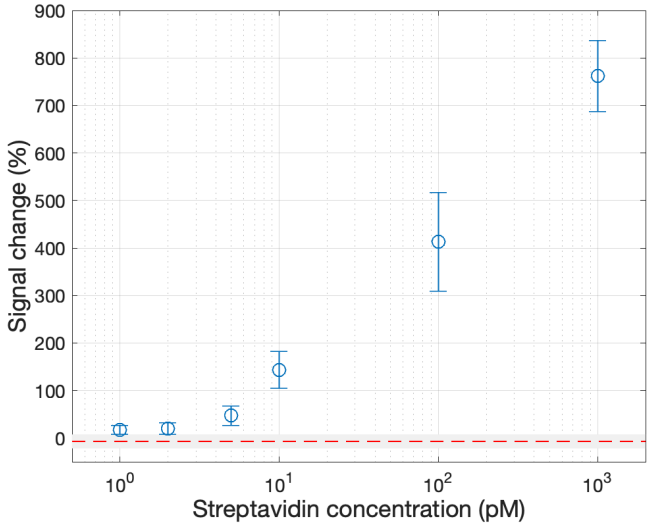

Figure 2.6: **Lily pad sensors can quantify picomolar protein concentrations**. SWV signal changes were measured for lily pads having 40 bp MB curtains and L = 34 bp linkers using six streptavidin concentrations from 1 to 1000 pM and a blank (zero analyte). Mean and standard deviation for each concentration were calculated from replication using five different chips (five biological replicates). On each chip, the off-signal (before sample application) was measured five times and averaged (five technical replicates). After sample application and incubation (one hour, 34°C) the on-signal (endpoint signal) was measured five times and averaged (five technical replicates). Signal changes in the interval $\mu_0 \pm 3\sigma_0$ are shaded gray, where μ_0 is the mean of the blank and σ_0 its standard deviation. LoD < 1 pM.

2007). However, we note that because the goal of these experiments was simply to demonstrate platform modularity, no efforts were made to co-optimize the aptamer and sensor (*e.g.* matching aptamer size and MB curtain length); there is therefore potential to improve the sensitivity of the PDGF-BB version of the lily pad sensor in future work.

2.10 Discussion

Using DNA origami, we designed and fabricated a nanodevice—the lily pad—and developed it to create a single-step, reagentless biosensor platform whose modularity enables it to detect arbitrary DNA sequences and proteins through electrochemical measurements. We showed that the modularity of our DNA origami sensor allows the sensing of analytes of varied size and binding properties via simple addition of a few unmodified oligo strands to the base sensor system. The conformational change required for signal is built into the architecture of our sensor, obviating the need to

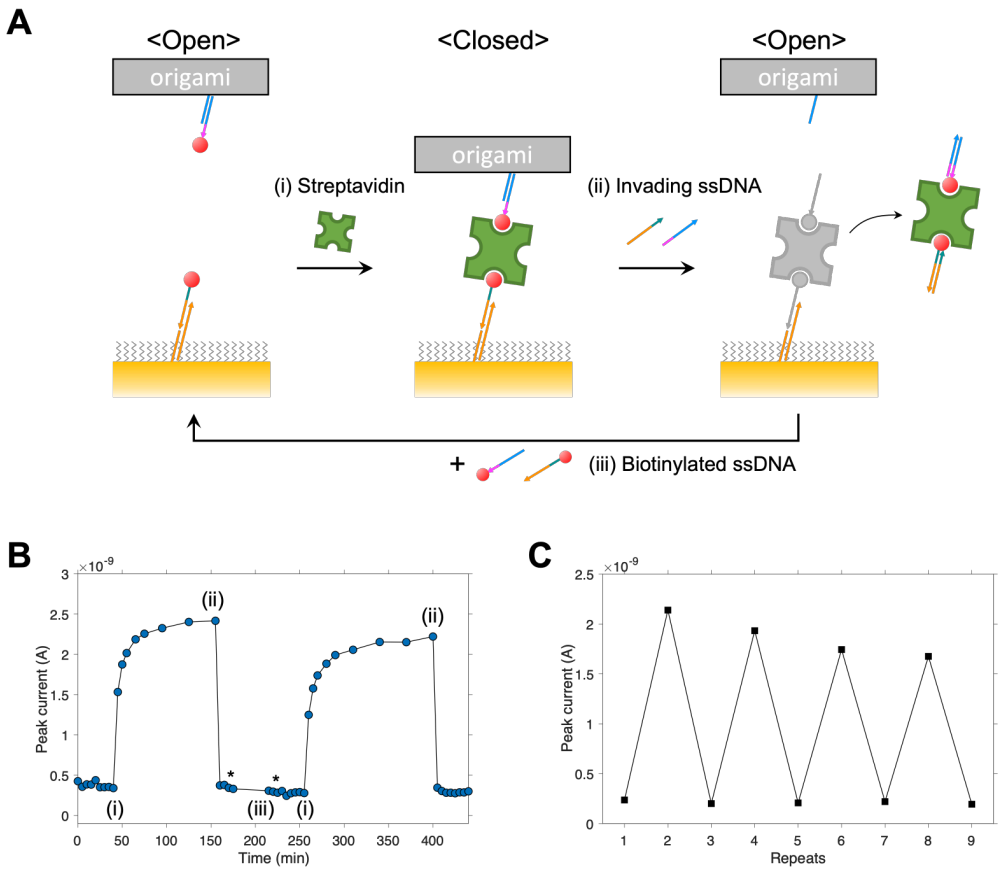

Figure 2.7: **Lily pad sensors with tightly bound analytes can be regenerated multiple times.** (A) Schematic shows a lily pad being closed by streptavidin (i), reopened by ssDNA invaders via strand displacement (ii), and regenerated by the addition of new biotin-modified adaptors (iii). (B) Sensorgram demonstrating two rounds of streptavidin detection where notations are made for buffer washes (*) and the addition of 500 pM streptavidin (i), 100 nM invaders (ii), and 500 pM biotinylated adaptor strands. (C) Changes to SWV signal through four rounds of lily pad regeneration. In each round, streptavidin solution (10 µL, 500 pM) was reacted for one hour at 34°C before a measurement was taken (high values). Lily pads with 40 bp MB reporters and L = 34 bp were used for (B) and (C).

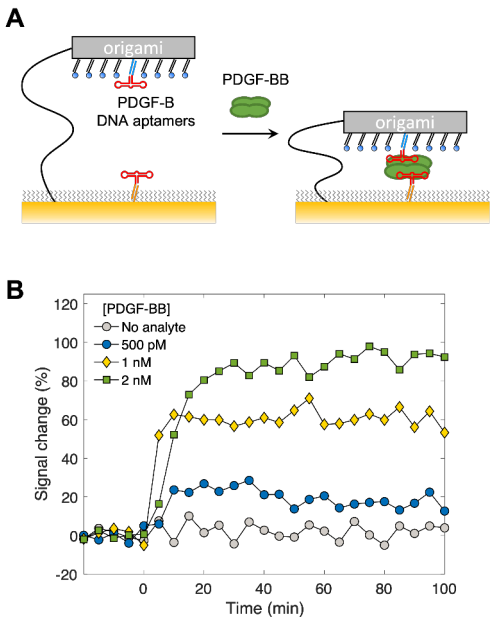

Figure 2.8: **Lily pad sensors can be adapted to detect a clinically-relevant protein biomarker.** (A) We functionalized lily pad sensors with platelet-derived growth factor (PDGF) binding aptamers. The length and sequence of x and y adapters were identical to those used in Figure 2.5C, as was the sensor preparation and interrogation protocol. (B) Here we show the continuous interrogation of the lily pad PDGF sensor before and after independent addition of three protein concentrations at t = 0 min. The root mean square of the baseline (*i.e.*, no PDGF) is ±7‰. Relative to this baseline, the signal to noise ratio (SNR) for each protein challenge is $SNR_{0.5nM}$ = 2.8, SNR_{1nM} = 8.5 and SNR_{2nM} = 13. Lily pad sensors were interrogated every 4 min via SWV, using parameters indicated in the SI.

find or engineer binders that undergo a conformational change. Thus the versatility of our sensing platform should only be limited by the ability to functionalize the binding sites of the lily pad. The lily pad can be trivially modified to use the large variety of available aptamers (Keefe, Pai, and Ellington, 2010; Zhang, Lai, and Juhas, 2019). Conjugating oligos to other binder classes such as antibodies, antibody fragments (Nelson, 2010), nanobodies (Harmsen and De Haard, 2007), or peptides (Wada, 2013) will allow for their facile incorporation into the lily pad. Whenever it is difficult or simply too expensive to get two binders from the same class, hybrid sensors mixing binders from two classes, *e.g.* antibodies and aptamers (Jarczewska and Malinowska, 2020), could be used. Larger binders and/or larger analytes may be accommodated by longer MB curtains or redesign of the lily pad geometry to provide a pocket for the analyte-binder stack.

In all versions presented here, the lily pad sensors use two binders. In this sens-

ing modality, lily pads can be customized to detect any analytes which are either multimers (for which both the origami and the electrode present the same binder), or have two distinct epitopes (for which the origami and electrode present distinct binders). To access the sensing of analytes with only one available epitope (*e.g.* small molecules and some proteins), an appropriate split aptamer (Debiais et al., 2020) or aptamer switch (Rangel et al., 2020; Yang, Pei, and Stojanovic, 2016) could be incorporated into the lily pad. In the case of a split aptamer modality, one half of the aptamer would be attached to the origami, and the other half would be attached to the electrode. Analyte binding to both halves would create a bridge and close the lily pad. In the case of an aptamer switch modality, an aptamer re-engineered to have an "antisense" domain (White, Rowe, and Plaxco, 2010) partially complementary to the analyte-binding region of the aptamer would be attached to the origami. A sequence complementary to the antisense domain would be attached to the electrode. Upon analyte binding of the aptamer, the antisense domain would be displaced and bind to its surface complement, thus closing the lily pad. Capture SELEX (Stoltenburg, Nikolaus, and Strehlitz, 2012; Yang, Pei, and Stojanovic, 2016) naturally generates switching aptamers with an appropriate antisense domain, and would obviate the need for aptamer re-engineering. Overall, however, split aptamer and aptamer switch modalities would add significant complexity, and can have a poor success rate for some targets (Yang, Pei, and Stojanovic, 2016); thus we expect that aside from the case of small molecules, a sandwich modality will be the preferred format for lily pad sensors.

The modularity of the lily pad provides benefits beyond simply altering the sensor's target specificity: *e.g.* we used a library of swappable linkers and curtain strands to optimize sensor performance. Through this approach, we obtained ssDNA (Figure 2.3) and streptavidin sensors (Figs. 3 and 4) that can translate picomolar-range changes in analyte concentration to many-fold changes in signal, achieving gains that significantly surpass existing E-DNA/E-AB sensors. The same library could be used to optimize gain and LoD of lily pad sensors that use any of the binders or sensing modalities (sandwich, split aptamer, or aptamer switch) described above.

Beyond sensor optimization, modularity enables practical chip and sensor reuse. When testing different lily pad designs, we reused chips over ten times by simply treating them with hot water to remove one sensor from the surface linkers, and then adding a new sensor.

Similar to E-AB sensors, our platform is reagentless and signaling relies on target-

binding induced conformational change—it thus has the potential to work in complex biological matrices, *in vivo* and ultimately in awake behaving animals. Achieving this potential will require strategies to increase the lifespan of the electrode and monolayer in serum (Watkins et al., 2023). Hardening origami to nuclease degradation, low Mg^{2+} concentrations, and nonspecific binding *in vivo*, while maintaining its structure and functionality, would also be necessary. Such hardening has been achieved by a variety of methods (Chandrasekaran, 2021) including increasing helical packing density, chemical cross-linking, coating with block copolymers, and functionalization with unnatural nucleotides and end-groups; these methods should translate readily to the lily pad.

Contrary to conventional biodiagnostics, such as lateral flow assays, ELISA, qPCR, and more, our platform is designed to perform real-time measurements of analytes in biological samples. This is achieved through an intramolecular and reagentless design, where analyte addition is the only step required after fabrication and before measurement. Once the lilypad has been hardened for *in vivo* applications as described above, the sensor could be placed in the bloodstream and it would continuously measure dynamic concentrations of target, until the electrode is degraded. This is achieved through the use of reversible binders, which will equilibrate over time to the concentration of analyte in solution, responding to its changes. In many conditions real-time measurement is extremely valuable, especially when an event is expected and a timely reaction is valuable, for example in glucose monitoring, or sepsis recognition. Generally, not every application requires such a granular level of detail and this is no one-size-fits-all solution. Lateral flow assays are still likely to be cheaper and adequately reliable for conditions where a yes/no answer is all that is needed, while ELISA and qPCR still have unmatched sensitivity when measuring a single time point.

Other real-time sensing techniques for *in vivo* use have been demonstrated for several applications. Continuous glucose monitoring (CGM) has rapidly become the standard of care for diabetic patients (Mihai et al., 2021). Early generation devices use electrochemical readouts through invasive, implantable electrodes. While sensing happens through enzymatic reactions, very differently from our lilypad design, the implantable needles are electrodes much like the ones we used and many of the same issues and solutions apply. Particularly, a recent trend in CGM has been to move away from invasive sensing to avoid issues of protein adsorption and increase the lifetime of the device from a few days to several weeks. This gives us a clue that,

even when hardened and optimized, we should expect the lilypad sensor to be useful in applications where only short-term sensing is necessary. Unfortunately, non-invasive CGM techniques usually rely on specific physical and chemical property of glucose, for example its response to specific electromagnetic frequencies (Wu, Liu, et al., 2023), with approaches that cannot be easily generalized for other targets. Additionally, one reason why glucose is relatively easy to detect is its millimolar concentration in biological fluids Klonoff, Ahn, and Drincic, 2017, compared to other targets like the ones we explored that are more likely to be in the nano- to picomolar range.

One of the few continuous sensing approaches that have proven successful, is the one shown in Arroyo-Currás, Somerson, et al., 2017, where E-AB sensors are implanted in ambulatory animals to monitor the concentrations of different small molecules. A few other continuous monitoring technologies exist for specific targets, such as lactate (Freeman et al., 2023) and serotonin (Ahmad, Andrade, and Song, 2023), but even these rely on specific properties of the analyte molecules and cannot be easily generalized. More general techniques that show promise when measuring in buffer, such as optical analysis of particle motion (Buskermolen et al., 2024) or organic field effect transistors (Yun et al., 2014), have not translated successfully to *in vivo* applications as hardening and anti-fouling approaches have either not been tested or proven difficult (Vaisocherová, Brynda, and Homola, 2015).

Finally, the lily pad design is not limited to electrochemical readout; any readout modality for which signal can be generated by a conformational change should work. With potential modification to the reporter molecules, energy-transfer based fluorescence, surface plasmon resonance, biolayer interferometry, and field effect techniques would all serve as effective readouts for the molecular architecture we describe.

2.11 Methods

dsDNA linker preparation

For synthesis of double-stranded DNA linkers with defined length and single-stranded overhangs with specific sequences, we performed two sequential PCRs, extension and autosticky PCRs (see Gál et al., 1999 and Appendix C), using Lambda DNA purchased from Promega (WI) and Taq polymerase from New England Biolabs (MA). In the extension PCR, each of the DNA primers (sequences in Table C.1), purchased from IDT (CA), consists of a 20 nt long template-binding region that

determines the length of the linker and another 20 nt long extension region that determines the terminal sequences of the amplicon added to the sequence from the template DNA (Figure C.1, top). The amplicons from the first PCR, after purification by agarose gel extraction using Zymoclean Gel DNA Recovery Kits purchased from Zymo Research (CA), were used in the second autosticky PCR as template DNA. Each of the primers used in the autosticky PCR (Figure C.1, bottom) contains two domains separated by an abasic site, a 20 nt long template-binding region, identical to the extended sequence in the first PCR, and an overhang sequence chosen for binding to either the flat DNA origami or gold surface. The PCR products were purified using the DNA Clean and Concentrator Kit from Zymo Research and stored in 10 mM Tris buffer (pH 7.4) at -20°C.

DNA origami design and folding

The DNA origami we used to prepare the lily pads is derived from a structure used in earlier work (Gopinath et al., 2021), which was designed in cadnano (Douglas, Marblestone, et al., 2009) to be a flat, circular shape with a square opening. In that work the square opening gave the design a specific orientation on a microfabricated surface; here the square opening is irrelevant. For the purposes of this work, the design was modified so that extensions of staples on the 5′ end would all appear on the same side (Figure 2.9). Most staple strands (see Table S5 for sequences) were ordered from IDT unpurified at 100 μM in water and stored at -20°C. To introduce an analyte binding site near the center for DNA sensing experiments, one staple strand was replaced by a new DNA oligo (IDT, PAGE-purified) that has a 14 nt long 5′ extension (shown in cyan in Figure 2.9). To create 20 bp MB curtains: (1) 70 out of 234 total staples were extended on their 5′ ends with a common 20 nt long single-stranded linker and (2) an MB-modified DNA strand (IDT, dual-HPLC purified) with a sequence complementary to the 20 nt linker was hybridized to all 70 extended staples.

When preparing the lily pads with longer MB curtain lengths (40 or 60 bp) for streptavidin sensing experiments, slightly different schemes were used, as shown at right in Figure 2.5B. For 40 bp curtains: (1) a 40 nt MB-modified strand (IDT, Dual-HPLC purified) was hybridized to the standard 20 nt extension, and (2) a single 20 nt "cap" ssDNA strand was hybridized to the 3′ end of the MB-modified strand to create a fully duplexed curtain. For 60 bp curtains, origami were functionalized with 40 nt extensions that hybridized the 40 nt MB-modified strand via the same 20 nt overlap used for 40 bp curtains. This meant that to create a fully duplexed

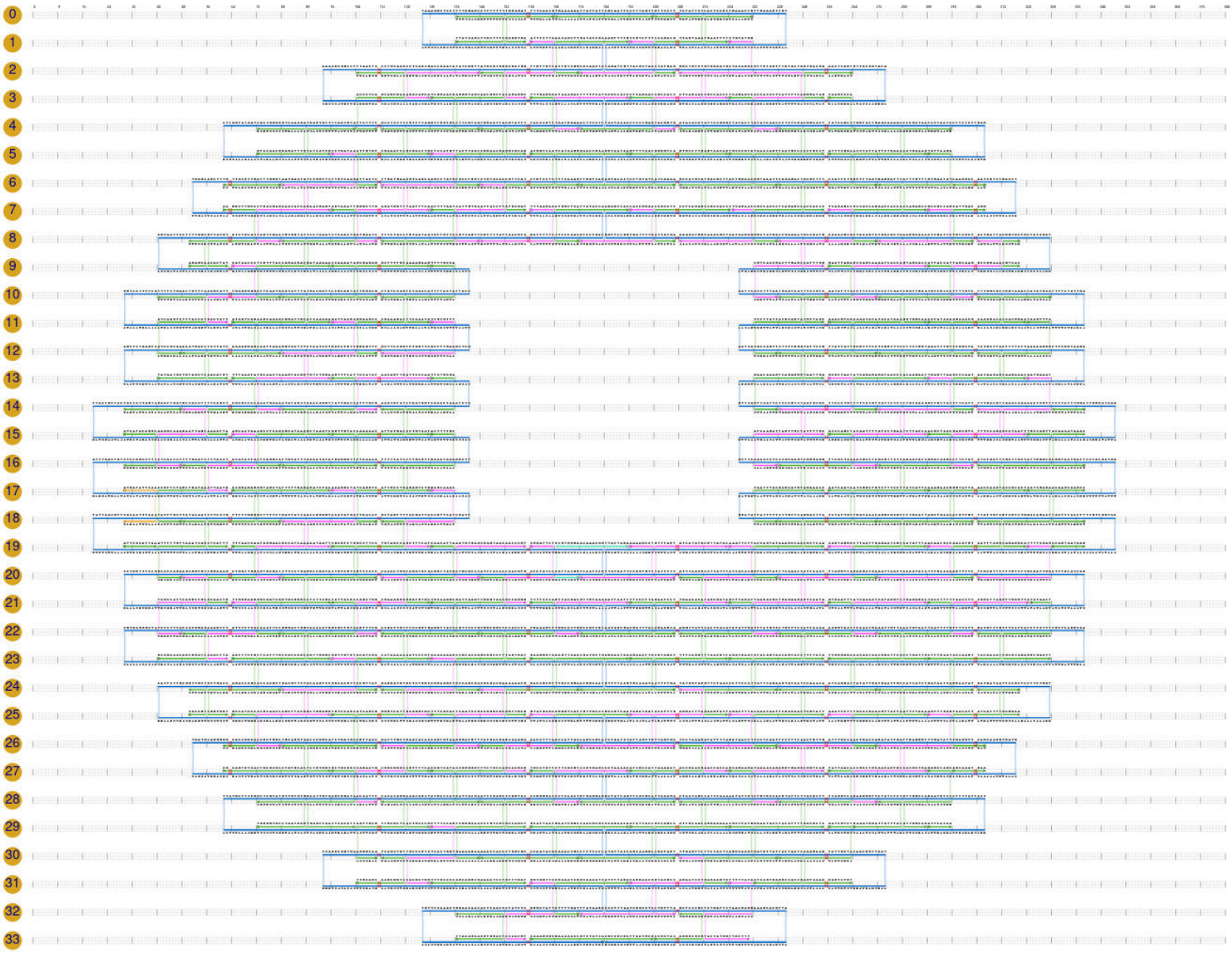

Figure 2.9: **Design of the DNA origami** Here the 70-MB variant of the origami used for sensor experiments is depicted. Strands that were modified with 5′ linker extensions, and subsequently bound by MB reporter strands are colored pink. A single staple which was modified with an extension to enable installation of a binder is depicted in cyan (helix 19, at the center). During origami folding, one staple, is omitted from the mixture (the yellow-orange staple in helixes 17 and 18 at center left). This is the position at which one end of the dsDNA linker binds scaffold. The remaining staples are colored green. Visualized using scadnano (Doty, Lee, and Stérin, 2020).

curtain, both the 20 nt cap described above, a second 20 nt cap were used (where the second cap was hybridized to the section of the staple extension that was proximal to the origami).

To synthesize origami, we mixed 8094 nt long scaffold strands (p8094 from Tilibit, Germany), with the staple strand mixture, MB-modified DNA oligos (IDT), and the dsDNA linker from PCRs to the final concentrations given in Table 2.1 (1:1 scaffold:linker, 5 nM each). One staple on the left side of the origami (yellow orange in Figure 2.9) was omitted to leave a position on the scaffold at which the dsDNA linker overhang could bind. Throughout this work, we refer to 1× TAE buffer (Bio-rad, pH 7.5) with 12.5 mM $MgCl_2$ as "TAE/Mg". 100 µL of scaffold/staple/linker mixture in TAE/Mg was heated to 90°C for 5 min and annealed from 90°C to 20°C at -1°C/min. The final concentration of origami, based on the initial scaffold concentration was 5 nM and the solution was then diluted for use to 2 nM in TAE/Mg buffer.

Lily pads assembly on gold surface

We use the template-stripping (TS) method to prepare ultraflat (see AFM in Figure 2.10) gold surfaces as a substrate for lily pad sensors (Hegner, Wagner, and Semenza, 1993). First, a 200 nm gold film was deposited on a 4 inch silicon wafer (University Wafers, MA) using a Labline electron beam evaporator (Kurt J. Lesker Company, PA) at the Kavli Nanoscience Institute Lab at Caltech. The wafer was then cut to 5×8 mm^2 chips by Dynatex GST-150 Scriber/Breaker. A 10×10 mm^2 glass coverslip (#2) was rinsed with acetone, isopropyl alcohol, and water, blown dry with nitrogen, and cleaned by oxygen plasma for 5 min in a PE-50 plasma system (Plasma Etch, NV). About 1 µL of UV-curable adhesive (Noland, No.61) was applied on a clean glass and a gold chip was placed on top of the adhesive. The adhesive was then cured via a long-wave UV irradiation for 1 hour (Weiss et al., 2007). Right before use, the silicon wafer was pried off the gold/adhesive/glass layers using a razor blade, exposing the ultraflat gold surface on a glass coverslip. To create a well and isolate the reactive area, a silicone gasket (Grace Bio-Labs Press-To-Seal silicone isolator, 2 mm diameter) was glued on top and copper tape was used to form an electrical connection.

Two thiolated DNA oligos were purchased from IDT, one for analyte binding (5′-HS-TTTTTAGCTTTGATATCTG-3′) and the other for origami-linker tethering on gold (5′-CGTAAACCCAGCGTCTTCACCACGATGAATACTCCCACCG-

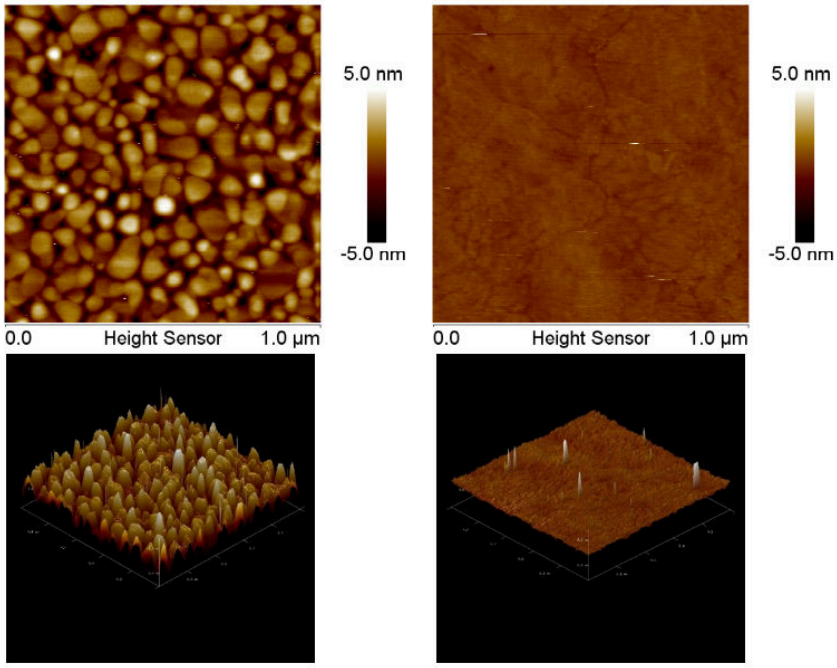

Figure 2.10: **AFM of gold surfaces.** Electron-beam deposited gold surfaces (AFM at left), commonly used in EDNA sensors, exhibit 20–100 nm diameter features up to 10 nm in height. EDNA sensors, typically a few nanometers in size, function well on these surfaces as they are much smaller than the features. On the other hand, template-stripped gold surfaces (AFM at right) have a much smoother and flatter profile. Apparent grain boundaries are often hundreds of nanometers apart and roughness is on the order of 1 nm. DNA origami are 100 nm in diameter, and relatively stiff. We reasoned that, to maximize signal in the closed state of the lily pad sensor, we should maximize the number of MB in close proximity to the surface, and we assumed that this would be best accomplished with a template-stripped gold surface; thus these are the surfaces we have used throughout this work. However, we have not compared the performance of the Lily pad on e-beam deposited and template-stripped surfaces.

TTTTT-SH-3′). In separate tubes, we mixed 1 µL of 100 µM thiolated DNA oligos and 1 µL of 10 mM tris(2-carboxyethyl) phosphine hydrochloride (TCEP, Sigma Aldrich) and incubated for 1 hour at room temperature to reduce the disulfide bonds. Then the solutions were mixed and diluted to 100 nM of each DNA in 1× PBS buffer (pH 7.4). 20 µL of the solution was introduced into a silicone gasket well on a freshly prepared TS-gold chip and a Teflon cell (CH instrument, TX) was assembled creating about 1.5 mL of reaction volume that allows three electrode connections. After 1 hour incubation at room temperature, the solution was exchanged with 50 µL of 10 mM 6-mercapto-1-hexanol (6-MCH, Sigma Aldrich) in 1× PBS buffer followed by overnight incubation at room temperature for formation of a passivating layer on the gold surface. After this step, the surface presumably had a random distribution of analyte binding and origami linker strands in a 1:1 ratio, with the spaces between these oligos filled by 6-MCH. The density of oligos on these chip surfaces was determined by binding a complementary methylene blue functionalized strand to the chip, and determining total methylene blue occupancy by cyclic voltammetry as shown in Figure 2.11.

When annealing the lily pad origami structure, we optimized the concentration of the dsDNA linker so that most of the linker was attached to the origami (Figure 2.2). In downstream steps, this allowed us to treat the amount of free linkers as negligible and use the annealed origami mixture without purification. After the passivation step, the 6-MCH solution was removed and 20 µL of 2 nM MB-modified lily pad solution was added in the reaction well of the silicone gasket and incubated for 30 min at room temperature for origami-linker placement on gold via 40 bp DNA hybridization. Then the gold surface was thoroughly rinsed with TAE/Mg to remove the unbound DNA origami, staple strands, and MB-modified DNA oligos.

Chips were reused (often more than ten times) by detaching the lily pads and analytes from the surface through rinsing with hot water (65 °C), by pipetting it directly onto the cell in 100 µL steps for a total of 15–20 times. We confirmed zero MB signal via SWV and cyclic voltammetry measurements after water rinsing.

Electrochemical measurements

A Metrohm PGSTAT 128N (Netherlands) potentiostat was used for SWV (see Appendix A for a discussion of the measurement technique). After equilibrating the cell at -0.15 V, SWV measurements were performed at a frequency of 10 Hz (see Figure 2.12 for optimization) with an amplitude of 25 mV between -0.15 V and -0.4 V

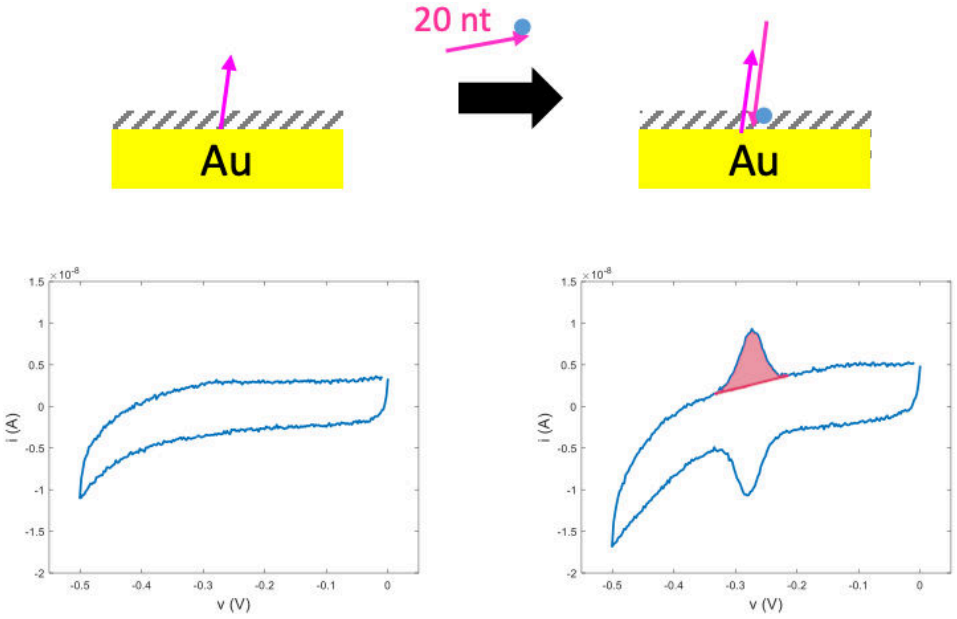

Figure 2.11: **Measurement of thiolated strand density on gold surfaces.** To estimate the packing density of thiolated strands, 20 ul a 15 nt thiolated strand at a concentration of 100 nM was deposited on a freshly template-stripped gold surface and incubated for an hour, before washing it off and interrogating the electrode via cyclic voltammetry. The electrode was then incubated with a partially complementary 20 nt strand with a methylene blue modification for 1 h, before rinsing and taking a second cyclic voltammetry measurement. The current peak in this second measurement was then integrated after subtracting the baseline, giving a charge measurement. This arises from the electrons transferred to the electrode from the methylene blue molecules as they are reduced. The charge can then be directly translated into the number of thiolated DNA strands on the surface, assuming full hybridization of the MB-labeled strands. Finally, knowing that template-stripped surfaces are ultra-flat, the surface area is estimated as the area of the silicone gasket. The density was measured on three different gold electrodes using this method and it was estimated to be 3.12 ± 0.034 e11 strands/cm^2.

relative to Ag/AgCl reference electrode in 1 mL of TAE/Mg at 34°C; temperature was controlled by using a Coy Labs glove box—without strict temperature control sensor response was too variable. SWV voltammograms were recorded every 5 mins for 1 hour before and 5 hours after the addition of analyte DNA, if not otherwise specified. The first hour of measurements before adding analyte is used to set the baseline, off-signal, and measure the fold-increase. To determine the peak current value a linear baseline is subtracted from the measurement and the MB peak is isolated. This peak is then fit to a Gaussian (Macfie, Atherton, and Compton, 2002) and its maximum value is recorded as the peak current (Figure A.1).

Frequency response of the sensor

The frequency response of electrochemical sensors (Dauphin-Ducharme, Arroyo-Currás, Kurnik, et al., 2017; White and Plaxco, 2010) is often used to (1) estimate the electron transfer rate of electrochemical sensors and (2) determine the operating frequency of the sensor for which sensor gain and signal-to-noise are optimized. The response of the system is measured by running square wave voltammetry measurements at different frequencies and plotting the peak currents divided by the frequency; this yields response values with units of $A \cdot s$ or charge. Such a plot is known as a Lovrić plot, or a volcano plot—the name volcano plot derives from the typical shape of these plots, which includes a single, volcano-shaped peak. The frequency at which the peak occurs can be used to derive an electron transfer rate for the sensor (Komorsky-Lovrić and Lovrić, 1995a,b).

For typical EDNA systems, in which a short MB-functionalized single-strand is hybridized to its complement on the surface, the peak in the volcano plot (and hence frequency of maximal electron transfer) typically occurs between 10 and 100 Hz. For our Lily pad sensor, the frequency response does not show a well-defined peak over the measured frequency range (1–1000 Hz) for either the open or the closed state. Instead, the response continues to increase as frequency decreases, and any peak likely falls outside of our measurable range. This suggests that, even when Lily pad sensor is closed and the MB are at their smallest distance to the electrode, the MB molecules do not come as close to the surface as they do in other EDNA system. Given the shape of the Lovrić plot and increased noise at frequencies less than 10 Hz, we chose an operating frequency (10 Hz) for the sensor that gives both good signal gain (between the open and closed states) and relative low noise.

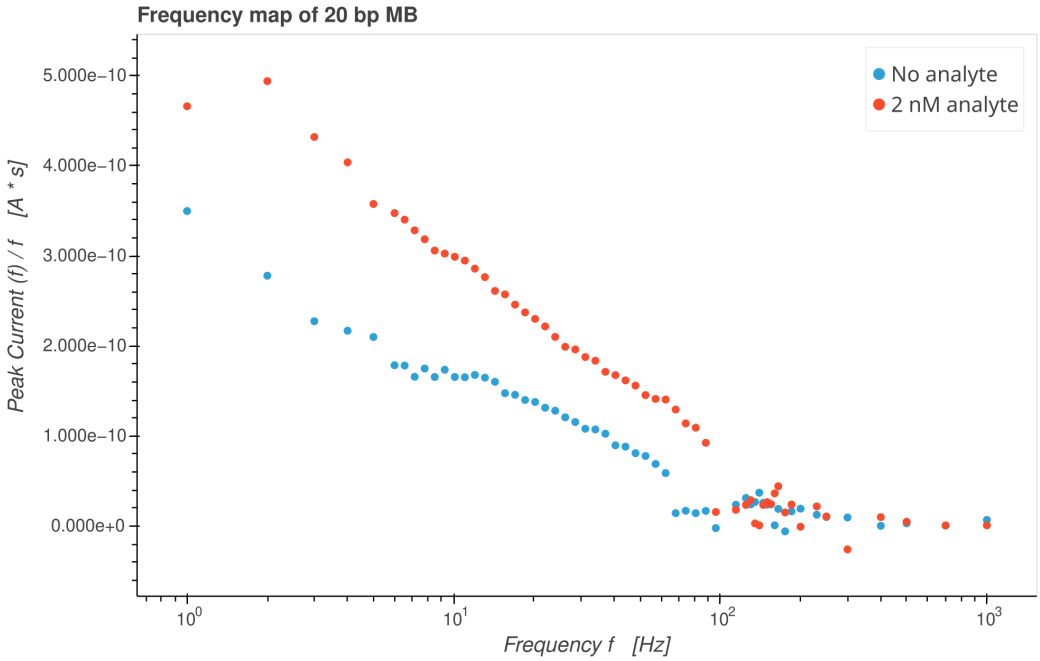

Figure 2.12: **Frequency response.** The frequency response of the sensor is evaluated using a Lovrić plot (also known as a volcano plot). The response in $A \cdot s$ calculated as the peak currents at a particular frequency, divided by that frequency. Unlike for usual volcano plots, no clear peak was observed and we used the plot to select a 10 Hz operating frequency for the sensor, as a compromise between signal gain and signal-to-noise. See Figure 4 of Komorsky-Lovrić and Lovrić, 1995b for an example Lovrić plot with a clear peak. On the vertical axis that work expresses our Peak Current$(f)/f$ $[A * s]$ as the dimensionless $(\Delta i_p/f)/\mu C$ where Δi_p is our peak current at a particular frequency f; note that $A * s = C$. The two plots in Figure 4 of Komorsky-Lovrić and Lovrić, 1995b show clear peaks as a function of f.

Streptavidin detection

Two biotin-modified strands were ordered from IDT, one to create a surface binding site, complementary to the DNA analyte binding thiolated strand (5'-Biotin-CAGATATCAAAGCT-3'), and the other to create a binding site on origami, complementary to the DNA analyte binding tail (5′-CTGAATGGTACGGA-Biotin-3′). The DNA sensing chip was incubated for 30 mins with 500 pM of each of these two strands in TAE/Mg at room temperature. This resulted in an $L = 14$ sensor. After rinsing with TAE/Mg, SWV measurements were performed for 500 pM streptavidin (Thermo Fischer Scientific) at 34°C in the same buffer.

To create streptavidin sensors with dsDNA surface linkers having a length greater than 14 bp (Figure 2.5C), we immobilized one of three different 3′-thiolated ssDNAs

(10, 20, or 30 nt long) instead of the standard 5′-thiolated sequence; we then performed a 6-MCH passivation step. Next, a 30 minute incubation was performed to simultaneously hybridize the lily pads to the surface, and add bridging strands where necessary. In particular, 5 µM of 24, 34, or 44 nt ssDNA bridging strands were added. The 5′ sequence of these strands was complementary to one of the 10, 20, or 30 nt ssDNA already on the surface (as appropriate), so they formed dsDNA complexes proximal to the surface; the 14 nt 3′ end of these strands projected ssDNA tails having the sequence y' into solution. In the next step where the biotin adapter strands (500 pM) were added, one of the adapters bound to the y' tails extending from the surface, forming dsDNA linkers with L = 24, 34, or 44 bp.

For LoD experiments in Figure 2.6, after rinsing off excess biotin-adaptor strands, we measured SWV signal five times before and five times after incubation with the relevant streptavidin solution on the chip; the pre- and post- binding signal for each chip was calculated as the mean of these values. Between the measurements, 10 µL of varying concentrations of streptavidin samples were introduced into a gasket well on the chip, and sealed with a piece of Parafilm to prevent sample evaporation. After 1 hour incubation at 34°C, chips were thoroughly washed with TAE/Mg buffer before the endpoint measurements. This process was repeated for 5 different chips per streptavidin concentration.

For regeneration experiments in Figure 2.7, two 19 nt biotinylated adapters (binding region + 5 nt toehold) were used, instead of our standard 14 nt ones. After a streptavidin measurement was finished, the chip was regenerated by adding 100 nM of 19 nt DNA strands that are fully complementary to the adapters, which displace them from the origami and surface sites, returning the chip to the DNA sensing configuration. To finish regeneration of the streptavidin sensor, the chip was incubated with new biotin-modified adapter strands (500 pM, room temperature, 30 min).

PDGF-BB detection

To create PDGF-BB detecting lily pad sensors, DNA aptamers for PDGF-BB protein (5′-CAGGCTACGGCACGTAGAGCATCACCATGATCCTG-3′) were ordered from IDT with two 14 nt extensions, one at 3′-end for binding to the thiolated DNA strands immobilized on gold surface (5′-CAGATATCAAAGCT-3′) and the other at 5′-end for the single-stranded DNA tail on origami (5′-CTGAATGGTACGGA-3′) that were used for the DNA analyte and streptavidin detection studies (see Table S3). PDGF-BB protein was ordered from PeproTech, Inc. (NJ). After preparing a stan-

dard DNA analyte detecting lily pad sensor, the chip was incubated with 1 nM each of the PDGF-BB aptamers with extensions in TAE/Mg at room temperature. The chip, assembled in a Teflon cell, was rinsed in the same buffer and connected to potentiostat. SWV measurements were performed as described above in 1 mL of TAE/Mg at 30°C. After recording SWV voltammograms every 5 mins for 1 hour, 0, 500 pM, 1 nM, or 2 nM of PDGF-BB protein in the same buffer was added.

Chapter 3

SIMULATIONS OF LARGE DNA ORIGAMI STRUCTURES

3.1 Introduction

As DNA nanotechnology achieved larger and larger structures, especially with the advent of DNA origami, interest arose in simulating their properties before folding, to avoid synthesizing hundreds of expensive strands only to discover deformations in the design. One of the first tools designed to predict the structure of DNA origami is CanDO (Castro et al., 2011; Kim et al., 2012). Solution of the structure is determined by basepair connectivity maps, using finite elements to model each basepair as a two-node beam with elastic and structural properties mimicking DNA. The output of the model is useful to determine global twists of the structure and areas under particular stress, introducing the option to iterate on the design before any DNA strand is ordered and the DNA origami is folded. It is especially useful to predict the structure of 3D DNA origami, where design rules were determined more empirically.

While CanDO is a very fast model, it focuses on structural properties and ignores much of what makes DNA unique, from sequence specific basepairing, to electrostatics and major-minor groove. The obvious alternative for a finer-grained simulation would be to use all atoms models, such as NAMD (Phillips et al., 2020), that take into account not only the DNA structure, but salt and solvent molecules around it. This is however extremely resource-intensive, with cost and time only increasing as the DNA origami become bigger. Additionally, models outputted by cadnano are not physically possible and need long relaxation steps before bond lengths and rotations could approach physical values and could be treated by the model. Relaxation potentials can be designed, as we will discuss later, but they require similar computational resources and this hinders the ability to rapidly prototype new designs. Furthermore, while all-atoms simulations can be necessary for enzymes with complex biophysics, it is unclear if most DNA structures would benefit from the added complexity.

To satisfy the specific needs of DNA nanotechnology researchers, a finer coarse-model was introduced in oxDNA (Ouldridge, Louis, and Doye, 2011; Šulc et al., 2012). It is a simulation code designed to model interactions of DNA and RNA

molecules at a coarse-grain level, losing some of the precision of all-atom models, but making computation much faster and enabling simulation of DNA kinetics that would otherwise be out of reach. To do so, seven different interactions have been modeled, namely:

- Backbone Connectivity,
- Watson-Crick Base Pairing (Hydrogen Bonds),
- Excluded Volume,
- Stacking Bonds,
- Coaxial Stacking,
- Diagonal Cross-stacking,
- Electrostatic Interactions (starting with oxDNA2 in Snodin et al., 2015).

Additionally, the model can use sequence-dependent parametrizations, allowing for finer simulations of hydrogen-bonding and stacking interactions. Due to the nature of the oxDNA model, different salt concentrations are simulated by changing parameters in the interactions, given that salt molecules are not explicitly modeled.

Finally, oxDNA can simulate structures using Metropolis Monte Carlo (and Virtual Move Monte Carlo), where nucleotides can only rotate and translate, or using Molecular Dynamics, allowing for thermal fluctuations and Brownian motion. As we will see, the latter is particularly useful in DNA origami where Brownian interactions can impact the shape and behavior of a larger structure around its equilibrium of minimum free energy. Again, due to the lack of solvent molecules, these interactions are modeled, not simulated explicitly.

To paint a more complete picture, it is worth talking about mrDNA (multiresolution DNA) (Maffeo and Aksimentiev, 2020), which starts to bridge the gap between the different simulation codes by progressively refining its models. It is primarily a coarse-grained model and it starts out considering the helices as elastic rods to obtain a first pass relaxation of the structure, before adding additional interactions and simulating each nucleotide. This results in significant gains in simulation costs, while still incorporating molecular dynamics. To enhance cross-compatibility, mrDNA files are compatible with oxDNA, meaning that it can be used to relax

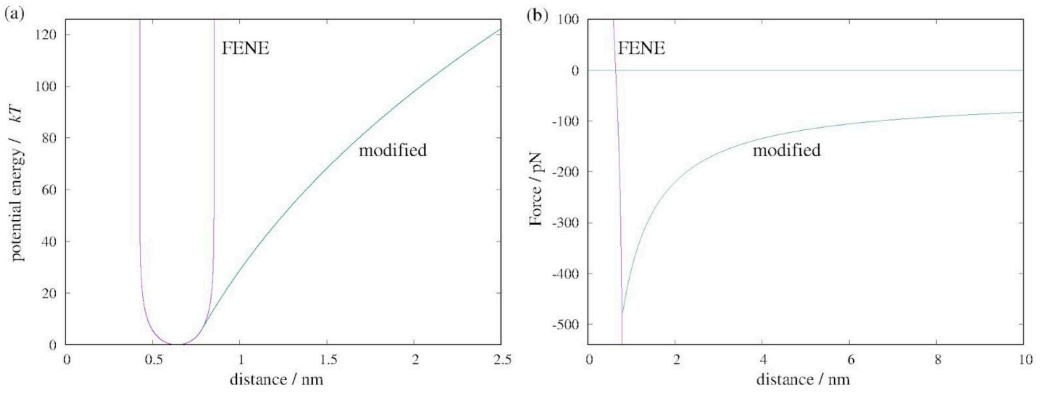

Figure 3.1: a) Original oxDNA FENE potential and modified relaxation potential; b) Forces due to these potentials. Reproduced with permission from Springer Nature from Doye et al., 2023.

structures before simulation, or to confirm results obtained from oxDNA simulations. Moreover, the suite of CAD tools written to design oxDNA molecules can be equivalently used for mrDNA.

3.2 Simulating DNA Origami with oxDNA

In oxDNA, simulations of large unrelaxed DNA structures, such as DNA origami, are run in three separate steps (Doye et al., 2023), where the first two are needed to relax the structure to a point where DNA bonds are within physical parameters and can be simulated correctly. The first step is a minimization step, meant to remove any overlapping nucleotides and some minimally overstretched bonds. It does not have any molecular dynamics interactions and most of the longer bonds are kept untouched. If we were to use the actual oxDNA interactions at this stage, we would immediately encounter numerical errors and singularities, since the potential used diverges for overstretched bonds, as shown in Figure 3.1a. The modified potential has a more gentle slope that allows far apart nucleotides to be brought back to physical distances, while still maintaining the same location for the minimum, i.e. converging towards the minimum free energy structure. It is fairly quick and it runs on CPU.

The second step is where the actual relaxation of the structure happens. This step is run with molecular dynamics enabled, albeit with a modified thermostat that sacrifices diffusion for faster energy gradient descent. Large scale movements are possible here and we expect the staple extensions on the origami to rearrange themselves to more natural positions. It is thus run on GPUs and it is comparable

to the actual simulation in terms of resources needed.

It is also important to mention that the oxDNA model has a few limitations specific to DNA origami. A detailed discussion is found in Doye et al., 2023, but we will mention that salt conditions are not modeled precisely enough to account for the difference between monovalent and divalent salts, which plays an important role in the transition of Holliday junctions from the open to the stacked state. Additionally, the twist of unconstrained junctions in oxDNA seems to be left-handed, where experimental data supports a right-handed twist. This is not expected to matter significantly in DNA origami, where most junctions are strongly constrained.

3.3 Initial Model Design

It is relatively trivial to write simple DNA structures in the format of input files for oxDNA. It requires two files, one that describes the topology and position of each nucleotide and one that defines the relationships between them: which nucleotides are connected by the same backbone. The first file will be updated or rewritten as the simulations progresses and the molecules rearrange, while the second one will be unmodified. Converting a DNA design to these instructions becomes obviously harder and more tedious as the structures grow larger, so that helper scripts have been written to automate the process. tacoxDNA (Suma et al., 2019) can convert a cadnano file into a format that can be read by oxDNA, maintaining spatial arrangement, bonds, and sequence. Since cadnano is meant only as a design aid and does not output simulated molecules, these structures can be quite unnatural and include severely overstretched bonds, forced twist, and other irregularities that are not corrected by tacoxDNA and require a relaxation stage.

The original model of our lilypad origami without any extensions is a fairly simple single-layer origami and it does not have any significantly overstretched bonds; thus the import in oxDNA is relatively painless, as shown in Figure 3.2.

As we wish to simulate the structure and behavior of our lilypad sensor, we need to first introduce the methylene blue curtain, by adding seventy staple extensions and the complementary strand that would be modified with methylene blue. oxDNA can only model nucleic acids, so our strands will not have any actual modifications, but the mere presence of overhangs could be enough to affect the DNA structure, so their effect is still of great interest. As shown in Figure 3.3, we can create staple overhangs in cadnano, with the caveat that in our design they are not planar to the DNA origami, but they project outwards on a different plane. In cadnano we first

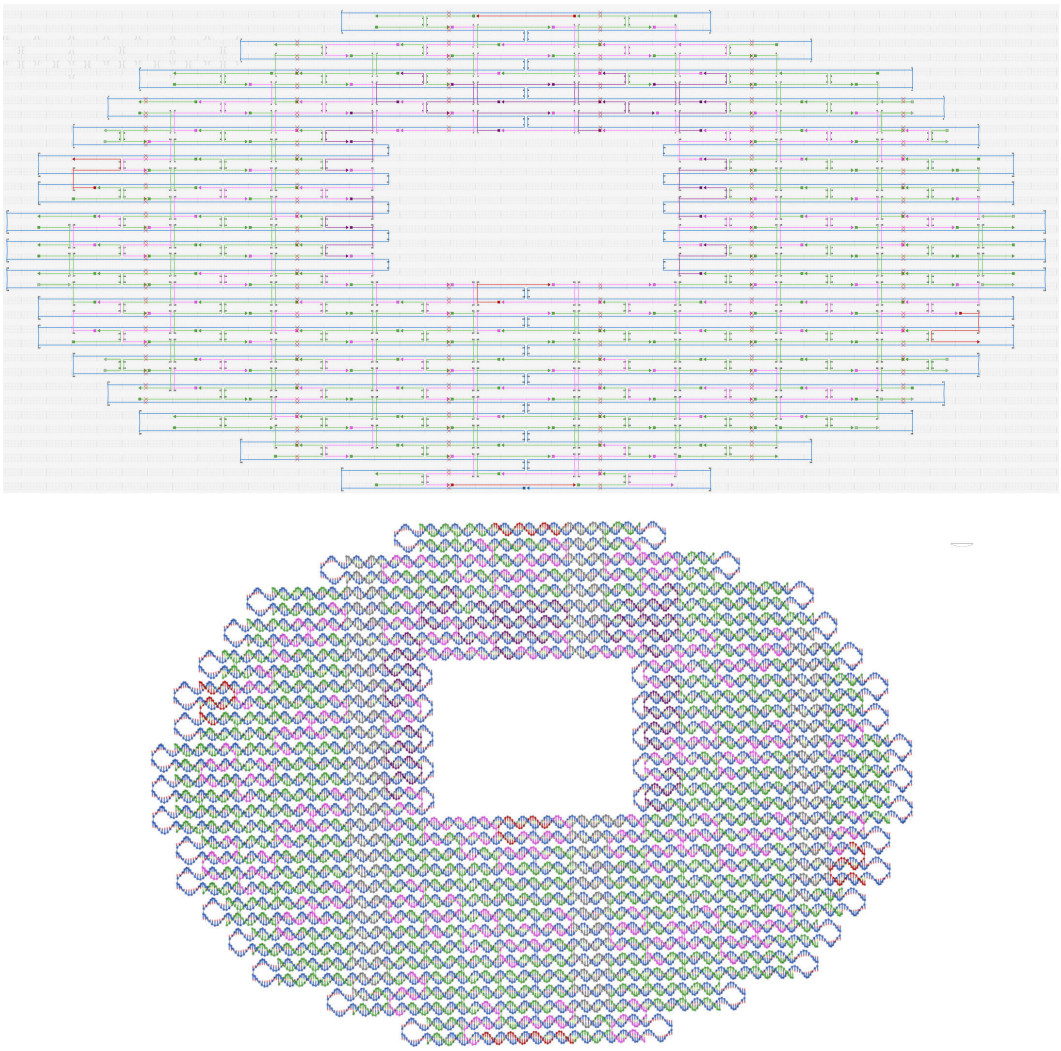

Figure 3.2: Top: Lilypad origami as designed in Cadnano 2. Bottom: Lilypad origami imported in oxView (Poppleton et al., 2020) through tacoxDNA.

need to introduce a second layer of helices where the extensions lay. In this model, they will still be on a plane parallel to the DNA origami, and they will relax in the outward orientation during simulation. This will entail additional simulation cycles before the system reaches equilibrium.

Finally, we decided to forego the single staple extension that is used as the analyte binder and the long double-stranded linker that tethers the origami to the surface, as we suspected they would not have large structural effects.

After importing the design in oxDNA, we ran a minimization step, which is relatively quick, a few minutes, and then started the relaxation phase. However, while the model showed a converging and relatively constant free energy, the structure quickly

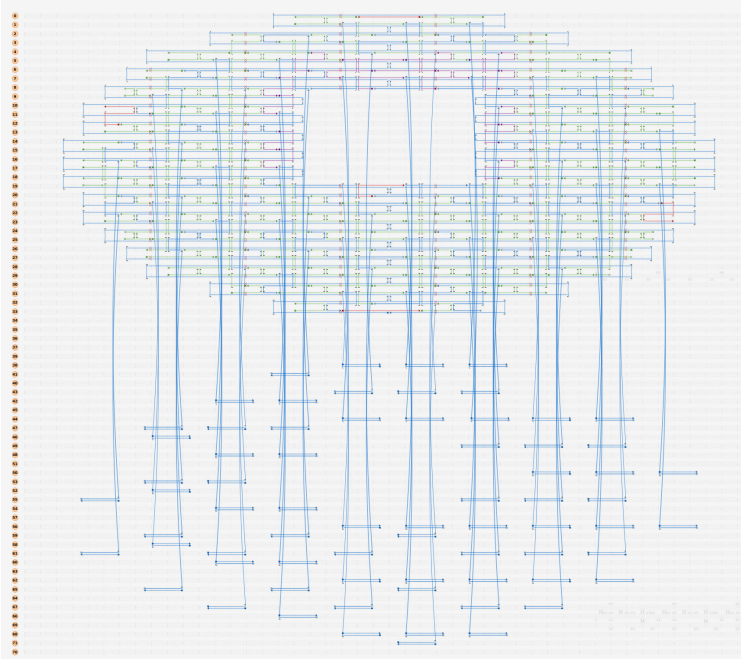

Figure 3.3: Lilypad origami with methylene blue curtain added on a separate plane in cadnano 2.

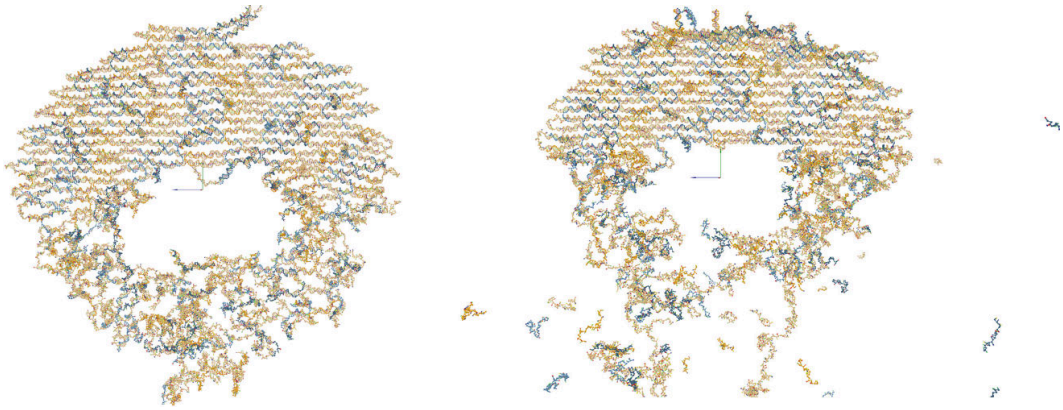

Figure 3.4: Lilypad origami with methylene blue curtain undergoing relaxation in oxDNA, the two frames show the evolution over time. Visualized in oxView.

exploded, with the origami unraveling and staples falling off, as shown in Figure 3.4. This might be due to the way bonds are relaxed, some of them possibly having to thread through the origami in order to relax, and to the fact that the modified potential used in relaxation has limited capabilities and might not be best suited for this specific design.

In order to redesign the structure so that it would need minimal relaxation, we turned to tools that can directly modify oxDNA topologies, specifically oxView

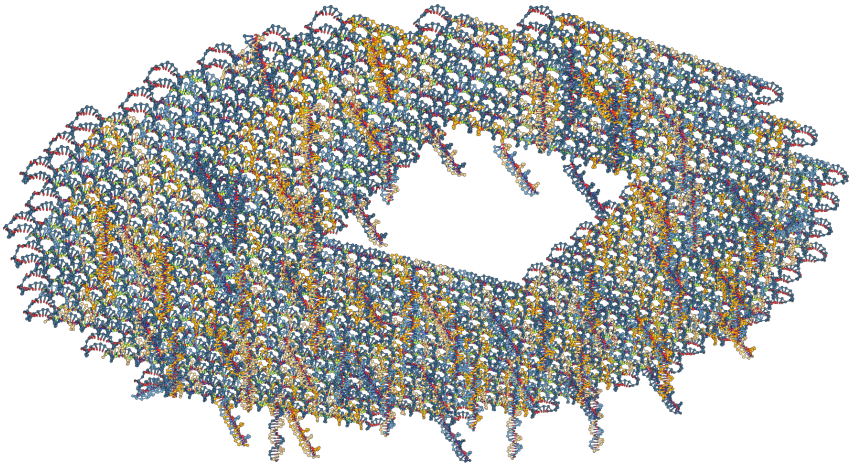

Figure 3.5: Lilypad origami with methylene blue curtain added through oxView scripting. Visualized in oxView.

(Bohlin et al., 2022; Poppleton et al., 2020). On top of the integrated visual editing capabilities, an API allows the user to access advanced functions and automate them through Javascript. We then wrote code[1] to add the staple extensions oriented directly outwards, resulting in the structure shown in Figure 3.5.

3.4 Effects of Overhangs on DNA Origami

After the relaxation phase and during the simulation, the lilypad origami with seventy methylene blue extensions looked noticeably curled along the axis of the helices, as shown in Figure 3.6. In trying to devise a metric to measure this curvature, we analyzed the angle between helices, but found that the nature of the molecular dynamics simulations leads to large swings from time point to time point. While it does not capture the effect precisely, we decided to use the distance between the first and last helix, which should be ~80 nm on a flat origami.

We then tested a few more versions of this same origami, with varying numbers of modified staples, from 0 to 234, meaning every staple on the origami. We noticed that origami with no modifications or only 30 overhangs do not seem to show this effect, but a higher number of modifications leads to exaggerated effects with a degree of curvature that can make the origami completely wrap around itself. We verified this behavior over 30 µs of simulation time[2] with the unmodified oxDNA potential for all structures, as shown in Figure 3.7. We concurrently verified that the energy converged and was flat throughout the whole simulation.

[1] A special thank you to Petr Šulc for the precious help.

[2] Such a simulation is run with CUDA on an Nvidia 1070 Ti in approximately three hours.

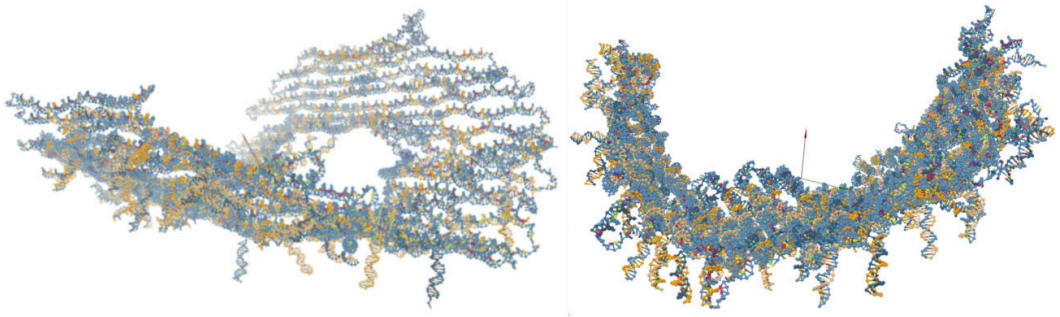

Figure 3.6: Two views of a DNA origami labeled with 70 x 20 bp double-stranded staple extensions during simulation in oxDNA, exhibiting significant curling. Visualized in oxView.

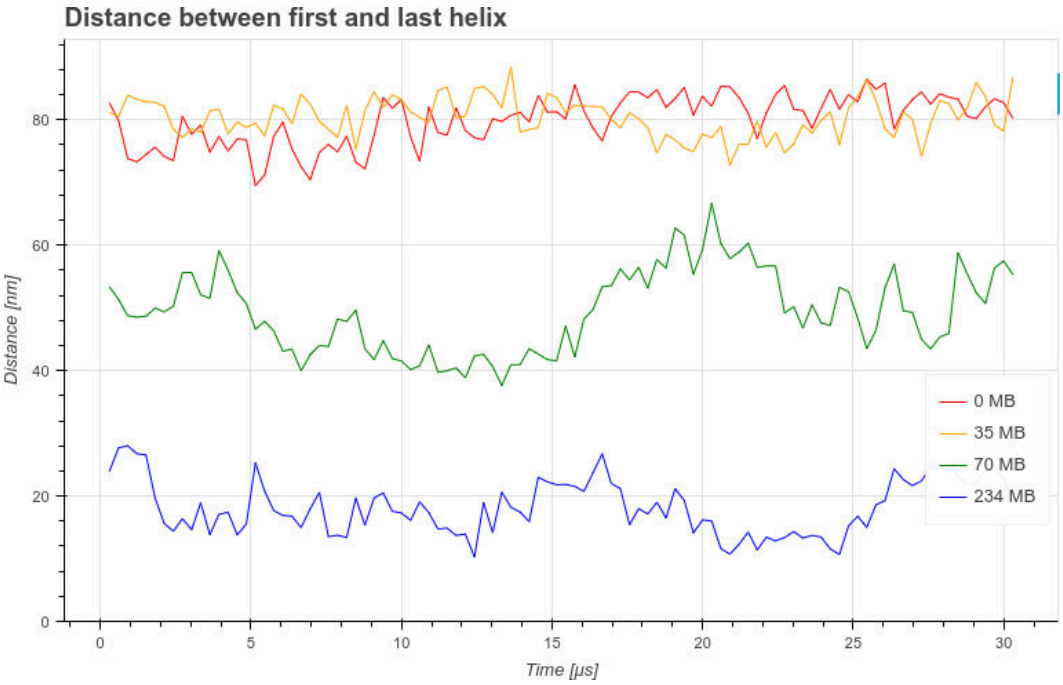

Figure 3.7: Distance between first and last helix of DNA origami with different numbers of staple extensions in their methylene blue curtain. All structures were minimized, relaxed, and then simulated using oxDNA.

We then tested a few different hypotheses to establish the cause of the curvature. We first considered that our staple extensions are 20 nt long and they are entirely double-stranded, leaving little to no room for flexibility between the origami and the extension. We thus made the complementary methylene blue strand one nucleotide shorter in the simulation, leaving one unpaired nucleotide free to rearrange, but this led to no discernible difference in simulation. We also considered shorter curtains (10 bp instead of 20 bp), we added flexibility inside the origami, and we tried changing salt conditions to mask electrostatic interactions, but we never saw any significant improvements.

In order to collect more data, we increased the simulation time for all structures ten-fold to 300 µs, with the results shown in Figure 3.8. This resulted in the 0, 35, and 70 staple extensions curves looking much more alike as the simulation progresses, with the 70 condition flattening out at times, while the 0 and 35 looked more curled. We did not observe any significant change in free energy, suggesting that this phenomenon is not due to further relaxation and convergence of the structures to a minimum free energy configuration. These states seem to be within the thermal fluctuations of our experimental conditions. Significantly, we did not see this curling effect in other simulations run with CanDO, mrDNA, and the unreleased cadnano Toolkit, although none of these models incorporates molecular dynamics.

At this point, we decided to pause these experiments, as we could not understand whether we were seeing an artifact of the relaxation step, or something with a physical meaning.

3.5 Effect of Overhangs on Rigid Double-Layer Structures

Sidestepping for a second the physical cause of these observations, we focused on possible solutions and looked into stiffer DNA origami designs. Single layer DNA origami are known to be fairly flexible, due to the fact that helices can slide against each other, as the junction angle is not strongly fixed. This issue might have been historically initially overlooked as most of the experimental measurements were done with atomic force microscopy on mica, where DNA structures are completely flattened due to the strong electrostatic interaction.

We thus looked at multi-layer DNA origami, borrowing the double-layer tile design from the Qian Lab at Caltech (Thubagere et al., 2017). In this design, two sets of helices are stacked on two layers in orthogonal orientations, meaning that the axis of flexibility of each layer is compensated by the other layer. We imported the

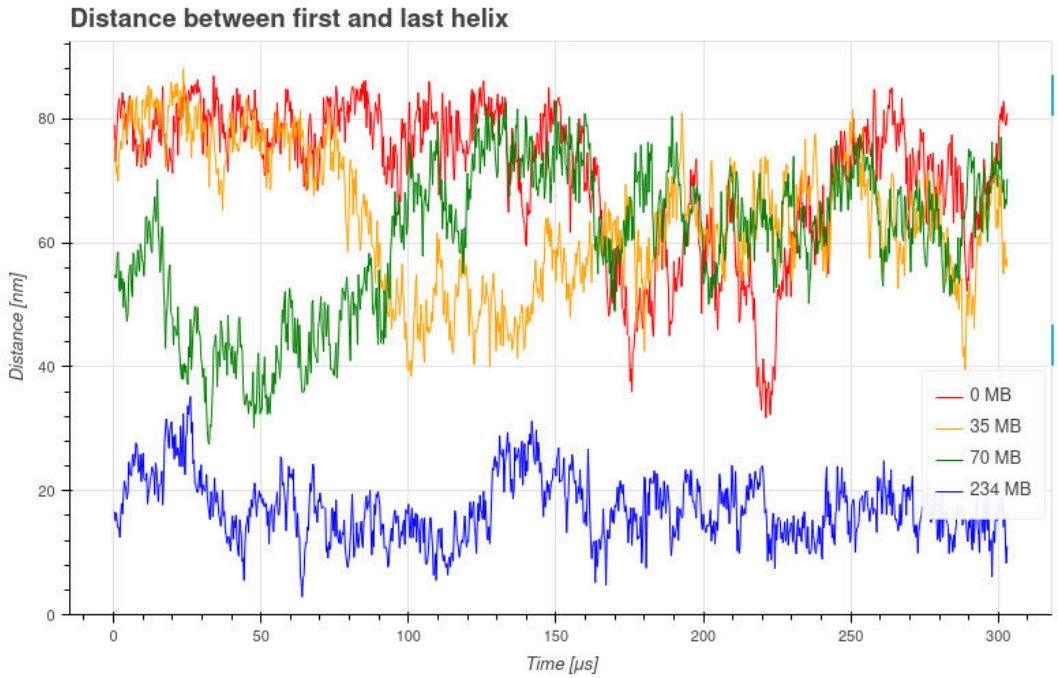

Figure 3.8: Simulation over a longer time span of the distance between first and last helix of DNA origami with different numbers of staple extensions in their methylene blue curtain. All structures were minimized, relaxed, and then simulated using oxDNA.

design in oxView and added the same staple extensions we use for the methylene blue curtain: 20 nt with a complementary strand. We designed three conditions with 0, 55, and 95 overhangs; we could not add any more as the double layer origami has fewer staples that can be extended on each side (half of the scaffold is used for each layer). The double layer tile is designed with significantly overstretched bonds in cadnano and it requires multiple stages of relaxation before it can be simulated with oxDNA. Specifically, the design is complex enough that the relaxation step we employed earlier fails as the bonds get tangled. We used a rigid-body relaxation function implemented directly in oxView that can recognize separate clusters, the two layers, and move them as separate objects trying to minimize their bond length. We then followed the previous pipeline to minimize, relax, and simulate the three structures. The results of a 300 μs simulation are shown in Figure 3.9, highlighting how the double layer origami remains stiff no matter how many staple extensions are added.

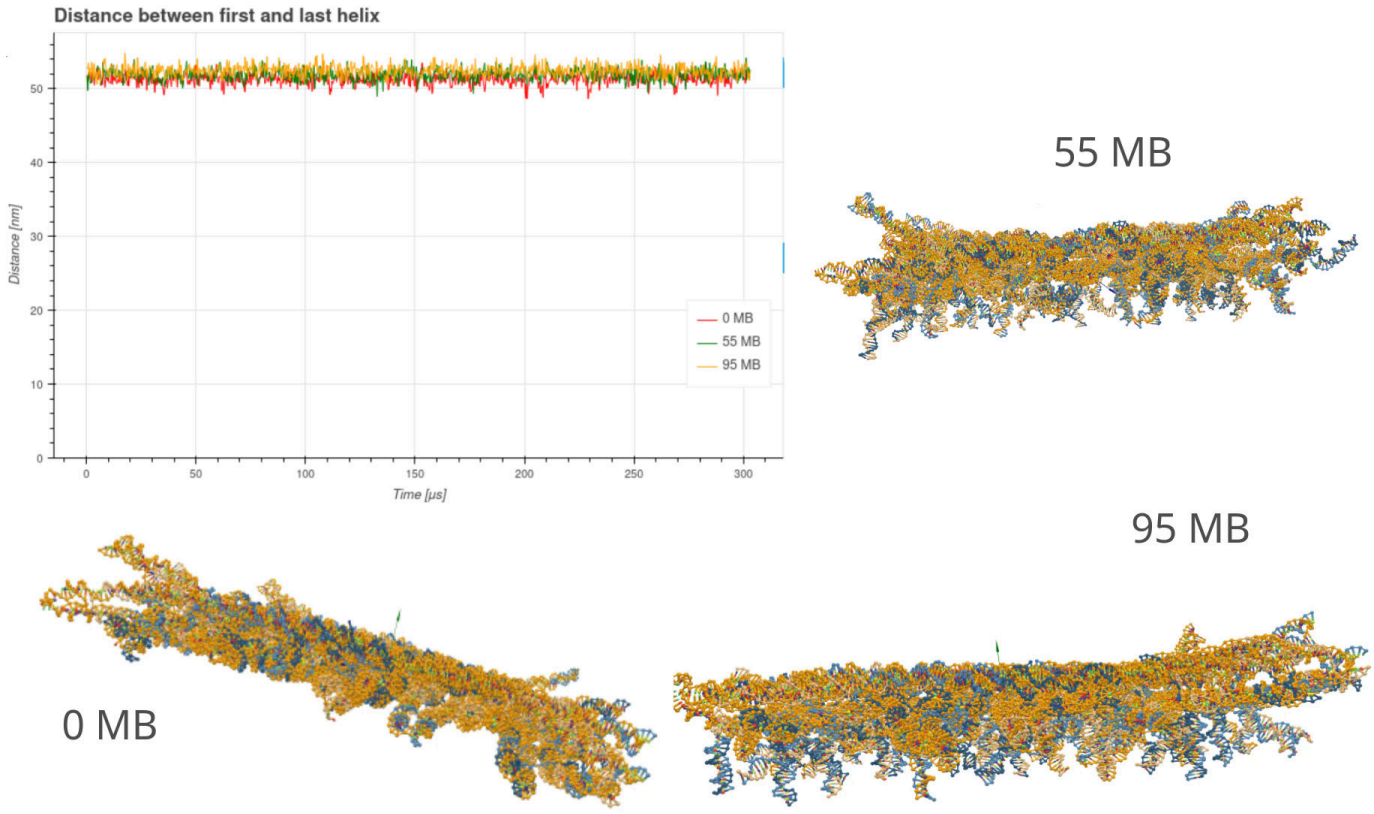

Figure 3.9: Distance between first and last helix of a double-layer DNA origami with different numbers of staples extended, simulated over 300 μs, showing no curling of the structure. Representative frames of the three different structures during simulations, visualized in oxView.

3.6 Explaining the Curling of the Hairygami

The frustrating part of research is having to abandon promising ideas after hitting one too many walls. Luckily, Petr Šulc and his group came to the rescue here. This section is meant to shed some light on the mystery of the curling DNA origami, with most of the explanation coming from Sample et al., 2024, a work by the Šulc lab that was being written as we were running our experiments and that investigates the same issue.

The curling effect we were seeing indeed had physical meaning, but it is non trivial to see it in simulation. Both the curved and the flat states have relatively close free energies, and this explains why the energy profile looked flat and the system seemed to be in equilibrium, when looking at the free energy. Fluctuations in thermal energy in molecular dynamics simulations are sufficient to move the system between the different states and hide the true minimum free energy configuration.

Umbrella sampling is a simulation technique that can be used to study such systems, by choosing a parameter of the structure and fixing it to a predefined value for the entire duration of the simulation. The experiment is then repeated sweeping through different values of the chosen parameter and the average free energy can be plotted, determining which value yields the minimum free energy. Sample et al., 2024 chose a single layer origami with 85-169 overhangs (a "hairygami") and studied its curvature by fixing the distance between first and last helix as the umbrella sampling parameter. This showed that, as the number of overhangs and their lengths increased, so did the curvature of the DNA origami, and its minimum free energy moved in that direction, matching the initial results of our simulations. We posit that our results were most evident at the end of the relaxation phase because it uses a different thermostat from the one used in the actual simulation. As we mentioned earlier, this thermostat (Bussi, Donadio, and Parrinello, 2007) favors minimizing the free energy of the structure, with a lower weight on diffusion and thermal fluctuations.

They then proceeded to selectively disable interactions in the oxDNA model to study what was causing the curling. They found that the effect was due to the flexibility of the overhangs, which can thermally move around their fixed point and bounce against other parts of the origami. The curling is not mostly caused by overhangs bumping against one another, but more by overhangs bumping against the origami itself and trying to entropically maximize the volume they can access. In the curved state, the overhangs maximize the number of states they can explore.

3.7 Consequences and Experimental Evidence

The issue of DNA origami curling under bouncing staple extensions might have significant consequences on the performance of our sensor that go beyond the change in shape. Methylene blue molecules give rise to a current signal when they are close to the surface via electron tunneling, the transfer of electrons between reporter and electrode through the solution that divides them. The electron transfer rate of this phenomenon has a negative exponential dependence on the distance between the two, meaning that small variations of the distance between methylene blue and surface can greatly affect the measured current. Molecules that are far enough from the gold electrode might not contribute to the signal, worsening the single molecule signal gain that we achieved by labeling the DNA origami with 70 MB molecules. The conformations shown in simulation seem to be closest to the surface in the center, where the binder would lock the origami on the electrode, and progressively curl upwards towards the edges, potentially leaving several MB

molecules inactive. It is hard to precisely estimate this effect quantitatively, but we empirically aim to design our systems such that MB is no further than 1 nm from the electrode, or approximately 3 bp. Uzawa et al., 2010 attached a single methylene blue on a single-stranded DNA tether and found that the electron transfer rate is approximately 2000 times worse between a 3 nt tether and a 30 nt tether. Single-stranded DNA is however very flexible and these conditions should not be viewed as increasing the distance by ten times. Unfortunately, when the same authors tried to repeat the experiments with much stiffer double-stranded DNA, they found that the electron transfer rate was too slow to measure with their setup. This suggests that even a 3 bp (1 nm) distance has highly significant effects on electron tunneling.

We set out to obtain some preliminary experimental evidence of these effects by folding two different versions of our lilypad sensor, one with 35 MB, which is predicted to be generally flat, and one with 70 MB, the one we used throughout our experiments and the same one oxDNA predicted to curl. We used a 20 bp long MB curtain and interrogated the sensor using our standard 28 nt DNA analyte[3] at a concentration of 2 nM. The results of this experiment are shown in Figure 3.10 and they highlight that the behavior in the two conditions is extremely similar, suggesting that we are not fully capturing the signal gain from the additional methylene blue molecules. This first experiment supports the results we have seen in simulation, but there are other possible explanations to this phenomenon. The surface might be too crowded and the lilypads might not fall flat, they might have additional deformations due to the MB itself (suffice to think of the aggregation issues mentioned in Sections 2.2 and 2.4), or there might be a combination of different effects. Finally, as we mentioned before, the different conformations are still close enough in free energy that thermal fluctuations might be enough to deform the DNA origami and hide some of these effects.

Finally, thanks to Lulu Qian and Namita Sarraf, we managed to test a version of our sensor using the double-layer origami and a 55 MB curtain. We designed new staples with 20 nt extensions complementary to our MB strand, a new staple for the analyte binder, and we synthesized a 957 bp double-stranded linker to tether the origami to the surface. The response of the sensor after interrogation with 2 nM of the same 28 nt DNA analyte is shown in Figure 3.11. We saw a much more gradual rise in current and an on signal that is about half of what we measured

[3] While this analyte has a mismatched length of 28 bp compared to the 20 bp of the MB curtain, we expect a single double-stranded DNA analyte to be flexible enough for the origami to get close to the surface.

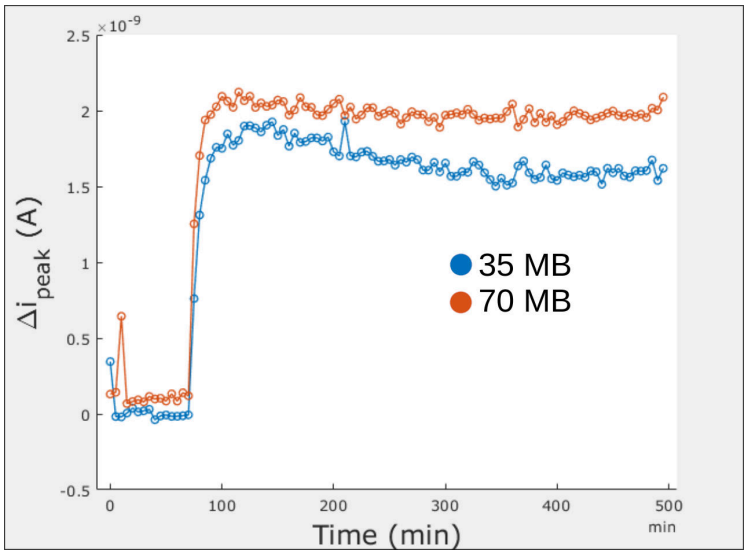

Figure 3.10: Experimental interrogation of two lilypad sensor designs, one with a MB curtain with 35 staple extensions and one with 70. Addition of 2 nM of a DNA analyte shows similar response for the two conditions.

with the original lilypad. This could potentially be the other side of the coin where the stiffness of the double-layer origami is such that it hardly adapts to the surface and even the small difference in length between analyte and MB curtain can have an adverse effect. A less flexible origami might also take longer to find the binder on the surface, as it can explore fewer states, explaining the relatively long rise in signal. While we did not explore this any further, it would be interesting to fold new versions of this origami with different number of methylene blue molecules and see if it demonstrate a more linear increase in signal with increased labeling. Finer tuning of this structure might yield a sensor that matches and possibly improves on the results shown in our work with the single-layer disc.

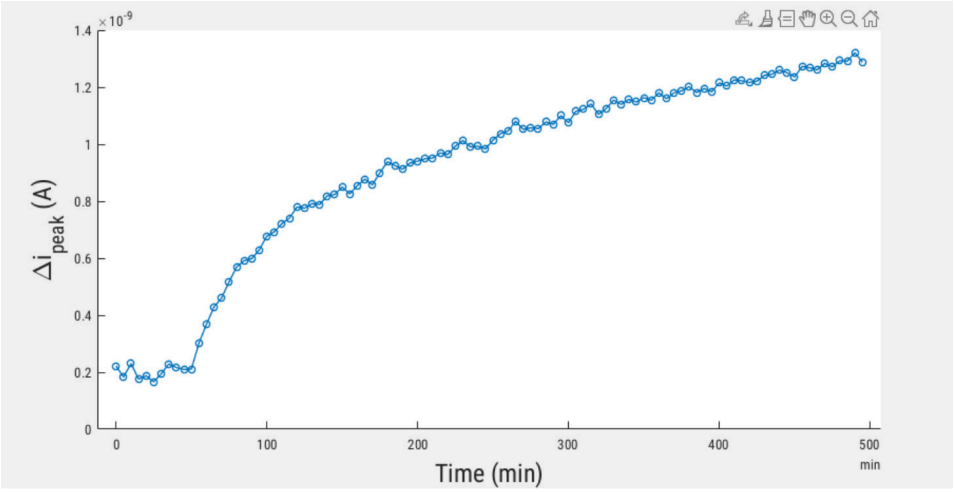

Figure 3.11: Experimental interrogation of a lilypad sensor designed using a double-layer origami instead of the flexible single-layer disc. The origami is modified with 55 methylene blue molecules. Addition of 2 nM of DNA analyte shows a fairly slow response compared to the original design.

Chapter 4

EXPANDING THE CAPABILITIES OF DNA NANOTUBE GLIDERS

4.1 Introduction

Ibusuki et al., 2022 demonstrated an engineered motor protein that can bind and kick DNA. The authors replaced the tubulin-binding domain of dynein (the foot) with a few different DNA binder proteins, incorporating their respective motor binding sequences (MBS) on DAE DNA nanotubes and showing that they glide similarly to microtubules. The higher programmability of DNA nanotubes enables new behaviors in motor-filament systems. For example, by using two different DNA binder proteins on the motors, they demonstrate sorter and integrator machinery, separating or combining different populations of DNA origami. Additionally, DNA nanotubes can be designed in many different topologies, as described in Section 1.2, yielding gliders with different properties, both structurally and kinetically.

Their work demonstrates different DNA-binding feet, taken from proteins that have been shown to have binding activity to DNA. Many of these proteins recognize palindromic DNA sequences, but we will instead focus on LEF1 which recognizes a 9 basepair DNA sequence that is non palindromic (5'-CTTTCGAAG-3'). This means that LEF1 can recognize the orientation of the sequence and the kick of the re-engineered dynein is only in one direction. For a palindromic sequence, the kick could be in either direction, as no orientation is preferred. While this has not been studied in depth, it is also clear that the main component of the vector of the kick is aligned with the position of the motor binding sequence (MBS).

Our interest in this work stems from the possibility to engineer DNA structures to a degree that is not possible for microtubules (Lian and Lin, 2024). Previous works in microtubules engineering have focused on general population parameters, such as controlling their length (Jeune-Smith and Hess, 2010), stabilizing them (Chew and Cross, 2023), or disassembling them (Bobinnec et al., 1998). More targeted control can be achieved by adding light-controlled switches (Buck and Zheng, 2002) and more recently some genetic modifications have been shown incorporating either chemically reactive domains or light-sensitive domains (Liu, Chen, et al., 2022). Not only have DNA nanotubes been designed with different architectures, they have also

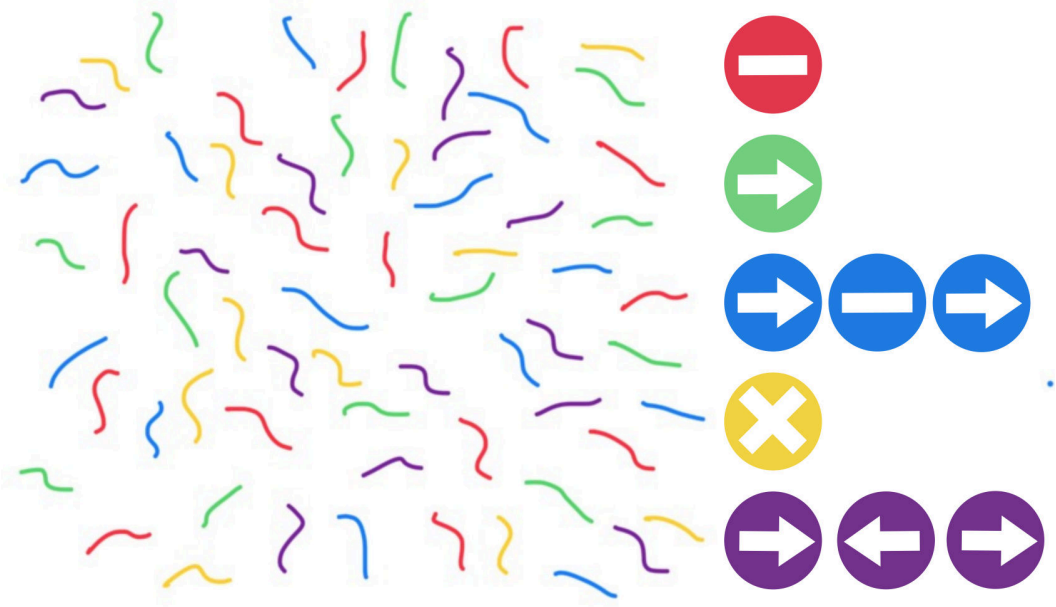

Figure 4.1: Different and orthogonal populations of DNA nanotubes gliders that exhibit independent behaviors and can switch between different states through external control.

been modified using the broader toolkit of DNA nanotechnology, from growing them from DNA origami seeds (Mohammed and Schulman, 2013; Mohammed, Šulc, et al., 2017), to integrating DNA strand displacement machinery (Zhang, Hariadi, et al., 2013), and controlling assembly with enzymes (Agarwal and Franco, 2019). Even before considering macro-modifications like the aforementioned ones, the sequence programmability of DNA nanotubes allows the designer to precisely position motor binding sequences and tune their properties, for example by choosing their density and spacing or their twist along the DNA helix, or possibly even tweaking their binding properties by adding sequence mismatches.

We envision a system of independent DNA gliders populations that exhibit different behaviors or can be controlled externally orthogonally. Figure 4.1 shows the kinds of machinery that we explore in this work. Red colored gliders are halted and cannot glide, even in the presence of ATP, while green gliders have received an "on signal" and are now gliding freely. Blue gliders cycle between on/off states through external control, while yellow gliders can be detached from the motor surface and released back in solution. Finally, purple gliders can switch direction of gliding along their axis, again through external control.

4.2 Launch Control

We first envisioned a system to selectively control the gliding of different populations of DNA nanotubes by selectively starting and stopping them through DNA strand displacement. This is a behavior that could be potentially achieved in microtubules systems through other means, for example by using a buffer without ATP, which would prevent any motor activity. Cycling buffers with and without ATP would turn gliding on and off. We aim to show a system that does not rely on the absence of ATP to stop gliding, meaning that it could be used in a more complex environment, where ATP cannot be controlled either because of experimental limitations or because it is needed by other components.

To do so, we designed a DNA anchor complex that can bind to the streptavidin coated glass slide through a biotin modification. As shown in Figure 4.2, the DAE DNA nanotubes are modified by extending the RE3 strand on the REd tile with an overhang that is complementary to a domain on the anchor complex. The anchor complexes will bind to the overhang on the nanotubes and, if the bond is strong enough, the nanotubes will be held in place on the surface, regardless of any kick from the motors. The overhang is designed with a toehold domain that can be used to displace the tubes from the anchor complexes, freeing the nanotubes from the anchors and allowing for gliding.

The surface is prepared by mixing biotinylated anchors and motor proteins on the streptavidin coated slides before adding the DNA nanotubes modified with overhangs. We add the ATP buffer and image the sample for a few minutes to verify that the DNA nanotubes are anchored. We then wash the sample with ATP buffer supplemented with the invader strand and image it again. In all launch control experiments we have a second control population of orthogonal tubes (more on that in Section 4.2) that do not have any launch control overhangs and can be used to verify surface preparation and gliding. Figure 4.3 shows an example of a gliding experiments, with launch control nanotubes appearing to be solidly anchored before addition of the invader strand and then gliding convincingly once they have been displaced. The control population of unmodified nanotubes is shown to be gliding in both states.

Tuning the Surface

Several parameters have to be adjusted to obtain a design where DNA nanotubes are stuck on the anchors in the off state and are gliding without issue in the on

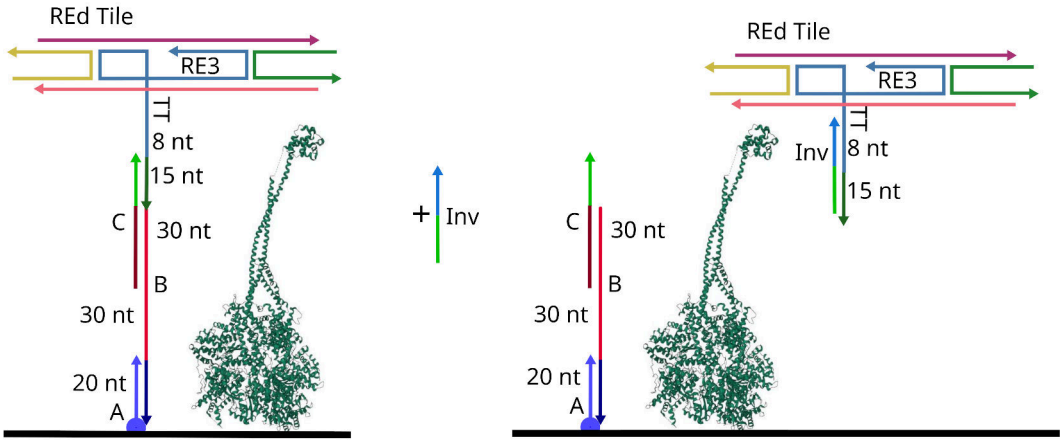

Figure 4.2: Scheme of a mechanism to control gliding of DNA nanotubes by using DNA anchors. The anchor complex is formed by a biotinylated strand A that binds to the streptavidin coating on the surface, by a strand B that acts as a flexible bridge, and by a strand C that binds to an overhang on the RE3 strand of the DNA nanotube. The addition of an invader strand (Inv) releases the DNA nanotubes from the anchors, through an 8 nt toehold on the extended RE3 strands. Invaded nanotubes can then glide on the motor proteins. Dynein image PDB 4RH7 from Schmidt et al., 2015.

state. The surface itself is a mixture of motors and DNA strands, which creates a trade-off between having enough anchors to hold the tubes, and at the same time enough motors to obtain robust gliding. The anchoring of the DNA nanotubes is determined both by the density of anchor strands and by the density of overhangs on the nanotubes, but, if the binding is too strong, it might be hard to displace entirely given that the kinetics of DNA strand displacement depend on concentration, diffusion and accessibility of the complex to be displaced. We do not know what would happen if the release of a nanotube from the anchor complexes was not complete and the nanotube started gliding while still being held in place in one location. The kick of the motors might be strong enough to release the anchor that is stuck, or it might cause the tube to break, or possibly it might be too weak to have any visible effect.

The overhang on the DNA nanotube is designed by modifying strand RE3. We initially engineered it simply by extending RE3 on the 3' end, but we then realized that that the orientation of the helix in that position is such that the overhang would project on the inside of the tube, making it hard to reach for the anchor strands and possibly constituting an additional steric obstacle for tube formation. Notably, before it was corrected, this original design proved to work fairly robustly and we only modified it to optimize the system, not because of any experimental issues. In

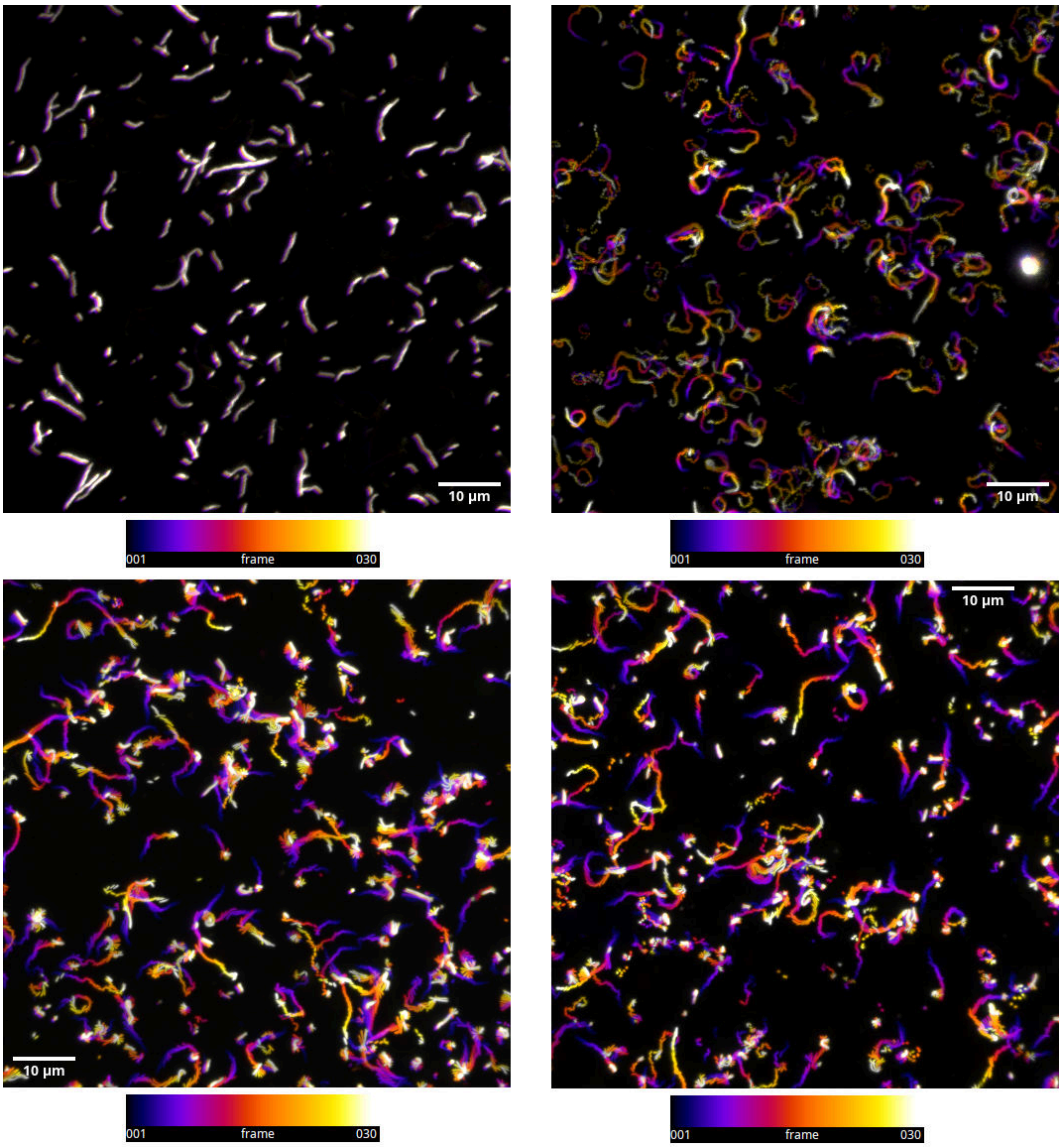

Figure 4.3: Top Temporal-color coded images of gliding assays of launch control DAE nanotubes before and after adding the invader strand. On the left, the only movement is the drift of the stage, while gliding is clear on the right. Bottom From the same field of view, a different population of DNA nanotubes that do not have launch control machinery, before and after addition of the invader strand. 30 frames imaged at 20 s intervals.

order to have the overhang project on the outside of the nanotube, we rotated the strand and moved the nick to a different position, before extending it. The extension is designed with two thymines that provide some flexibility, followed by an 8 nt toehold and a 15 nt binding domain complementary to a conjugate region of the anchor complex.

Since the part of the sequence of the new RE3 that is within the tube has not been modified, when we anneal the tube we can titrate the concentration of extended RE3 and original RE3 to obtain different levels of doping of the DNA nanotube. This lets us control the density of overhangs on the tubes, and we think of this is as a variable that is almost equivalent to the density of anchor strands on the surface. While the effects of the two are more complex, increasing the doping of tubes allows for lower anchor density, which in turn results in a surface coated with more motors.

Figure 4.4 shows how the percentage of extended RE3 over total RE3 in the annealing solution affects the capture and release of the DNA nanotubes. The 0% condition is useful to assess the quality of the modified surface and whether the anchor strands hinder gliding. The trend of higher capture with increasing doping is fairly clear, however all conditions from 5% and higher seem to yield good capture and release. We decided to only consider 5% and 10% for further testing, both because we do not need the DNA nanotubes to be anchored more strongly than the bare minimum necessary to hold them in place, and because we noticed that at higher doping conditions the release seems to affect the tubes, which are either found broken or gliding less consistently, for example if they remain anchored in one spot.

Figure 4.5 shows the effect of the density of anchor strands for the two doping conditions of 5% and 10%. We anneal the anchor complex at a concentration of 10 µM and then dilute it to 125 nM, 250 nM, and 500 nM before mixing it at a 1:2 ratio with the motor proteins. The solution is then flowed onto the biotinylated slide and incubated for five minutes. While we cannot precisely control the density of the surface, which is not just determined by concentration, but also by diffusion, we can see an effect of the initial concentration of anchors on gliding. While the 10% nanotubes seem to show robust on/off switching for every condition we tested, the 5% show a progressively worse off state as we decrease the number of anchors. We decided to focus on tubes with 10% doping and keeping anchor strands at 250 nM.

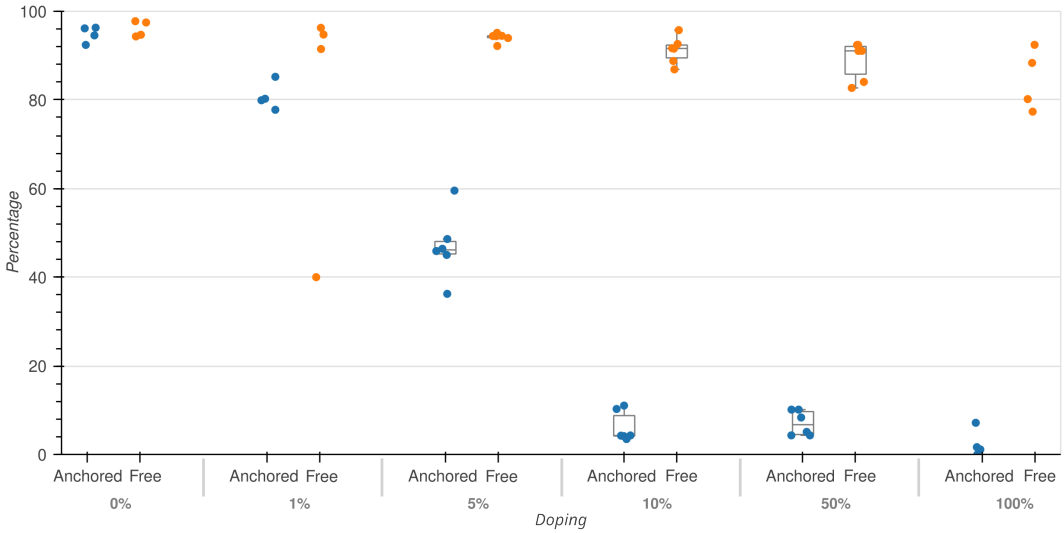

Figure 4.4: Effect of overhang doping on the on and off state of the anchor system. Nanotubes are annealed with a mix of unmodified RE3 and extended RE3, shown as a percentage on the horizontal axis. The free state is obtained by flowing in an ATP buffer supplemented with the invader strand. The percentage of nanotubes that move more than 1 µm over the entire measuring window is shown as on the vertical axis for the anchored and released states. For the 0%, 1%, 5%, and 100% conditions, two fields of view on two different slides are imaged and measured, for the 10% and 50% conditions, three slides are imaged.

Tuning the Anchors

As shown in Figure 4.2, we designed the surface anchors to be a DNA complex formed by three strands: a biotinylated strand A that binds to the streptavidin coating on the surface, a connecting strand B, and a strand C that binds to the overhang on the nanotubes. The rationale behind this design is to make the strands modular and replaceable without incurring in high synthesis costs. Using a single strand would require every iteration to have a biotin modification on one side and be PAGE purified so that there is no truncation on the other end where the nanotube is attached. Knowing that commercial chemical synthesis of oligonucleotides starts at the 3' end and truncations only happen on the 5' end, we designed strand C to bind the nanotubes on the 3' end in order to avoid truncations on that side, making sure that the anchors would hold the nanotubes in place. The length of the complex was chosen such that, when perpendicular to the surface, it would be as tall as the dynein motors, thus being able to reach the DNA nanotubes gliding above them on the motor surface.

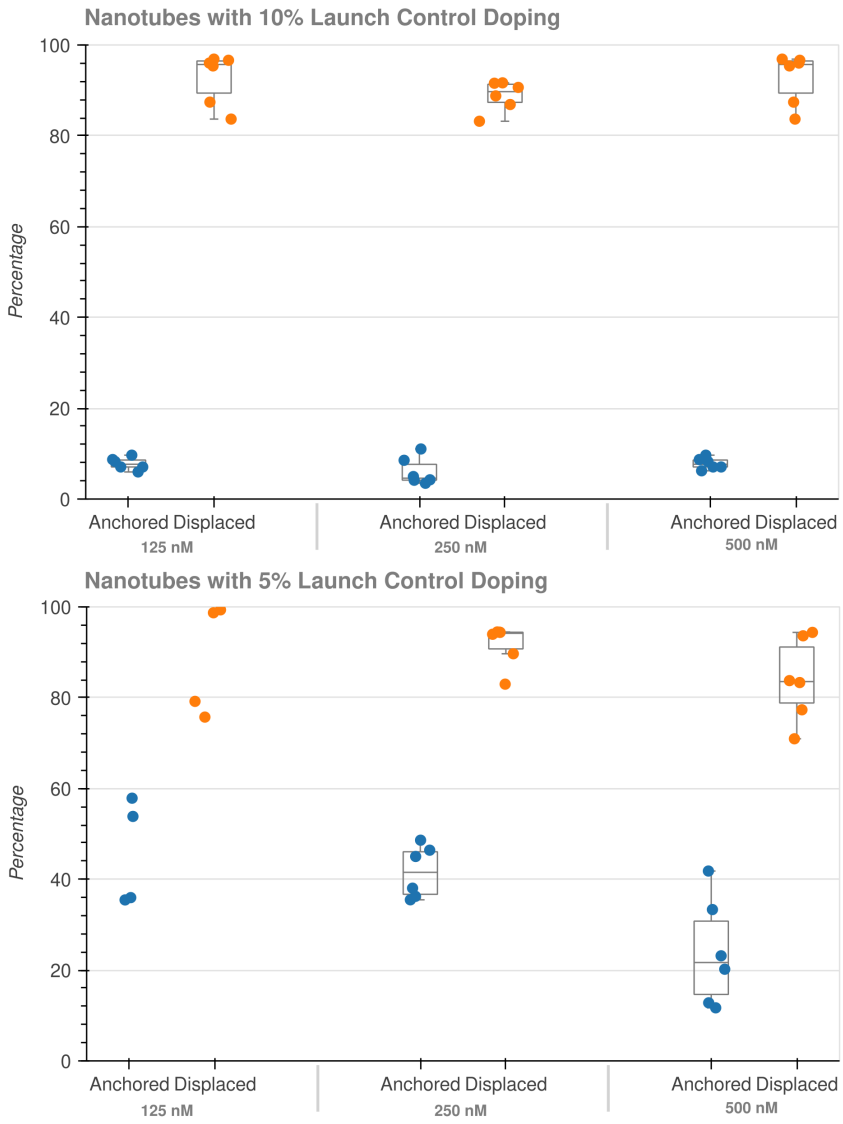

Figure 4.5: Effect of concentration of anchors on the on and off state of the anchor system. Top: Nanotubes doped with 10% of extended RE3 shown under three different conditions. The anchor complex is annealed and then diluted to 125 nM, 250 nM, and 500 nM before mixing it with motor proteins and adding it to the slide. Bottom: Nanotubes with 5% of extended RE3 shown under the same three surface conditions. The percentage of nanotubes that move more than 1 µm over the entire measuring window is shown on the vertical axis for the anchored and released states. Aside from the 5% 125 nM condition, where only two slides are imaged, for every other condition, two fields of view on three different slides are imaged and measured.

We first tested how the strength of the binding between anchors and nanotubes affects immobilization. In the off state, when the DNA nanotubes are stuck bound to the anchors, the motors are still hydrolyzing ATP and likely kicking them. If the binding domain on the C strand is not long enough to securely anchor the nanotubes, we expect to see gliding in the off state. We ordered four versions of strand C with binding regions 0 nt, 5 nt, 10 nt, and 15 nt long and we ran gliding assays with all of them, as shown in Figure 4.6. We noticed that 15 nt seems to offer the highest contrast between the two states, with the 10 nt condition being quite similar, albeit with a less perfect release. This condition can be thought of as extending the toehold for strand displacement by 5 nt, so we would not expect to see any differences in the on state. It is possible that we are just seeing sample-to-sample variability, and more data would be needed to assess that. Interestingly, the 0 nt condition still shows some degree of anchoring, possibly suggesting that DNA nanotubes with a single-stranded overhang are still stickier than invaded nanotubes where the overhang is double-stranded. While we designed the anchor complex to minimize crosstalk between strands, it is possible that there is some minimal interaction between the single-stranded domain on B and the overhang on RE3. We have often observed that even small affinities between strands can cause strong interactions when the tiles are repeated as often and closely as they are on nanotubes.

We designed a shorter version of strand B, by removing 10 and 20 nt from the single-stranded domain between A and B, in order to assess whether the complex could still bind to the nanotubes if it was significantly shorter (~4-8 nm) than the leg of the motor proteins. As evidenced in Figure 4.7 we saw that a shorter B does not apparently impact the capture capability of the complex. This might be explained if the re-engineered dynein motors behave like springs and are not found in their fully extended conformation, as evidenced for kinesin in previous models and experiments (Gibbons et al., 2001; Kerssemakers et al., 2006; VanDelinder, Imam, and Bachand, 2019). Similarly to how we think of the motor proteins as elastic springs, we should not look at the anchor complex as a stiff DNA rod, especially in its single-stranded region. Thus, even if the anchors extend outwards more than the motors do, their flexibility is such that the nanotubes can still reach the motors and glide.

Orthogonal Tubes

One advantage of the launch control system over simply adding or removing ATP from the buffer is that multiple populations of nanotubes can coexist and be cycled

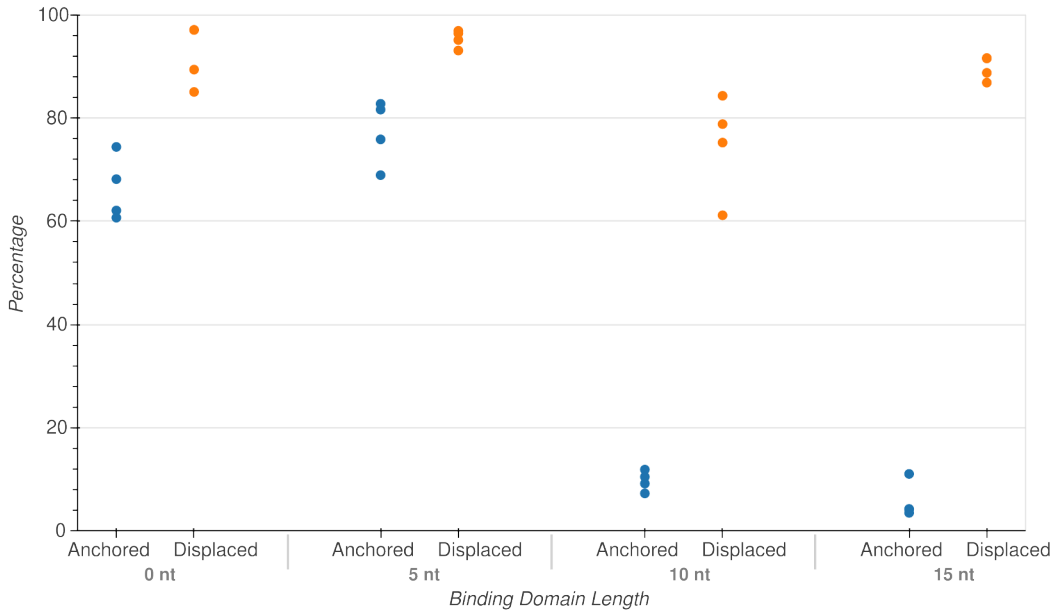

Figure 4.6: Effect of the strength of the binding between nanotubes and anchor strands on gliding. Four different versions of strand C are tested, progressively increasing the length of the binding domain from 0 nt to 15 nt. The percentage of nanotubes that move more than 1 µm over the entire measuring window is shown on the vertical axis for the anchored and released states. For each condition, two fields of view on two different slides are imaged and measured.

between different states independently. Designing two sets of anchor complexes and overhangs on the nanotubes would be trivial and their respective invader strands could be added to control either population separately. We initially tried annealing two sets of DAE nanotubes with the same sequences but different fluorophores (green Alexa 488 and orange Alexa 546) and we added them together in the same lane on our sample. We quickly observed that mixed tubes would start forming, where different color tubes would be found joined to each other. This is not entirely unexpected, given that the nanotubes can grow indefinitely and they are not capped after annealing, so that their sticky ends are still free to bind to other tiles or nanotubes. We cannot observe this phenomenon as easily with single-color populations as there is no clear indicator of post-annealing growth or polymerization.

To overcome this issue, we designed a new set of the strands SE2, SE4, RE2, and RE4, with orthogonal sticky ends, which would make the different populations of annealed tubes orthogonal to each other. These new tubes still retain the core sequence of the initial DAE nanotubes, so they still cannot be annealed in a single pot reaction. Even in this case we saw evidence of nanotubes of mixed color,

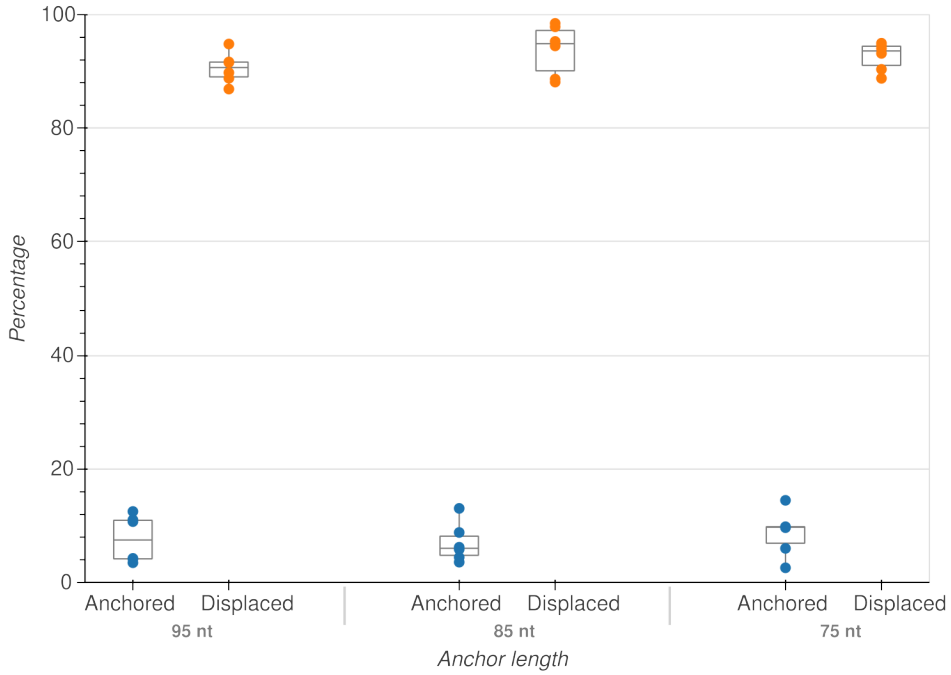

Figure 4.7: Effect of the length of the anchor complex on gliding. Three different versions of strand B are used, testing it as originally designed, dimensioned to match the size of the dynein motor, and then removing 10 and 20 nt (~4-8 nm). The percentage of nanotubes that move more than 1 µm over the entire measuring window is shown on the vertical axis for the anchored and released states. For each condition, two fields of view on three different slides are imaged and measured.

which led us to think that the core sequence of the tile can still undergo some level of rearrangement or that truncations in DNA strand synthesis can lead to tube-to-tube interactions. Neither hypothesis is fully satisfying, as we have found strand displacement within the nanotube to be rare if not impossible (more on this in Section 4.4) and we have mostly used PAGE purified DNA strands, which should have limited to no truncations. A likelier explanation is that, after annealing, the nanotubes are not purified of the free tiles and strands that have not been incorporated. When the orthogonal populations are mixed these free strands could form hybrid tiles that bridge the connection between green and orange tubes.

Finally, we decided to design an entirely orthogonal DAE nanotube, replacing the entire sequence with one previously published in Jorgenson et al., 2017. With this design we never saw evidence of hybrid nanotubes and indeed we used a version of the orthogonal DAE nanotube with the Alexa 546 dye in all of our experiments to assess the quality of the sample preparation.

4.3 Halting Gliding

The system we presented above is extremely effective at controlling gliding of nanotubes between on and off states, where we define the "on state" as what we see in traditional gliding assays with ATP and the "off state" as one where DNA nanotubes are bound to the motors, but the kick does not result in large-scale motion. However, launch control has to be carefully tuned and it has an intrinsic negative effect on the quality of the motor surface, given that motor proteins have to be replaced by DNA anchor complexes. This is especially clear when adding populations of nanotubes with different anchors, such as when we added a second color. The change in surface properties also requires the designer to re-evaluate the concentration of anchor strands and the doping of the nanotubes, as the two variables determine how close to the ideal on and off state the system can get. We studied a different approach to incorporate DNA machinery that performs a similar function directly on the nanotube, without any need to modify or degrade the surface. From preliminary data not shown here and from experiments in Ibusuki et al., 2022, we expect that, if the motor binding sequences are not all aligned in the same direction, they can cause the kick vectors to cancel out or even the motors to seize. We thus modified a strand on the DAE nanotube to have a floppy overhang and its complementary strand with the motor binding sequence. Thus, for every tile of the tube that has a MBS oriented along the axis of the tube, there is now a second floppy MBS that will be oriented randomly with thermal fluctuations. If motor proteins grab onto these misoriented binding sequences and they cannot release them, due to major-minor groove orientations or because of steric effects, we hypothesized that the nanotubes would remain anchored to the surface.

Another preliminary question that we were not able to answer satisfactorily is whether we can talk about the sum of the vectors of all the kicks as what directs the gliding. If all the MBSs were in the same orientation, we could assume that their effect would be somewhat additive and we would see large scale motion in one direction, which we do indeed observe. However, once we added a second set of just as many randomly oriented MBSs, these would statistically cancel out between themselves and their effective contribution to the gliding of the overall structure would be zero. If their contribution was zero, we might still expect to see the tubes glide thanks to the first set of correctly oriented MBSs. It is possible that kicks in one direction are hard to sustain if the structure is overall moving in the other direction, and this could cause the dynein to seize, but, with a step length of 8 nm (Reck-Peterson et al., 2006), a few backwards or sideways steps could be absorbed

by the flexibility of the DNA nanotube, more so when dynein is quite flexible in its kick (Reck-Peterson et al., 2006).

Figure 4.8 shows the results of gliding assays of DNA nanotubes with dummy binders. When the nanotubes are annealed with the strand complementary to the overhang, thus with the entire dummy binding site, they appear to be stuck to the motors in the presence of ATP, and they are only released after displacing this strand, as seen on the top right. However, when the tubes are annealed directly without the complementary strand, they appear to move significantly faster (on the bottom left), albeit still slower than unmodified DAE nanotubes, or even than launch control nanotubes with overhangs. This deserves further exploration, but it could suggest that even single-stranded motor binding sequences could be responsible for some degree of stickiness to the motor proteins.

Finally, one design constraint of this system is that we designed it such that there is one dummy binding sequence for every REd tile, corresponding to 100% doping in the previous system, hence more strand displacement reactions are needed to completely disable the dummy binding sequences.

4.4 Releasing DNA Nanotubes

An alternative way to stop gliding is to "break" the motor binding sequence, so that the DNA nanotubes fall off the motor proteins and back in solution. This is distinctly different as the off-state will result in an empty field of view, not in stopped nanotubes.

To obtain this, we designed two versions of the REd tile on the nanotube, one with the unmodified LEF1 MBS, adding just a toehold, and one with a modified version of the LEF1 MBS, adding two mismatches, hoping that the sequence would be different enough to be unrecognizable by the LEF1 foot on the re-engineered dynein. We then designed two complexes that can turn either tile into the other one, through DNA stand displacement. Figure 4.9 shows the complex that can break the binding site. The complex is made of two strands, RE3_mis will replace RE3, and RE3* is the reverse complement of RE3. RE3* will start hybridizing to RE3 through the single-stranded toehold and from there four-way branch migration will lead to RE3 being replaced by RE3_mis and RE3 forming an inert duplex with no toehold with RE3*. The energy penalty of having the two mismatches in the MBS will be compensated by the now double-stranded toehold, driving the reaction forward. A mirror complex made of RE3 and RE3_mis* is used to replace RE3_mis with RE3.

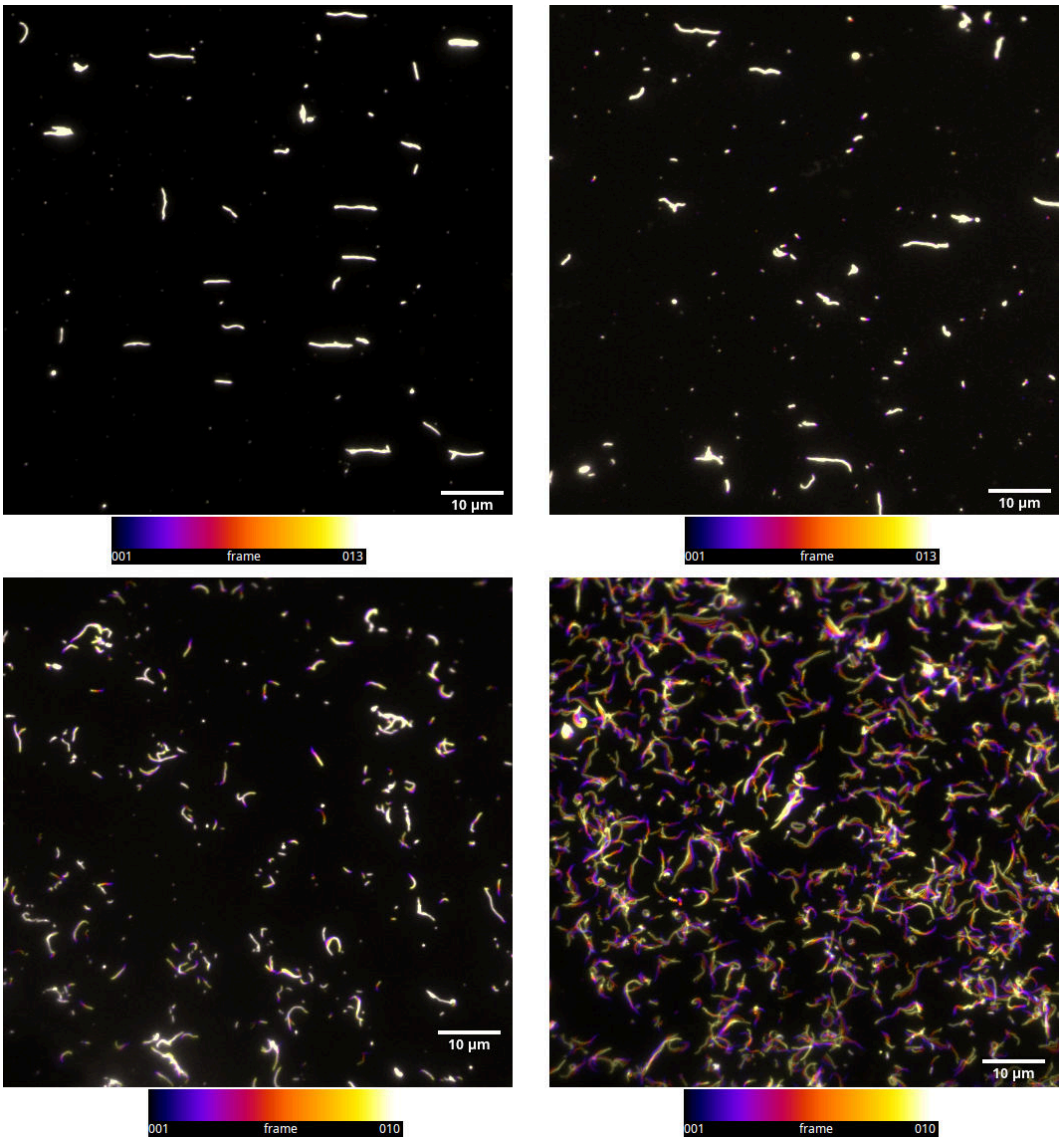

Figure 4.8: Top: On the left, temporal-color coded image of a gliding assay of nanotubes with dummy binding sites. On the right, temporal-color coded image of the same nanotubes after strand displacement. Albeit very slow, gliding is visible for many tubes through the purple shading (indicating where the tubes where in the first frames). Bottom: On the left, temporal color-coded image of nanotubes with dummy binding sites annealed without the strand complementary to the dummy binder overhang. On the right, to compare, launch control system after displacing the tubes from the anchors. The top two are imaged over 13 frames, while the bottom two only have 10 frames.

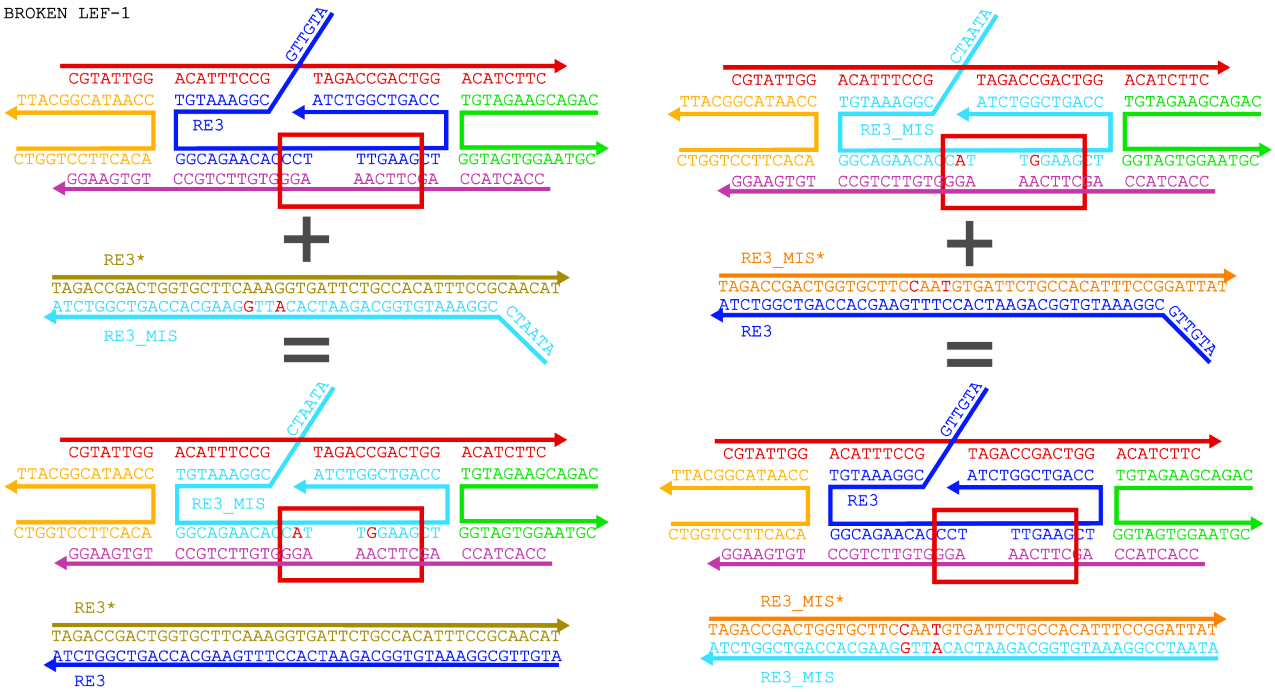

Figure 4.9: Scheme of an REd tile with a mechanism to break and form again the motor binding sequence. Left: The addition of a complex with two mismatches initiates a four-way branch migration reaction that replaces strand RE3 with RE3_mis, deactivating the MBS on the nanotube. Right: The addition of a complex with the correct MBS can replace the mismatched version and reset the nanotube to its original state.

As shown in Figure 4.10, we first verified that the DNA nanotubes with two mismatches do not bind to the protein motors. The only interactions we see are very clearly due to nonspecific adsorption on the surface in regions where the passivation is not optimal. This is evidenced by their localized adsorption at a single location on the DNA nanotube, whereas the rest of the structures is shown moving around further away from the TIRF plane in solution, clearly not bound to the motors.

However, when we tried adding the invader complex, we did not see any change in the nanotubes. LEF1 nanotubes after invasion with the mismatched complex appeared to still glide, while mismatched nanotubes invaded with the perfect LEF1 binding sequence did not bind to the motor proteins. Importantly, in this second case, the strand displacement reaction needs to happen in a test tube in solution and cannot be done on the slide under the microscope. When we add the complex, we wash the slide with it and, if the nanotubes are not bound to the motors, they will be washed away and removed from the lane. This is an experimental constraint specific

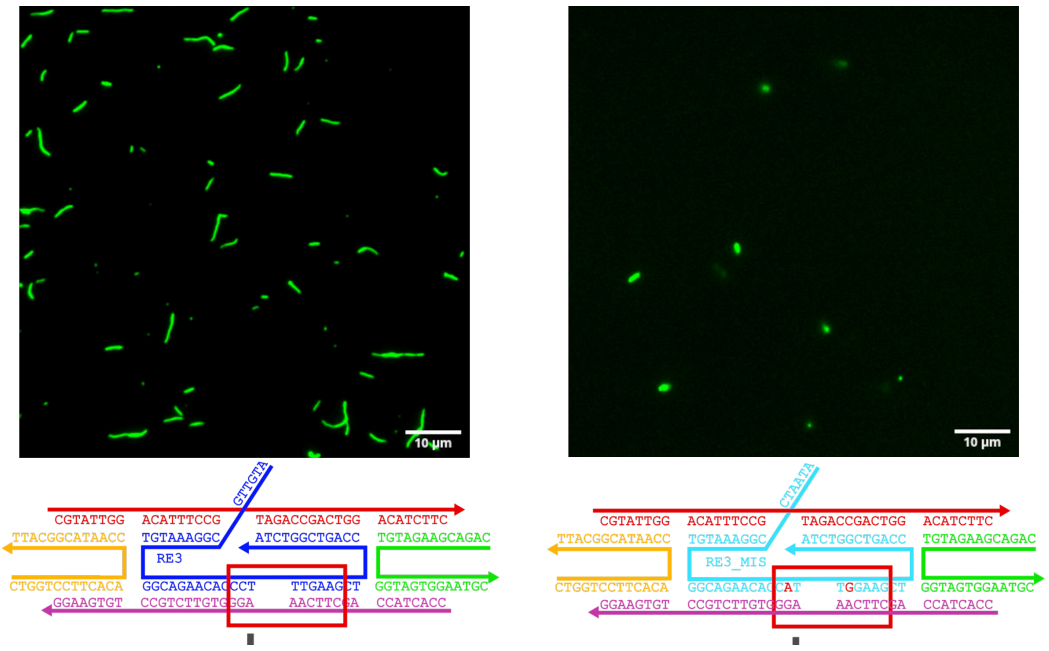

Figure 4.10: Left: DNA nanotubes with a MBS and a toehold on strand RE3 imaged on a functionalized motor protein surface. The DNA nanotubes are solidly adsorbed on the surface, but they are not gliding due to lack of ATP. Right: DNA nanotubes with a MBS with two mismatches and a toehold on strand RE3 imaged on a functionalized motor protein surface. The two mismatches are enough to block recognition and binding by the motor proteins and only few nanotubes appear to stick to the surface and only at specific points, suggesting nonspecific stickiness due to local surface imperfections. Dim nanotubes are indication of structures locally adsorbed on the surface and otherwise flailing in solution.

to this system: once we release the DNA nanotubes from the motors, we cannot add any more reagents through washes.

Four-way branch migration is known to be a much slower process compared to the three-way branch migration strategy that we have used in previous experiments, especially when a single toehold is used. To assess whether the issue was just due to the longer kinetics, we tried invading the LEF1 nanotubes and their RE5 strand simply with the complementary RE5* strand in a three-way branch migration reaction. This would detach the MBS from the DNA nanotube, making the nanotubes fall off the protein motors. A subsequent step could add the mismatched RE5_mis strand and bring the system to the desired state. The reason we initially designed the system to use four-way strand displacement from the beginning is that after the displacement reaction the nanotubes would be completely missing strand RE5 which not only contains the MBS, but also has a fundamental structural role for the DNA

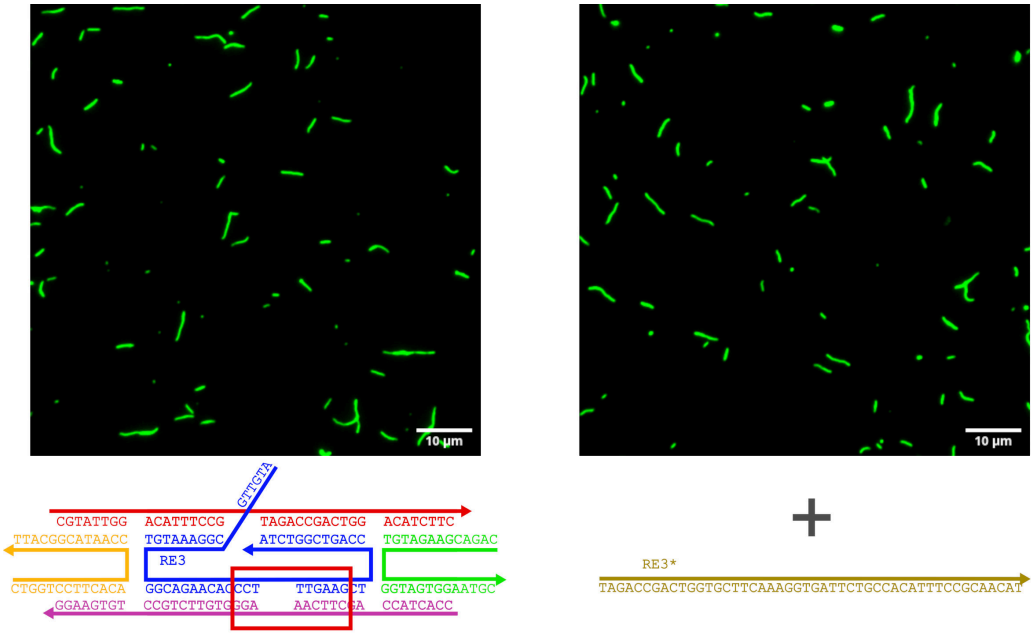

Figure 4.11: Left: DNA nanotubes with a MBS and a toehold on strand RE3 imaged on a functionalized motor protein surface. (Frame from the same timelapse as Figure 4.10) Right: DNA nanotubes with a MBS and a toehold on strand RE3 after addition of strand RE3* designed to displace RE3 and leave the MBS single-stranded and open up the DNA nanotube.

nanotube. We would expect the nanotube to fall apart after the displacement reaction. However, as shown in Figure 4.11, we again saw no difference after invasion, suggesting that even three-way branch migration is hindered.

Most strand displacement reactions happen in solution, between free complexes that can freely rotate and rearrange as the branch migration unfolds. In a DAE nanotube, the helices are heavily constrained by the crossover junctions that hold them together and they can become steric obstacles to the migration process. Furthermore, in our design the invading strand needs to wrap around a double crossover junction, which both constitutes an additional steric obstacle and also effectively creates a "threading the needle" situation. Zhang, Hariadi, et al., 2013 has shown how DNA strand displacement reaction can be integrated in DAE tiles, on the RE1 strand (symmetric to RE5), going through a double crossover. However, this happens in isolated tiles, before they have polymerized into nanotubes, removing all the steric obstacles due to the presence and constraints of other helices, and the twist that they force on each tile.

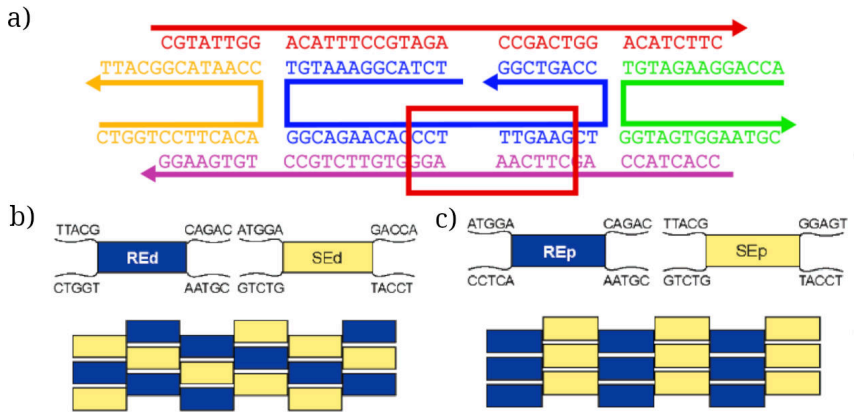

Figure 4.12: a) Scheme of the REd tile, with the MBS highlighted in red. b) Sticky end design to anneal diagonal REd/SEd DAE nanotubes. c) Sticky end design to anneal parallel REp/SEp DAE nanotubes. Adapted with permission from Rothemund et al., 2004. Copyright 2004 American Chemical Society.

Design of Longer Tile DAE Tubes

We decided to test whether the presence of a double crossover blocked the strand displacement reaction by redesigning the mechanism in an area free of junctions. On a DAE tile this means breaking the bottom strand of the REd tile (shown in Figure 4.12a) into three separate strands, two at the edges with the double crossovers and one in the middle without. The sequence between the two junctions is 21 nt long, which would have to be broken into three separate regions so that the two junctions can maintain rigidity and not come apart. The easiest solution would be to divide it into 7 nt long sections, but the middle one would not be long enough to contain the 9 nt long MBS. Furthermore, the MBS needs to be positioned in the correct major-minor groove orientation, and it should be flanked by a few basepairs on each side for rigidity. We thus decided that it would not be possible to use the original DAE tile, and we looked into replacing it with a different one. The first modification we thought of is to add two additional turns of helix (21 bp) in the middle of the tile, making the region between the two double crossovers longer but keeping the tile compatible with the tube design.

However, the REd/SEd tube design that we have used until now is diagonal, meaning that the two different tiles alternate along the circumference, as shown in Figure 4.12b. If one tile was longer than the other one, the design could not form properly due to this mismatch. We decided to keep the SEd tile as it was originally, because longer strands are harder to synthesize and more expensive, especially when incorporating a fluorophore like SE3 does. We thus looked at the design in Figure

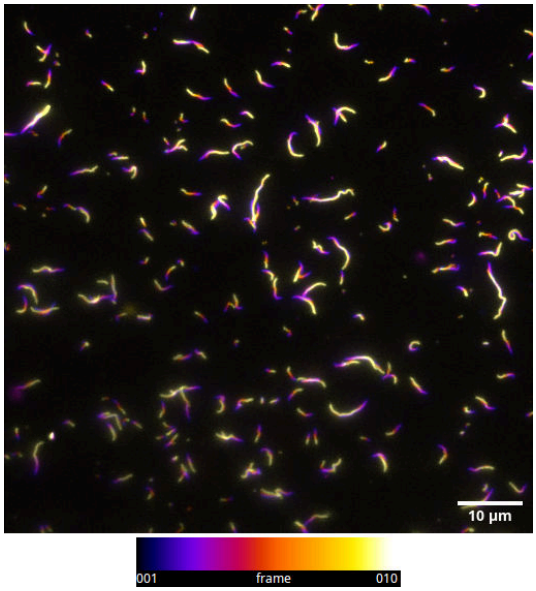

Figure 4.13: Gliding assay of a REp/SEp DNA nanotube with an incorporated MBS, imaged over 10 frames taken at 20 s intervals and visualized as a temporal-color coded image.

4.12c, with tiles REp and SEp, where only the sticky ends are modified where one circumference is formed by REp tiles and the next one by SEp, alternating between the two so that the difference in length between them does not prevent folding. As shown in Figure 4.13, we first verified gliding with the original REp/SEp design without using the longer tile, but simply incorporating the MBS on strands RE3 and RE5. While this is little more than a control experiment, the change in tiling of the REp/SEp design could result in differences in gliding due to the different spacing of the MBSs, but we do not see appreciable differences.

To design the longer REp tile, we added two 21 bp sequences to the top and bottom helices, as shown in Figure 4.14, and broke up RE3 into two different strands, as its length would otherwise approach synthesis limits. To design the two sequences, we used a simple NUPACK script adding diversity constraints and making sure that both tiles would still be orthogonal, while avoiding spurious motor binding sequences. We did not modify the sticky ends, aiming at a tile that could be integrated directly with the original SEp tile design. It is however important to remember that DAE tiles have an intrinsic twist that gives rise to tube formation and longer tiles can affect it, causing additional torsional stress during annealing. Given this issue and the use of desalted unpurified strands, compared to the usual PAGE purified strands, we decided to fold the tubes with a slower anneal protocol.

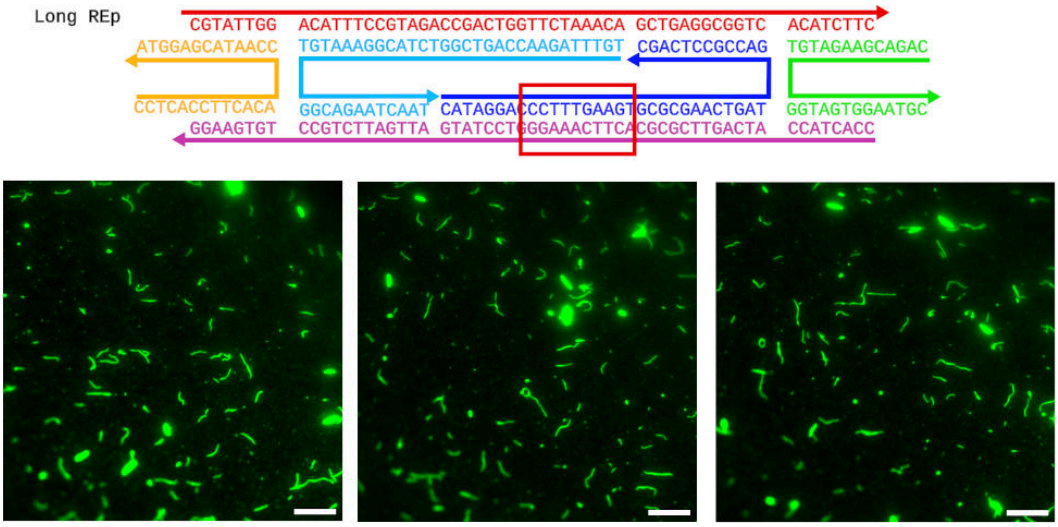

Figure 4.14: Top: Elongated REp tile with two additional turns of helix in the middle. The central strand has been broken in two for easier synthesis and the MBS is highlighted in red. Bottom: Light microscopy images of the parallel DAE nanotubes with elongated REp tile after annealing. Most structures look similar to diagonal nanotubes, with a few larger aggregates suggested by the thicker and brighter structures. Scale bar 10 μm.‘

Figure 4.14 shows that the REp/SEp nanotubes with a longer REp tile appears to anneal successfully when viewed under light microscopy. However, gliding assays show that these nanotubes stick to the motor proteins without gliding, and that this does not happen for control nanotubes designed without a MBS. Due to resource constraints, we could not further verify if there were any issues with the annealing process, but under the microscope we noticed that some nanotubes looked thicker, possibly a symptom of aggregation of bundles of nanotubes. Furthermore, we think it might be possible that the additional torsional stress could shift the position of the motor binding sequence enough to prevent successful binding, kick, and release, or that the nanotube might not fold as well as we expect.

Breaking the MBS on Dumbbells

We then looked into how we could move the motor binding sequence away from the structure of the nanotube to an area where there would be no crossover and limited steric constraints. We designed a modified version of the strand RE5 that incorporates a dumbbell extension. The dumbbell projects away from the origami and it is formed by two external hairpins and their stems where the MBS can be incorporated. Dumbbells form a Holliday junction with the helix they stem from

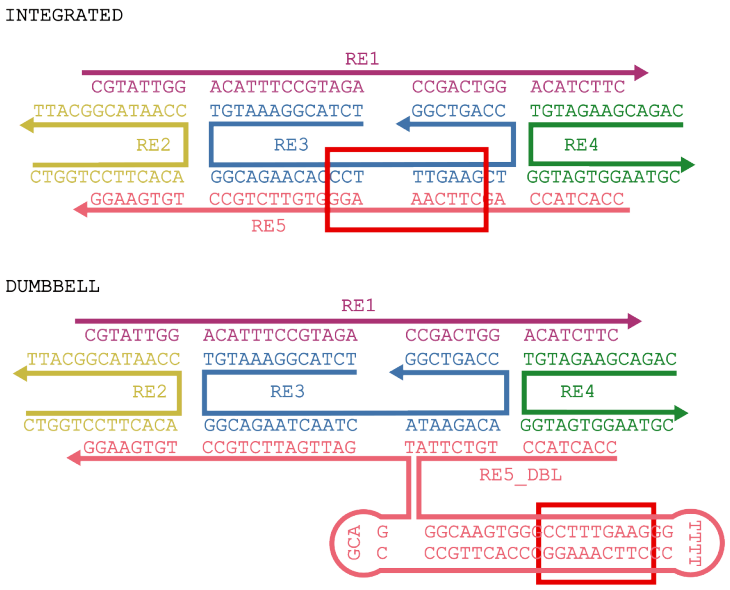

Figure 4.15: Top: design of the REd tile of a DAE DNA nanotube with an integrated binding sequence for LEF1. Bottom: design of the REd tile of a DAE DNA nanotube with the binding sequence for LEF1 moved to the a dumbbell sticking out of the RE5 strand. The MBS is highlighted in a red box.

and this junction orients the two helices at a somewhat rigid angle, as previously described in Section 1.1. Thus, while these binding sequences on dumbbells are considerably less stiff than ones incorporated into the structure, we still expect them to have a coherent average orientation that would make the DNA nanotubes glide. To test this hypothesis, we first redesigned the DAE nanotubes without an incorporated binding sequence, and we added a dumbbell to one of the strands, as in Figure 4.15. The position of the sequence on the dumbbell was chosen to obtain the correct orientation of major and minor groove for LEF1 binding. Moreover, the MBS is flanked by basepairs on both sides to increase its rigidity, as the LEF1 domain has been shown to significantly deform the DNA helix when bound (Love et al., 1995).

Assays of DNA nanotubes with dumbbells and with an integrated motor binding site are shown in Figure 4.16. Measurements of gliding speed show that nanotubes with a dumbbell are approximately 4 times slower than ones with integrated binding sequences, at the same salt conditions (350 mM KCl). We attribute the decrease in measured velocity to the floppiness of the dumbbell junction that will results in binding sites pointing in slightly different directions and the sum of the vectors of the kicks averaging these differences.

While the decrease in gliding speed is significant, it could allow us to overcome the

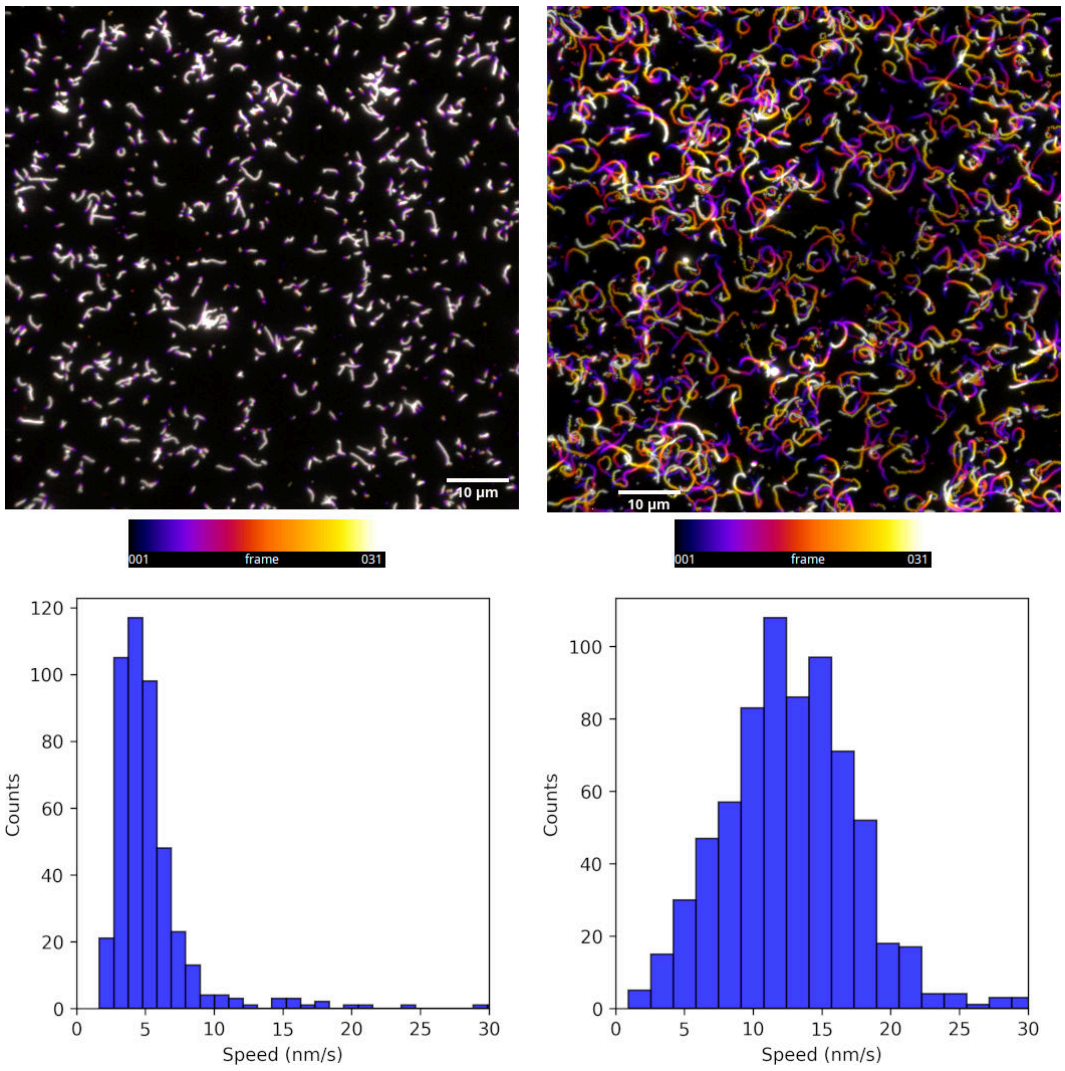

Figure 4.16: Gliding assay of DNA nanotubes with MBSs on a dumbbell on the left and with an integrated MBS on the right. Top: Temporal-color coded images over 31 frames taken at 20 s intervals. Bottom: histograms of the measured speeds for the two conditions.

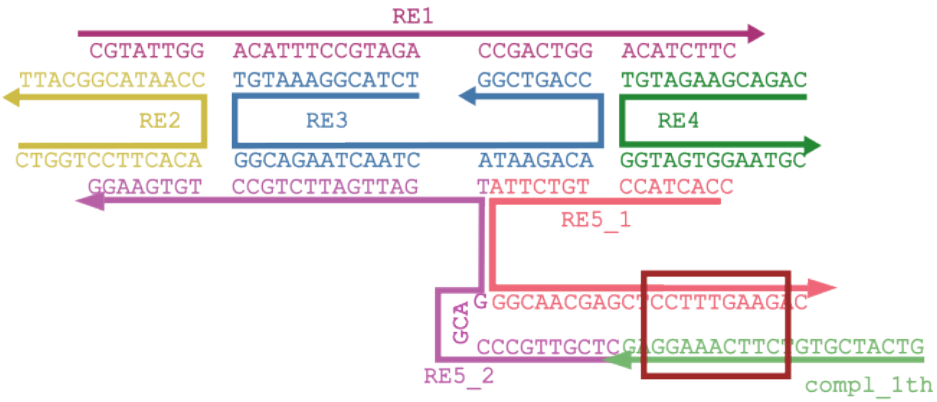

Figure 4.17: Scheme of an REd tile modified with a dumbbell incorporating the MBS. The strand `compl_1th` can be strand displaced through its toehold, effectively leaving a single-stranded MBS that the motor proteins cannot bind to. The MBS is highlighted with a red box.

obstacles we faced when attempting a DNA strand displacement reaction through a crossover. Indeed dumbbells do not have any junctions on their arms and their intrinsic flexibility makes strand displacement conditions comparable to reactions happening to duplexes in solution.

Incorporating the machinery to break the motor binding sequence on the dumbbell still requires some tweaking, as the dumbbell needs to be divided into separate strands that can be displaced. However, as shown in Figure 4.17, breaking the binding sequence here can be done simply by removing one of the strands that form that region of the dumbbell and leaving the MBS single-stranded. In the integrated binding sequence design this was not possible, as the MBS also had an important structural function in the nanotube. We can then disregard considerations about mismatches and, more importantly, we can swap a slow four-way branch migration reaction for a much faster three-way branch migration reaction.

Adding toeholds and breaking the dumbbell into multiple strands created unforeseen aggregation issues that we were able to solve only after several iteration of design. In gliding assays, the "breaking" mechanism worked very well and the nanotubes fell off the surface almost instantly after adding the invader strand. However, we noticed that the gliding on state was much slower even when compared to MBS on a dumbbell. Figure 4.18 shows a heavily zoomed in color-temporal coded image of a gliding assay, showing only minimal evidence of gliding. The movement of the nanotubes can be inferred by looking at their ends and noticing that the shadow

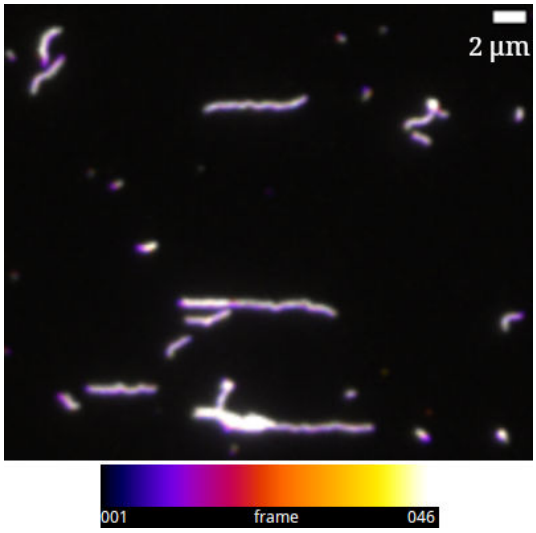

Figure 4.18: Temporal-color coded image of a modified dumbbell with a toehold to break and displace the motor binding sequence. Gliding is not clearly apparent, but it can be seen by looking at the tail ends of the nanotubes, showing that their change in position during the measurement is along their axis. Imaged over 46 frames at 20 s intervals.

of previous frames is aligned with the axis of the nanotube. This suggests that the motion is coherent and due to motor kicks, not just to stage drift. The effect is more clear when looking at the gliding assay as a video. Before we further optimize this system, it would be important to understand the issues of speed with dumbbells and whether we can improve the performance of the system as designed. Otherwise, we are in a regime where significant gliding can only be observed only over timescales that are close to the half-life of the motors and the ATP buffer.

4.5 Discussion

We have demonstrated that we can confidently modify DNA nanotubes when the additional machinery and strands is outside of the main structure of the tube, as we have shown with launch control, dummy binders, and broken dumbbells. This is a first step towards the larger picture of independent populations of gliders that we laid out at the beginning of this chapter. While qualitatively these systems are promising, we have also noticed that some of these designs, particularly dummy binders and dumbbells, take a severe hit in gliding velocity, up to the point where gliding is hardly detectable during our imaging window. However, when we tried to remediate this issue by using incorporate motor binding sequences, the addition of DNA strand displacement machinery within the structure of the nanotube has

proven very hard and our investigation suggests that the rigidity of the nanotube itself might be reason enough for the lack of any sign of displacement, or at least for a slowdown of its kinetics by several orders of magnitude. Multiple experiments also suggest that both structure and sequence need to be tweaked more precisely than we initially imagined, and that there is significant interaction between the engineered motor proteins and the DNA structures. These experiments include our design of a longer DAE tile which was shown not to glide, possibly due to aggregation issues or difficulty in folding due to torsional strain, different designs of SST tubes that are not shown here, and experiments on mutated MBSs that we will show in the next chapter.

Focusing on the system that achieves the highest gliding speed, launch control, our experiments have shown that we can design two orthogonal populations of gliders, and it is now a matter of surface optimization or sequence tweaking to demonstrate the behavior on the same surface. Multiple sets of anchors decrease the relative density of motor proteins, impacting the quality of the surface. While we have not noticed significant degradation of gliding in launch control experiments, we have been able to observe behaviors that we attribute to surface defects in many of our experiments. Nanotubes can become stuck after gliding for a few minutes, they might buckle, or start spinning on themselves. Many of these behaviors have been observed in microtubules as well (Gosselin et al., 2016; Soheilypour et al., 2015), but the LEF1-dynein surface seems more prone to them. While we would like to further improve the quality of our surface functionalization, there is scientific interest in these defects in motor-filament research, and this system could be use to investigate them.

4.6 Methods

Materials

Streptavidin-coated glass coverslips 1 mm thick were obtained from Schott US. LEF1 engineered dynein was expressed and purified by the Bio-ICT laboratory in the Advanced ICT Research Institute (Japan) and kindly provided to us by Dr. Ken'ya Furuta. TAE/Mg buffer is defined as 1x TAE, 12.5 mM $MgCl_2$. All gliding experiments were conducted in Tube Buffer (TB: 5 mM $MgCl_2$, 5.6 mM DTT, 50 mM Tris pH 8, 1 mM EGTA, 350 mM KCl).

DNA Nanotubes Preparation

All DNA strands were ordered from IDT. Unless otherwise specified, strands were ordered PAGE purified, except for fluorophore-modified strands which were ordered HPLC purified To anneal nanotubes, the concentration of each strand was first measured with a spectrophotometer and diluted to 10 µM in water, then the strands were mixed at a 400 nM concentration in TAE/Mg buffer before annealing. The annealing protocol consists of a first step where the mix is held at 90 °C, before being cooled from 90 °C to 50 °C at a rate of 1 °C/min. Then the rate is slowed to 0.1 °C/min between 50 °C and 30 °C and finally to 0.02 °C/min between 30 °C and 20 °C. Conventional DAE nanotubes can be annealed successfully with less careful protocols, but we believe that the slower anneal is beneficial for the long REp/SEp tubes. The nanotubes are never purified of free strands and tiles after annealing.

Sample Preparation

Streptavidin coated glass coverslips were bonded to a glass slide with a parafilm layer heated to 75 °C to melt the parafilm. They were then incubated with a casein buffer (1x TB, 1 mg/ml Casein) for three minutes to dissolve the protective coating on the coverslip. The lanes were then washed with 2-3x their volume of casein buffer and incubated for 5 minutes to passivate the surface and prevent DNA adsorption. The lanes were then washed with 5x their volume of 1x TB. 10 µl of motor proteins were diluted with 8 µl of 1x TB and then added to the lanes, before incubating for 10 minutes. The lanes were then washed with 5x their volume of 1x TB. 0.5 µl of the annealed nanotubes were diluted with 9.5 µl of TB and flowed into the slide, incubating for 10 seconds before washing the lanes with 5x their volume of 1x TB.

Gliding Assays

All light microscopy imaging was performed under TIRF with a 100x oil objective. An energy buffer with ATP recyclers (1x TB, ~25 units/ml pyruvate kinase,~38 units/ml lactic hydrogenase, 25 mM phosphoenolpyruvic acid) . The preparation of PKLDH used contains monovalent ions, and thus the concentration of KCl in TB was decreased to maintain the final concentration of monovalent ions at 350 mM. After flowing in energy buffer, the slides were immediately imaged capturing one frame every 20 seconds. Multiple lanes and field of views were imaged during the interval by moving the stage on the xy axes. Most samples were imaged for 10 minutes or 31 frames.

Launch Control Assays

When mixing strands for launch control nanotubes, strand RE3 was mixed with the modified RE3_mod according to the desired doping percentage to obtain a final concentration for RE3+RE3_mod of 400 nM. The anchor complexes were annealed with strand A at 10 μM, strand B at 20 μM, and strand C at 40 μM, holding them at 90 °C for 5 minutes and then following a 1 °C/min annealing ramp from 90 °C to 20 °C. 1 μL of annealed complex was then diluted in 19 μL of TB. The sample was prepared as described previously, except for the dilution of the motor proteins. For each lane, 2 μL of motor proteins were mixed with 1 μL of the diluted anchor complex. For the displacement reaction, the energy buffer was supplemented with the invader strand at a concentration of 15 μM. To displace the nanotubes, after imaging them in energy buffer, the lanes were washed with 5x their volume of invader strand-supplemented buffer and imaged immediately.

Chapter 5

TOWARDS ROBUST GLIDING OF ARBITRARY DNA NANOSTRUCTURES ON ENGINEERED MOTOR PROTEINS

5.1 Introduction

Controlling the shape of the glider could allow us to explore interesting behaviors, for example at friction interfaces where the gliders are predicted to undergo a diffraction phenomenon based on their aspect ratio similar to Snell's law (Ross et al., 2022). Different DNA origami could be designed to have virtually any aspect ratio, with independent populations that can be, for example, separated from each other by designing a prism-like interface, much like what happens for different wavelengths in optics.

The ability to place motor binding sequences at precise orientations and the formation of superstructures of precisely oriented DNA origami would let the designer program the exact kind of motion that each structure exhibits, significantly deviating from the paradigm of nanotubes or microtubules gliding along their main axis. Consider for example the tile in Figure 5.1, a design from the Qian lab that can polymerize and form larger arrays of tiles where helices are found in two different and orthogonal orientations, vertically and horizontally. Remembering that the direction of the motor kick is along the orientation of the motor binding sequence, placing MBSs on vertical or horizontal helices would make the tile move in two different directions. A single tile that can polymerize can form an array like the one in Figure 5.2, where all the MBSs are aligned with the main axis of the ribbon, a design that we expect to glide similarly to a microtubule, although all the motor binding sequences are here on a single surface, not wrapped around a tube. However, moving the MBSs to the orthogonal helices would yield a ribbon that moves against its main axis, a behavior that has not been previously observed. Such a system could explore interesting regimes of the gliding theory laid out in Duke, Holy, and Leibler, 1995 and previously explained in Section 1.5. A nanotube gliding in a direction perpendicular to its main axis at every step would need to find new motors, not just at its head, but in every position, and it would have much higher stiffness, positioning it in a regime similar to a high motor density. Furthermore, by programming interactions between different tiles, we could engineer 2D arrays that

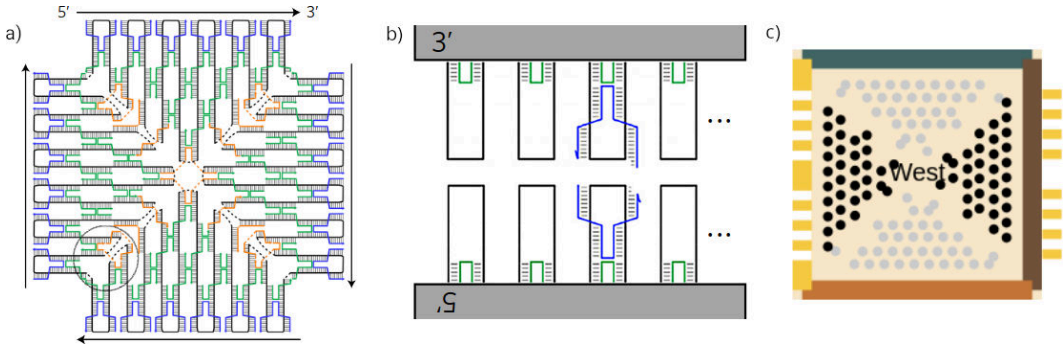

Figure 5.1: a) Tile from Tikhomirov, Petersen, and Qian, 2017, with two sets of perpendicular helices and twelve edge locations. Reproduced with permission from Springer Nature. b) Edge sticky end mechanism. An edge staple on one tile is truncated by two nucleotides, leaving two unpaired bases on the scaffold. On the other tile, an edge staple is extended by two nucleotides, with a sequence complementary to the open location on the scaffold. Reproduced with permission from Springer Nature from Tikhomirov, Petersen, and Qian, 2017. c) Schematic design of one specific tile type. Holes on the left edge indicate edge staples that have been truncated, while protrusions on the right side indicate extended edge staples that are complementary to the holes. This particular tile could bind to itself horizontally and form long 1D ribbons. In the central part of the tile, locations in black indicate sites that have been modified with a dumbbell with a MBS, in this case 68 locations on the horizontal helices. Modeled with DNA Tile Displacement Designer (https://qianlab.caltech.edu/DTDDesigner/).

can translate or rotate, as shown in Figure 5.2. Similarly, contracting and expanding arrays could be theoretically designed, yielding structures that might be collapsed or torn apart by the action of the motors. This is just a small subset of the kind of designs we could explore with more programmable DNA gliders, but we first need to make sure that we can design DNA origami gliders.

DNA nanotubes, both DAE and SST, are the only DNA structure that has been shown to glide on the engineered dynein-LEF1 complex, so, before we move to design a new class of DNA origami based gliders, we have to understand the differences between the two. The most obvious one is in their shape and dimensions: where DNA nanotubes are limited to a cylindrical shape with a cross-section of a few nanometers and micrometer-scale length, DNA origami can take any shape and are usually limited to a few tens or hundreds of nanometers in any given direction. While a DNA nanotube can theoretically keep growing until the solution is depleted of tiles, a single DNA origami is limited by the length of the scaffold it is built on.

The need for a biological template that acts as the scaffold strand for DNA origami

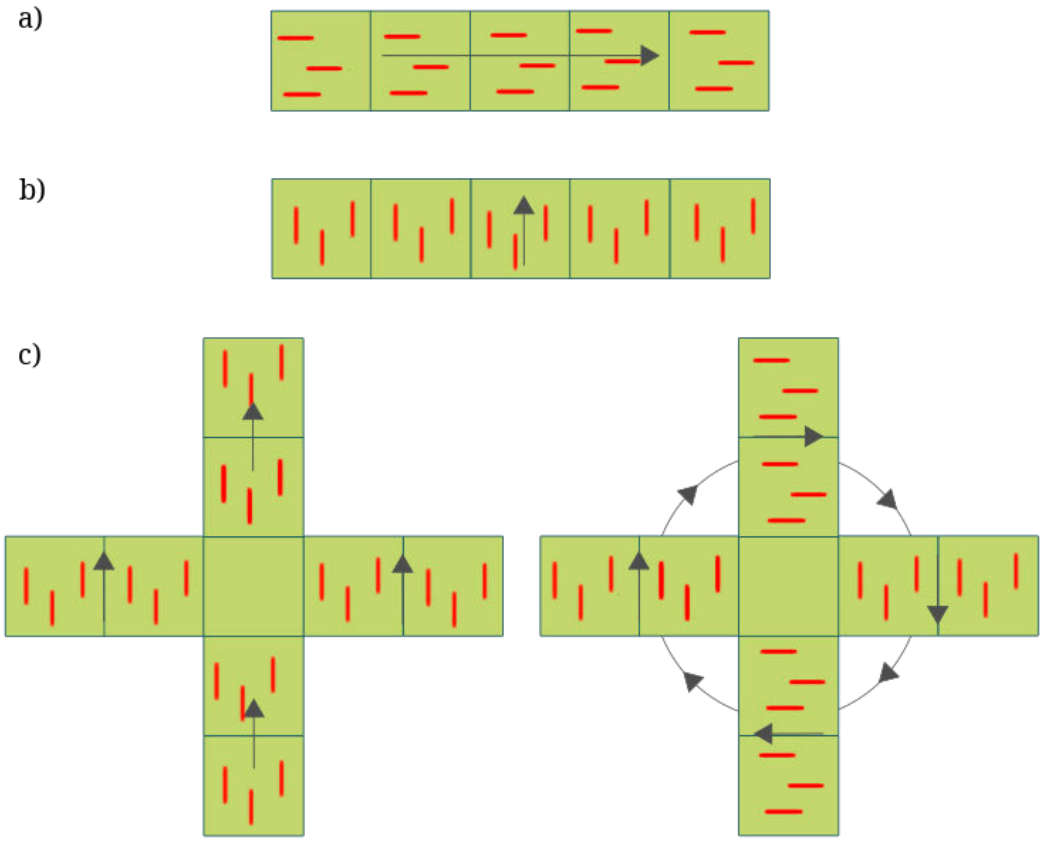

Figure 5.2: a) Design of an array made of DNA origami tiles where the motor binding sequences are aligned with the main axis of the array. b) Design of an array of DNA origami tiles with MBSs aligned perpendicularly to the main axis of the array, resulting in a structure that would glide against its axis. c) Design of two types of cross-shaped 2D arrays which exhibit translational or rotational motion based on the orientation of the MBSs on each tile.).

also means that, while the sequence of a DNA nanotube tile can be designed to accommodate a motor binding sequence, the sequence of the scaffold cannot be easily modified to allow for the origami to bind to the motors. Thus, a different system must be designed to add binding sites to a DNA origami and to that end we repurposed the dumbbell design we used on DNA nanotubes. We have shown in Section 4.4 how motor binding sequences can be moved away from the structure of the DNA nanotube and incorporated on a dumbbell projecting outside of the nanotube. Although we have measured them to be at least 4x slower than nanotubes with integrated MBS, their speed would still be sufficient to analyze gliding of DNA origami-based structures. The first obstacle we need to overcome is the difference in size between DNA origami and DNA nanotubes. While we do not necessarily

want the origami to be as big as nanotubes, we need to be able to see them under the microscope.

5.2 DNA Origami Arrays

The size of DNA origami is limited by the length of the scaffold strand, usually ~7 kbp, which results in a square tile smaller than 100 nm x 100 nm. For gliding experiments, the resolution of a light microscope can be calculated as $\lambda/2NA$ where λ is the illumination wavelength, 488 nm in our case, and NA is the numerical aperture of the objective used, 1.4 for a 100x objective in oil. This means that any object smaller than 170 nm cannot be distinguished as a single molecule. Furthermore, we want our structures to have features that make their orientation clear, so that the direction of motion can be understood with respect to the orientation of the molecule. While it is trivial to design DNA origami with absolute orientation features at the nanometer level (Gopinath et al., 2021), these could not be clearly resolved under the microscope at the micrometer level.

We examined two main categories of DNA origami arrays: boundless and bounded. A boundless array can be formed by just a single tile that is designed to be sticky to itself so that each monomer will bind to another monomer and form one continuous polymer until the solution has been depleted of tiles. The simplest design of a bounded array instead defines the position and identity of each tile that it is formed by and it would usually have as many different tiles and interactions as the number of units it is composed of. In the last fifteen years, DNA origami have been used to demonstrate both types of system.

Li, Liu, et al., 2010 showed 1D ribbon-like boundless arrays of a rectangular DNA origami tile that use additional DNA strands to link the two ends of neighboring tiles using base-pairing. Woo and Rothemund, 2011 later demonstrated that a similar behavior could be obtained through nonspecific weak stacking bonds, or by modifying the geometry of the tiles, making them fit together like pieces of a jigsaw puzzle. In the same work they also demonstrated a first example of a bounded array formed by four different tiles that have different edge geometries. An early example of a 2D array is found in Liu, Zhong, et al., 2011 where two cross-shaped tiles interact with sticky ends in solution to build a boundless lattice that spans several square micrometers. Woo and Rothemund, 2014 demonstrated a 2D array using a single rectangular DNA origami tile and again stacking bond interactions. Perhaps the most striking design of a 2D bounded DNA origami array was reported

in Tikhomirov, Petersen, and Qian, 2017 where 64 tiles with unique edge codes come together in successive anneals to form an 8x8 matrix. It is important to note the experimental difficulty of this work: each interaction had to be tweaked, so that anneal temperatures got progressively lower, as not to destroy the previously formed complex. Additionally, several different strategies had to be employed to improve the yield at each step, in order to be able to achieve the 8x8 structure at a yield of 1.81%. Even with their highly optimized incorporation rate, estimated to be 95%, a 16x16 array would only have an estimated yield of 2e-6%, making the process hardly scalable. Importantly, the 8x8 design still only measures ~650 nm x ~650 nm, resulting in a molecule with few features that could be resolved under a light microscope. These factors led us to first consider boundless 1D arrays in order to maximize length and we set out to design a ribbon-like structure that would have a similar aspect ratio as that of a DNA nanotube.

5.3 Designing a Boundless 1D DNA Origami Array

One additional important property of our system is that, as mentioned in Section 4.1, the direction of the kick of the protein motors, and hence of the gliding, is determined by the orientation of the motor binding sequence on the DNA nanostructures. This means that on each DNA origami all the MBSs have to be aligned in order for the effect of the kicks to be additive, but it also means that each tile in an array must have the same orientation, lest their contributions cancel each other. Thus, the interaction between different tiles cannot be entirely symmetrical and nonspecific, but it must recognize orientation. We first considered the design from Woo and Rothemund, 2011, where a single tile yields ribbons that are several micrometers long. The nonspecificity of the stacking bonds however means that their first design does not recognize the orientation of each monomer that gets incorporated, resulting in half the tiles oriented in one direction and half in the opposite direction. The second system they demonstrate uses edge codes to obtain highly specific orientation recognition. This is achieved by only using stacking bonds on specific helices, breaking the symmetry such that incorporating a tile in the wrong orientation would be energetically unfavorable, as it would result in fewer stacking bonds. The edge code with the lowest error rate yields a 98% correct incorporation rate. However, even after a long series of tiles in the correct orientation, after a single mistake, the orientation would be flipped and every new monomer would have the opposite orientation, until another mistake occurs. This means that while statistically a 50-mer would have a single mistake, 25 of its tiles would be pointing in one direction

and the other 25 would be pointing in the opposite direction. Half of the motor binding sequences would move the structure in one direction, while the other half would move it the other way, effectively canceling each other out, or breaking the array in two. We thus decided to focus on sticky-end interactions between tiles, which are highly specific and should not have any errors over hundreds of tiles. We used the tile from Tikhomirov, Petersen, and Qian, 2017 for the two reasons explained previously, the first one being that it has been designed to be used with sticky ends and its interactions are well characterized, and the second one being that it has DNA helices both in vertical and horizontal orientations. By moving the motor binding sequence to a perpendicular helix, it would be possible to obtain systems where the MBSs are positioned at a 90° angle.

Figure 5.1c shows the first tile design we tested. Each black dot is a staple modified with a dumbbell with the motor binding sequence, while the yellow edges represent the sticky ends we used, 8 staples each with a 2 nt complementarity. Notably, this array can be annealed in a single pot reaction, as the tiles will form at higher temperatures and then come together to form ribbons as the temperature decreases. Atomic force microscopy measurements of such structures, shown in Figure 5.3, however reveal few long ribbons and a very significant presence of aggregates, highlighted by the co-localization of large groups of tiles. The interaction between DNA and the mica substrate, mediated by divalent ions, is strong enough to flatten 3D DNA structures, thus loosely formed aggregates of tiles are imaged as clusters of tiles flattened on the surface. Interestingly, a different tile design where the dumbbells are positioned on helices perpendicular to the ribbon axis exhibits a slightly different behavior with shorter linear structures, possibly a clue as to what is causing the formation of these 3D arrays.

As described in Section 3.6, we hypothesized that the large number of dumbbells on one side of the origami might be causing significant curvature on each monomer, leading to poorly formed arrays that are not flat in solution, but only flattened when imaged on the mica surface. We then reduced the number of dumbbells to just six per origami, a number that should not cause significant curvature and could still approximate the linear density of motor binding sequences on a nanotube (1 every

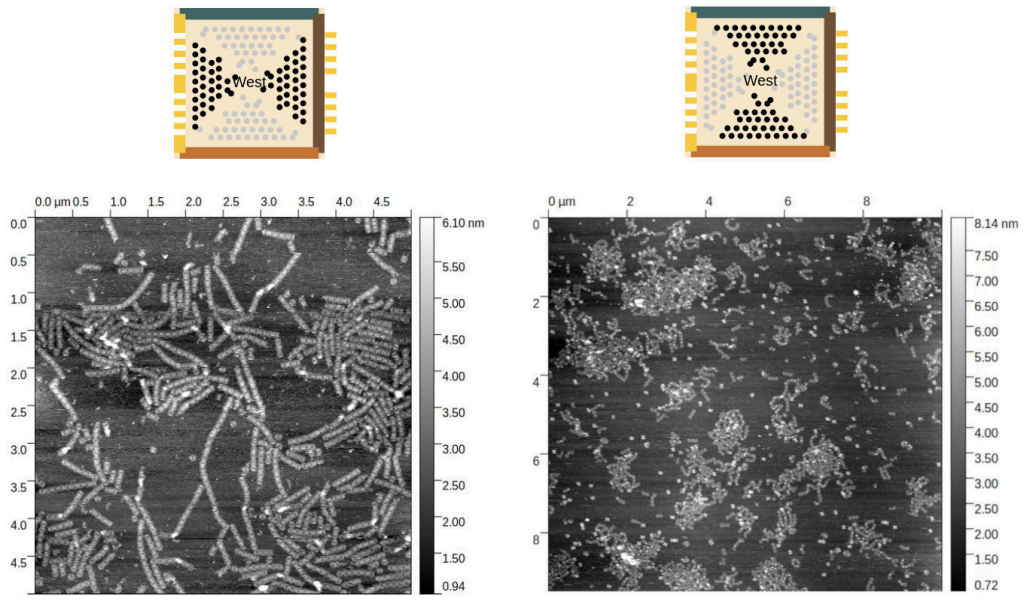

Figure 5.3: Atomic force microscopy images of two different sets of tiles designed with 8 x 2 nt sticky ends that should form ribbon-like unbounded 1D arrays. The tile on the left has been modified with 68 dumbbells on helices parallel to the ribbon axis, while the one on the right has dumbbells on helices perpendicular to the axis. Notice that the scale is different between the two images. Modeled with DNA Tile Displacement Designer (https://qianlab.caltech.edu/DTDDesigner/).

14 nm)[1]. This specific design also increased the number of binding edges to 11 per tile, which could have positive effects in binding strength, but we also realized would cause the array to start forming at higher temperatures, possibly when the monomers are not completely annealed yet, causing incorporation of defects. The AFM data supports an improvement in the level of large scale aggregation and highlights the presence of many 6-10 tiles clusters. One peculiar property is the large number of structures where two rows of tiles are found next to each other. This is again evidence of a 3D structure being flattened on the surface, as shown before in DNA nanotechnology (a particularly beautiful example is the icosahedron in Tikhomirov, Petersen, and Qian, 2018). Specifically, we are likely seeing rings of DNA tiles that have closed on themselves, limiting the size of the array, but also yielding a DNA

[1]The ideal density of MBSs is a problem we do not have a good answer to. Ibusuki et al., 2022 showed a difference in velocity based on MBS position on DNA nanotubes, but it is unclear how such a mechanism works. On a diagonal DAE nanotube, while the MBS appears on a single helix only every four tiles, it appears on the neighboring helix with every tile, meaning that their density could be higher if some amount of rotation is allowed. If we move away from a 1D paradigm, it might also be important to switch from a concept of linear density to one of surface density, for example if DNA has some level of nonspecific stickiness to the motor proteins.

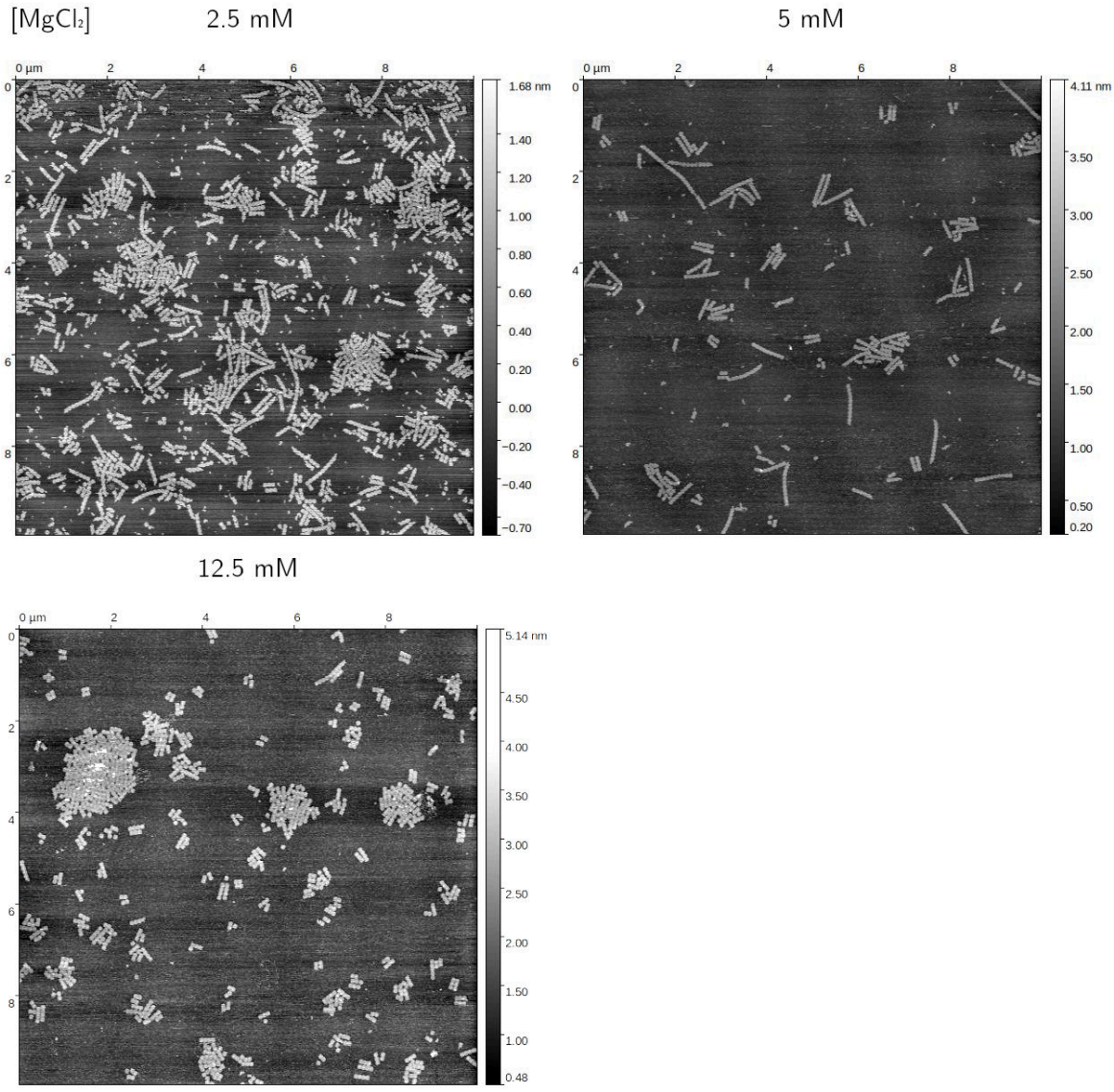

Figure 5.4: 1D array of DNA origami tiles annealed at three different concentrations of $MgCl_2$

.

structure that is very different from our original design. This phenomenon is due to the flexibility of single layer DNA origami and it is exacerbated by the high melting temperatures of these arrays and by the structure of this tile, where the two diagonals are fairly flexible seams.

One way to make DNA nanostructures less flexible is to reduce their melting temperature, reducing their kinetic energy and decreasing the flexibility of the junctions (Niu et al., 2016). We reduced the number of edges to 6 in order to decrease the

melting temperature and we also reduced the concentration of magnesium chloride during annealing. As evidenced in Tikhomirov, Petersen, and Qian, 2018, magnesium is known to stabilize DNA duplexes (Owczarzy et al., 2008) and to reduce spacing between helices (Fischer et al., 2016), so that lowering its concentration would make the arrays less stable at higher temperatures. We annealed it at different $MgCl_2$ concentrations, 2.5 mM, 5 mM, and the baseline 12.5 mM. As shown in Figure 5.4, 2.5 mM might be too low to anneal well-formed tiles, but the 5 mM condition yields longer ribbons than what we observe at 12.5 mM. While the presence of rings is still obvious, they are larger than before, suggesting that the flexibility of the tile has indeed been mitigated. We do not know how ring-like structures would behave in a gliding assays, but we see linear fragments that are up to 1-2 µm long, which should be visible and distinguishable under the light microscope. Even if we have not yet reached the 10-15 µm length of a DNA nanotube, we can already use these chains of DNA origami to test gliding on motor proteins.

5.4 Tubular origami design

We decided to first focus on testing whether we could observe any gliding of DNA origami structures on motors, before introducing DNA origami arrays. We looked at a different DNA origami design that is more comparable in shape to DNA nanotubes, in order to minimize differences between the two systems. We chose a six-helix bundle origami (Bui et al., 2010), shaped like a tube with six helices and a length of approximately 400 nm. Eight staples all on the same helix were modified to add a dumbbell with the LEF1 binding sequence, using the same design shown for DNA nanotubes in Section 4.4. The six-helix bundle was folded in two versions, a control without dumbbells, and the modified version with eight dumbbells. Figure 5.5 shows field of views from the control and the modified origami when imaged on a glass slide functionalized with motor proteins, comparable to a gliding assay. The density of structures on the motor surface does not seem different between the two conditions and, additionally, no gliding was observed once ATP was added to the system. Two possible explanations for this are either that DNA origami with the binding sequence were not sticking to the motors, or that origami were sticky even without the binding sequence, making it impossible for them to glide. It is hard to exclude either hypothesis based solely on this data, given the relatively low general density, compatible with some nonspecific stickiness where the surface presents imperfections.

We tested a second design that turns the six-helix bundle into what we called a seven-

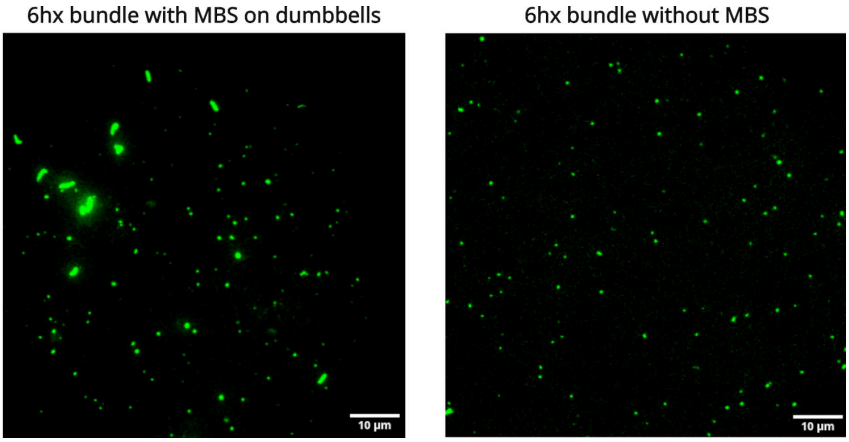

Figure 5.5: a) Six helix bundle origami with six dumbbells containing the MBS for LEF1 on a surface functionalized with motor proteins. This image shows some contamination from a control lane on the same sample that had DAE nanotubes. This was fixed in following experiments. b) Control with six helix bundle origami that do not have any MBS.

helix bundle. We decided to remove uncertainty about rigidity of the dumbbells by adding a seventh helix outside of the tube and designing this helix to be entirely formed by staples, thus giving us full control over its sequence, as shown in Figure 5.6[2]. The downside of this design is that it can promote aggregation as the binding sequence is repeated 33 times along the origami and staples that form this extra helix can start hybridizing to each other before they are attached to one scaffold strand, possibly getting incorporated into multiple origami and linking them together. The sequence of the seventh helix was carefully designed using NUPACK to minimize potential aggregation. Additionally, a version of the seventh helix without any binding sequences was designed to provide a negative control.

Gliding assays were performed for the seven-helix bundle, both with and without LEF1 binding sequences. Here orange DAE nanotubes with integrated LEF1 binding sequences were added to both lanes to confirm that the surface preparation was successful and gliding was possible. Figure 5.7 shows that the density of DNA origami between the LEF1 condition and the non-sticky control was entirely comparable. Given the very high density of origami in both conditions, it is likely that origami without any LEF1 binding sequence are very sticky on these surfaces. To screen for possible electrostatic effects while modulating binding strength, we titrated different concentration of monovalent salt, KCl, from 100 mM to 300 mM.

[2]The name seven-helix bundle is slightly misleading as the seventh helix is not part of the tube's circumference, but is projected out of it.

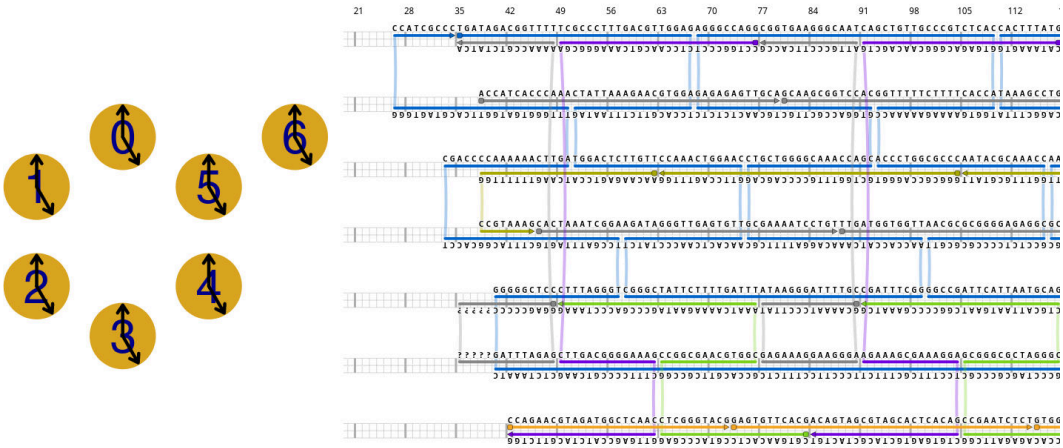

Figure 5.6: Design of a seven-helix bundle DNA origami, adding a seventh helix projecting outside of a six-helix bundle origami, as shown on the section on the left. The seventh helix is made entirely of staple strands and connecting strands, as seen in the helix structure on the right, where the added helix is shown at the bottom, made of purple and green staples connected by orange strands. Visualized in scadnano.

After ATP addition, the DNA structures seem to be bound to the motor surface in the 100 mM and 200 mM conditions. At 300 mM KCl they bind and unbind over time, suggesting that any nonspecific binding is reversible and salt-mediated. This observation alleviates our previous concerns about surface preparation: in that case spots on the glass that have not been correctly functionalized or passivated can be extremely sticky for any DNA construct, through an interaction that is effectively irreversible and not salt-mediated. To that same effect, the gliding of control DAE nanotubes in the same lane suggests that the motor surface was successfully prepared. We thus decided to focus on exploring possible causes for the nonspecific binding of DNA origami to motor proteins.

Another significant difference between the seven-helix bundle and a DAE nanotube is in their length, up to 10-15 µm for a nanotube, only 400 nm for the origami. To alleviate this concern, we used end staple strands for the seven-helix bundle that can join multiple origami end-to-end, creating concatamers that preserve the direction of the binding sequences along the main axis of the structure. Figure 5.8 shows the design of the terminal connecting staples and the distribution of structures on a motor surface. The structures seem to be more strongly bound to the surface, but they show local binding and unbinding along their length. Again, no gliding was observed.

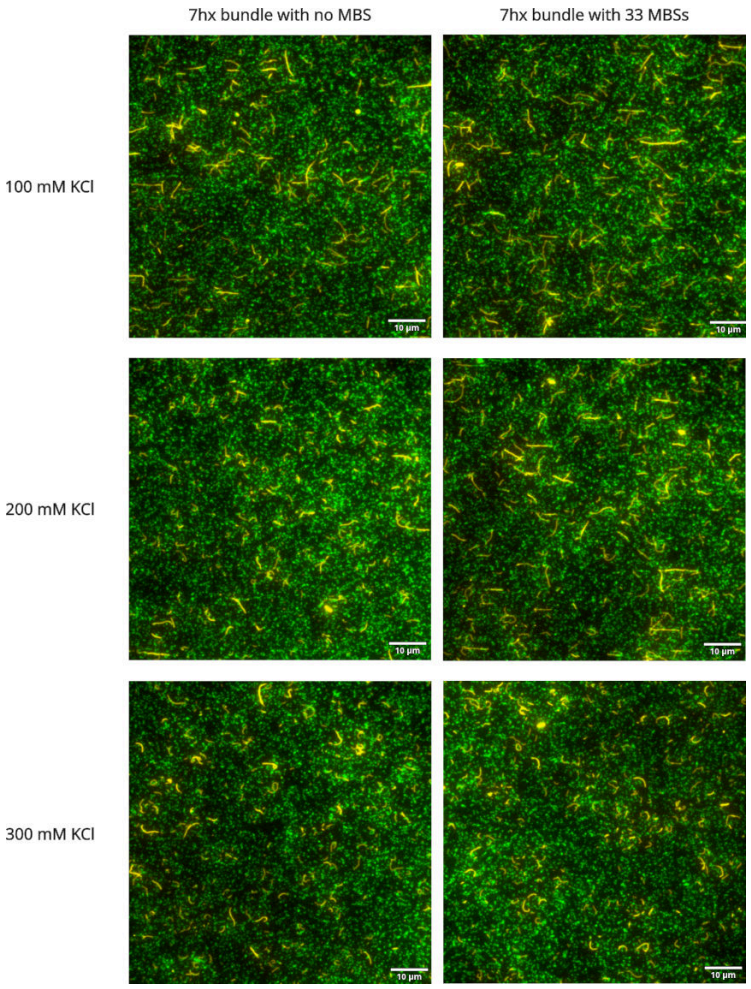

Figure 5.7: Left: In green control seven-helix bundle origami with no motor binding sequences. Right: In green seven-helix bundle origami with 33 MBSs on one helix. From top to bottom, three different monovalent salt conditions: 100-200-300 mM KCl. In orange in every image DAE DNA nanotubes with integrated MBSs, used as a control to confirm that the motor surface has been prepared successfully.

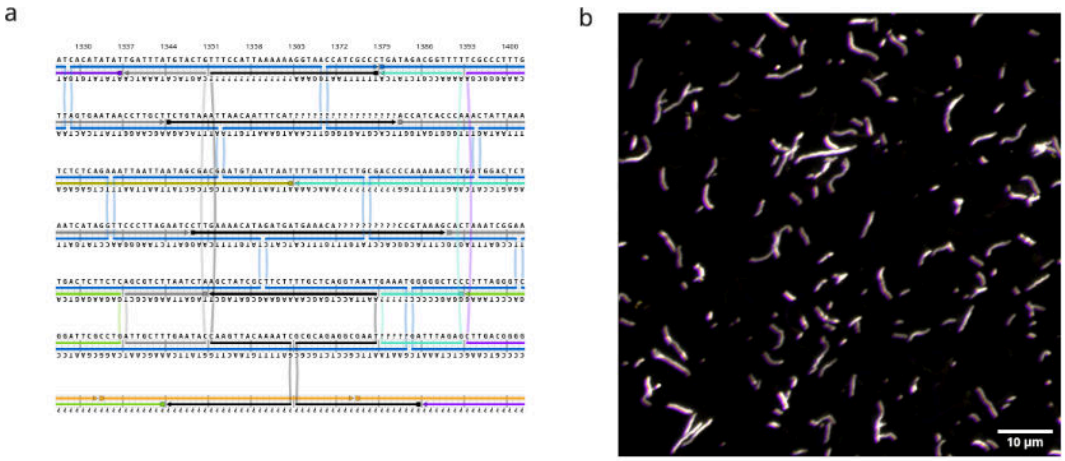

Figure 5.8: a) Design of terminal strands (in black) for the seven-helix bundle origami that connect multiple structure end-to-end, forming a concatamer. b) Field of view of seven-helix bundle concatamers on a motor surface.

5.5 Effect of single-stranded DNA domains

Many DNA origami designs incorporate single-stranded loops in various locations, either because the scaffold is not completely used up by the design, or to allow for flexibility at the edges. There are no single-stranded domains on DAE nanotubes, and we do not have a clear understanding of whether wildtype dynein, LEF1, or the engineered LEF1-dynein might show some affinity for single-stranded DNA. To test this hypothesis, and to have a more systematic approach to DNA origami, we folded a molecule that we called "labeled scaffold". This is a p8064 DNA scaffold, the same one used for the six-helix bundle, with no staples, except for the 33 staples that are used to label the six-helix bundle with fluorophores. It allows us to maximize single-stranded domain, considering that fully folded origami usually have more than 200 staples, while retaining enough fluorophores to see the origami under light microscopy.

Additionally, we annealed two other versions of the labeled scaffold with six additional staples: in one of them these are modified with a dumbbell with the MBS on it, in the other one, they are modified with a biotin tag. Given that our motor surface is prepared on streptavidin-labeled glass slides, we can use the biotin labeled scaffold to measure a positive control of how densely can DNA origami crowd this surface. This allows us to get a read of a sort of maximum fluorescence intensity. In samples where the streptavidin surface has been coated with motors, we expect to see a difference in fluorescence intensity between the labeled scaffold with no dumbbells and the one with dumbbells, if single-stranded loops do not cause non-

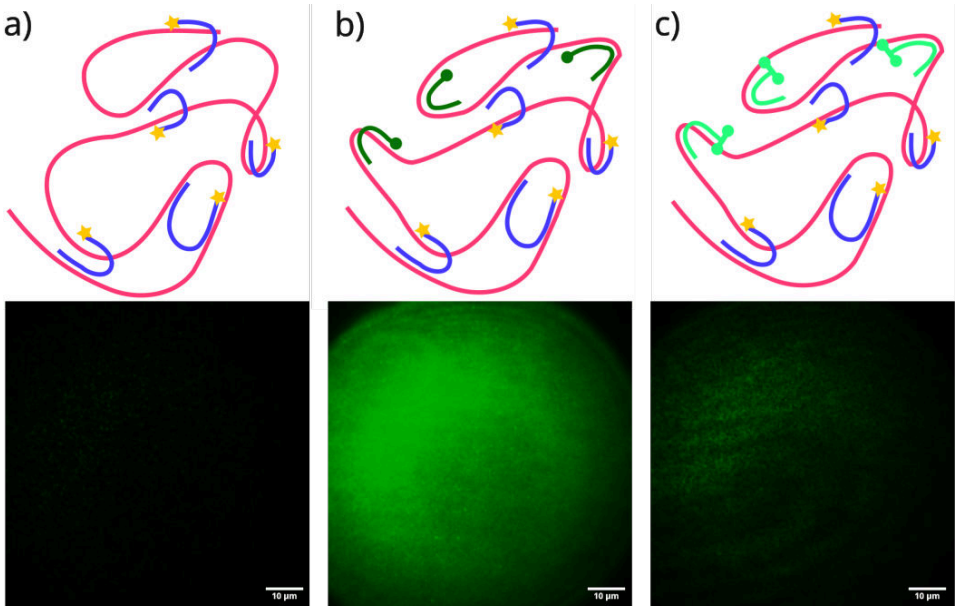

Figure 5.9: a) Top: Schematic of a scaffold strand (red) labeled with fluorophore labeled staples (blue). Bottom: Field of view of a motor surface after incubation with labeled scaffold b) Top: Schematic of the labeled scaffold with addition of six biotinylated staples (green). Bottom: Field of view of a streptavidin coated slide after incubation with biotinylated labeled scaffold c) Top: Schematic of the labeled scaffold with addition of six dumbbells with a LEF1 MBS (green). Bottom: Field of view of a motor surface after incubation with labeled scaffold with dumbbells.

specific binding. This is indeed what we observe, as shown in Figure 5.9, with a much brighter image for the sample that has MBSs on dumbbells. We posit that single-stranded loops are not a major factor in nonspecific binding of DNA origami to motor proteins.

5.6 Specificity of binding sequence recognition

Finally, we investigate how specific is the recognition of the binding sequence for LEF1. For the following discussion, it is useful to remember from Section 4.1 that LEF1 binds to a nine basepair non-palindromic DNA sequence, the MBS, specifically 5'-CCTTTGAAG-3' and its reverse complement. The orientation of the binding with regards to major and minor groove of the DNA helix determines whether and how fast gliding can happen (SI of Ibusuki et al., 2022). Interestingly for our case, the same group also reported that mismatched and misaligned sequences can result in motor binding without release, that is to say DNA structures stuck on motor proteins. Assuming perfect specificity of sequence recognition, meaning that LEF1 does not bind to anything but the sequence we reported, if the MBS was found

anywhere on the origami scaffold at the wrong orientation, it could cause the motor proteins to bind to it and seize, preventing any gliding. We checked that the MBS is not found anywhere on the scaffold sequence, but, if other sequences can trigger LEF1 binding, this could explain the evidence we have reported where origami that have no MBS still stick to the motors.

We decided to first investigate sequences close to the MBS, specifically single and double nucleotide mutations. These can happen in several ways on a DNA origami; the most obvious one would be if the sequence was present directly on the scaffold, and if it happened to be entirely contained in a single staple domain. The MBS is thus found on a single helix without any nicks, comparably to what happens on a DNA nanotube. A second possibility could be that it is found directly on the scaffold, but it is spread across two staple domains, meaning that the duplex has a nick in it. This also happens in the third case, where a single staple domain joins two non-consecutive scaffold domains, creating an MBS that would not be present in the scaffold if read linearly. Consider this last possibility, an analysis for 0-1-2 nt mutated sequences has to be performed on every origami separately, since the results depend on how the scaffold is routed. To do so we read the origami sequence by parsing the helices on a cadnano file one by one, reading the bases of each helix linearly. We then parsed this scrambled scaffold for any possible 9-mer with Hamming distance <3 from the MBS, which led us to identify 0 direct matches, 3 point mutations and 31 double mutations on the six helix bundle. Additionally, we considered the hypothesis that the reverse of the MBS might be a match, implying that LEF1 might not have a strong preference for 5'-3' versus 3'-5' orientations. This brings the number of single mutations up to 5 and double mutations up to 51.

We went back to DNA nanotubes to test the effects of mutations of the MBS on motor-DNA binding. Changing the MBS to one of its mutations on a nanotube just requires changing two strands at a time, but gliding experiments are fairly expensive both in materials and time, making a systematic study prohibitive. At the same time, testing just the MBS as a duplex can be done with a high-throughput technique such as binding assays in a PAGE gel, but the conditions would very different from what we see on a motor surface and they might not be quite representative. We tested a fairly multiplexed assay that still uses DNA nanotubes together with motor proteins that are bound to a magnetic bead. This assay was inspired by a similar protocol in Ibusuki et al., 2022 that we optimized for our experiments. LEF1-dyneins with a biotin linker—the same protein and modification we used in gliding assays—are

bound to streptavidin-coated magnetic beads suspended in solution in a test tube. When fluorescent DNA nanotubes are added to the solution, they will bind to the motor proteins based on the binding strength of the particular mutation of MBS they incorporate. Using a magnet, the beads are brought to the bottom of the test tube where they are held, while removing the remaining solution. This means that all the nanotubes that are not bound to motors will be washed away from the beads, and we can collect this wash solution. We can then measure the fluorescence of the wash, which will be inversely proportional to the amount of nanotubes that are bound to the motors. If the MBS mutation binds strongly to the motors, most of the fluorescent DNA nanotubes will be found on the beads, hence the wash will be depleted of nanotubes, yielding a low fluorescence signal. The final measurement can be performed using a plate reader over multiple samples at the same time, allowing us to test different mutations in a single assay. Importantly, the signal is quantitative, a measurement of absolute fluorescence, and does not require further manual intervention, such as counting the number of bound or gliding nanotubes in a field of view.

Figure 5.10 shows the result of a magnetic bead experiment with three different single nucleotide mutations of the LEF1 binding sequence. Two controls are added: nanotubes without MBS show a high signal, meaning that most nanotubes did not bind to the motors, while nanotubes with the unmutated LEF1 sequence show a low signal, as they were bound to the motors on beads. For two of the mutated sequences we see signal close to the nanotubes without MBS, suggesting that a mutation in those positions is sufficient to completely disrupt the binding between LEF1 and the DNA duplex. However, one mutation, a cytosine in position 8, still exhibits some degree of affinity to the LEF1 binder, with a measured fluorescence halfway between the negative and positive controls. This suggests that the binding of LEF1 is not entirely specific and that some relatives of its binding sequence might indeed still be a good match and possibly lock the origami onto the motor surface, if not compensated for.

5.7 Discussion

Our exploration of DNA origami gliders has not proven successful, but we have been able to test several hypothesis and shine some more light on some apparent parasitic interactions between LEF1-dynein and DNA origami structures. We initially tried to incorporate MBSs on a fixed sequence structure like DNA origami by adding dumbbells on the outside of the structure, but we looked for a different solution once

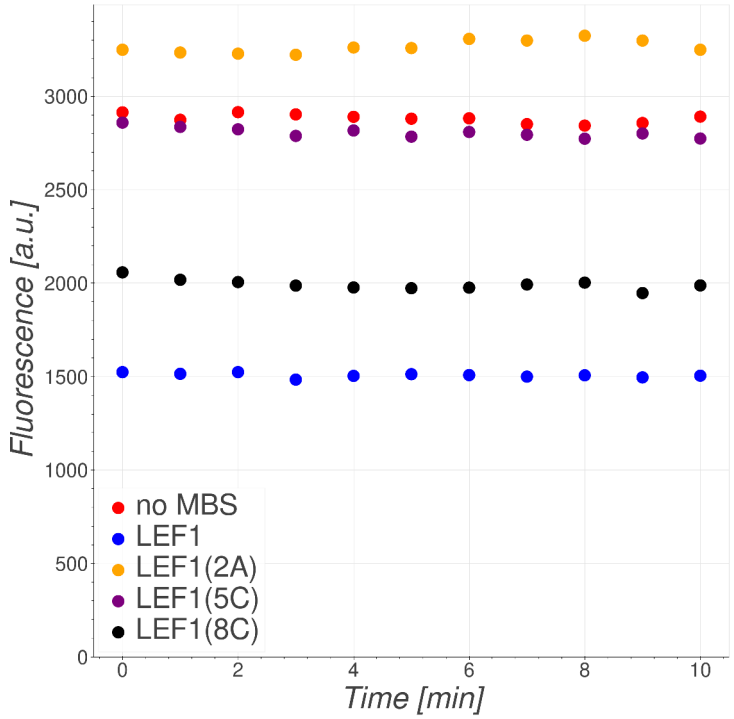

Figure 5.10: Fluorescence measurements of different DNA nanotubes after a magnetic beads assay, a higher fluorescence signal indicates lower binding affinity. A positive and negative control are established with a DNA nanotube with the unmutated MBS and one without MBS. The other three conditions exhibit a point mutation in one of the 9 basepairs of the MBS.

we realized how slow and unstable gliding of dumbbells is when applied to DAE nanotubes. Our design of 6 helix and 7 helix bundles aimed to start from a structure that resembles as closely as possible a nanotube or a microtubule. This seems important to us because we do not have a clear picture of how gliding happens in DNA nanotubes. For example, given that the tubes have MBSs all around their circumference, the direction of the kick could deviate significantly from the orientation of the MBS, but the tube might be able to accommodate that by spinning and presenting a new MBS on the surface. However, this might not happen in a flat tile that cannot undergo any torsional motion, and it would still look different on a 6 helix bundle like ours where the motor binding sequences are found on a single helix. Furthermore, DNA, through the negative charge of its backbone, might exhibit electrostatic interactions with the proteins on the surface, and the strength of these interactions would be proportional to the exposed surface area, making a flat tile much stickier than a tube that exposes a single helix to the surface.

From experiments with our design of a labeled scaffold, we confirmed that single

stranded loops do not cause significant nonspecific binding of origami, but we got some evidence that the large sequence variability of the DNA origami scaffold might be responsible for the spurious interaction. Off-target binding of promoters and other proteins to DNA is well demonstrated in biology (Agback et al., 1998; Slattery et al., 2014) and the length of the unique sequence of a DNA origami is approximately 50 times the one of a DNA nanotube, making spurious interactions much more likely. With evidence of parasitic motor binding sequences, we would now need to explore the entire sequence space of the origami to ascertain what is causing nonspecific binding. We realized that the time cost of this analysis would be prohibitive and that it would go beyond the scope of our project. We decided to stop our exploration here, but we will suggest a couple of ways to move forward in the next chapter.

Chapter 6

CONCLUSIONS

This work delves in and answers questions about two potential applications of DNA nanotechnology: one focused on translational research and one focused on exploring biological systems, one using DNA nanotech to extract information from a sample, one using it to control a system.

Every question we asked ourselves branched out into multiple questions, some we answered, some we could only probe and poke at. Every door I found got me excited to peek at what was on the other side, I tried to knock at as many as I could, but I only managed to open a few.

We demonstrated a modular DNA biosensor that can be adapted to a range of analytes thanks to the size and programmability of DNA origami, and to the use of simple components that can be regenerated or replaced. The idea that such a system could now be limited only by the availability of binders for a specific molecule is extremely appealing compared to the need to redesign EDNA molecules for different targets. I was particularly fascinated by the significant improvement in gain per binding event that we achieve by labeling the lilypad with 70 MB molecules compared to the usual single reporter systems. However, this was not immediately reflected in the data we collected, where LOD was not found to be much lower. We questioned whether we were indeed seeing the contribution of all the reporters and we did not get a solid answer. Furthermore, as we discussed, increasing the number of reporters might not directly translate to lower LOD, if the off-signal is proportional to their number. As we studied the effect of the overhangs on the lilypad molecule, we wondered more and more about the use of different geometries and the flexibility of single-layer DNA origami. We got a taste of these effects, but stiffer structures require more careful optimization of the molecules.

From a system that can be adapted to different targets it is a short conceptual step to one that can detect multiple analytes concurrently. We envision multiplexed chips to measure the concentrations of a few target proteins in a single sample. This could be achieved by using multiple chambers and electrodes in a microfluidic device, or with more creative fabrication techniques, for example by patterning a surface with oligonucleotides that bind different versions of the double-stranded linker on the

lilypad.

Before the lilypad sensor can be used with biological samples, it will need to undergo rigorous engineering to make it more robust and specific, given the various salt and pH conditions of serum, and all the possible spurious targets. We have a promising precedent in the work that has been done to translate EDNA systems to biological samples and *in vivo* setups (Arroyo-Currás, Somerson, et al., 2017). We have also seen how DNA origami, and generally larger DNA structures, can have peculiar interactions with proteins. While this step should not be taken for granted, the possibilities of our system for in vivo applications are extremely promising. Thanks to the single-molecule lilypad and the reagentless design, the sensor could be used in vivo without risks of contamination. Additionally, the reversible binders we tested will respond to changes in concentration of the analyte, allowing for continuous measurements.

The lilypad sensor is a sandwich assay, requiring one binder on the DNA origami and one binder on the surface. The proteins we showed in this work are homomers, formed by multiple identical subunits, so that two identical binders can be used to capture the same molecule by binding to the same location on two of its subunits. For monomer or heteromer proteins this approach would not work, and we would instead need to identify two binders with different epitopes. One way to use a single binder while retaining the reagentless single-step design could be to make the electrode surface nonspecifically sticky, so that proteins can be adsorbed on it. The lilypad would then have a specific binder and it would only close if the target protein was adsorbed on the surface. However, multiple binder designs have a significant specificity advantage, where the nonspecific interaction of one binder would not affect the other ones, making them a more attractive system when they can be implemented. We are confident that we could modify the lilypad to accommodate antibodies, antibody fragments, or nanobodies, opening the door to what is currently the largest class of binders and reaching the same analyte pool as the gold standard of bioassays, ELISA.

The study of the interactions between DNA and motor proteins is promising for research in both DNA nanomachines and motor-filament systems. DNA walkers have been studied extensively and they have achieved speeds of 5 nm/s (Li, Johnson-Buck, et al., 2018), which is still significantly lower than wildtype human dynein, ~1.2 µm/s (Verma, Wadsworth, and Maresca, 2024), and the LEF1-dynein from Ibusuki et al., 2022, 50 nm/s. Aside from speed, the constraints of either design

might make walker or motor-protein preferable depending on the application. As for motor-filament systems, we believe that access to more programmable gliders would both increase our understanding of their dynamics and allow us to design new behaviors.

We have shown that the toolkit of dynamic DNA nanotechnology can already be implemented to add DNA strand displacement circuitry to gliders, demonstrating new mesoscopic behaviors that could shine some light on biological motor-filament systems. We have shown control over different populations of gliders between on and off states, selectively stopping gliding. We have tested other kinds of machinery that can be incorporated in DNA nanotubes, with a focus on branch migration reactions inside the tile. While we did not achieve significant strand displacement, I am confident that we could redesign the tile, for example on SST tubes, or we could move the motor binding sequence position to a more favorable location. With the same mismatch principle, we could then have MBSs with different orientations, selectively enabling them and controlling the direction of gliding. Design of DNA nanotubes that glide against their axis are also within reach, for example by using T-junctions, and they would enable a novel type of gliding, where motors are never reused as the gliders move.

What has proven elusive is extending the paradigm of gliding nanotubes to more complex DNA nanostructures. While we have not been able to demonstrate gliding, we now have a clearer picture of how the properties of DNA origami affect their interactions with the engineered dynein motors. In our opinion, a particularly promising avenue is the study of spurious binding sequences that might be found on DNA origami. While the literature on spurious binding of LEF1 or dynein is scarce, an empirical search through the sequence of the scaffold strand is possible through the "labeled scaffold" method we demonstrated. Specifically, following a principle similar to a binary search, we could fold two incomplete DNA origami, each with one half of the staples. If one of the two showed stickiness to the motor surface, its staples could be further sub-divided, and so on until a sequence is isolated. The use of an automated liquid handler could make this study more approachable and even allow us to test 200 versions of the origami, leaving out one staple at a time.

We believe that there is enormous potential for discovery and learning once we can get DNA origami-based gliders. The ability to precisely place MBSs on the surface of the origami could help us visualize the components of the kick, both rotational and translational, in order to understand the behavior of the motors and optimize their

engineering. We could then access a new class of motor-filament systems where we can use structure to program function, creating populations of gliders with different roles and studying their interactions, in novel mesoscopic active matter systems.

BIBLIOGRAPHY

Agarwal, Siddharth and Franco, Elisa (2019). "Enzyme-Driven Assembly and Disassembly of Hybrid DNA–RNA Nanotubes". In: *Journal of the American Chemical Society* 141.19, pp. 7831–7841.

Agback, Peter et al. (1998). "Architecture of Nonspecific Protein–DNA Interactions in the Sso7d–DNA Complex". In: *Nature Structural Biology* 5.7, pp. 579–584.

Ahmad, Habib M. N., Andrade, Arturo, and Song, Edward (2023). "Continuous Real-Time Detection of Serotonin Using an Aptamer-Based Electrochemical Biosensor". In: *Biosensors* 13.11, p. 983.

Aissaoui, Nesrine et al. (2024). "Free-Standing DNA Origami Superlattice to Facilitate Cryo-EM Visualization of Membrane Vesicles". In: *Journal of the American Chemical Society* 146.19, pp. 12925–12932.

Andersen, Ebbe S. et al. (2009). "Self-Assembly of a Nanoscale DNA Box with a Controllable Lid". In: *Nature* 459.7243, pp. 73–76.

Arroyo-Currás, Netzahualcoyotl, Dauphin-Ducharme, Philippe, et al. (2020). "From the Beaker to the Body: Translational Challenges for Electrochemical, Aptamer-Based Sensors". In: *Analytical Methods* 12.10, pp. 1288–1310.

Arroyo-Currás, Netzahualcóyotl, Sadeia, Muaz, et al. (2020). "An Electrochemical Biosensor Exploiting Binding-Induced Changes in Electron Transfer of Electrode-Attached DNA Origami to Detect Hundred Nanometer-Scale Targets". In: *Nanoscale* 12.26, pp. 13907–13911.

Arroyo-Currás, Netzahualcóyotl, Scida, Karen, et al. (2017). "High Surface Area Electrodes Generated via Electrochemical Roughening Improve the Signaling of Electrochemical Aptamer-Based Biosensors". In: *Analytical Chemistry* 89.22, pp. 12185–12191.

Arroyo-Currás, Netzahualcóyotl, Somerson, Jacob, et al. (2017). "Real-Time Measurement of Small Molecules Directly in Awake, Ambulatory Animals". In: *Proceedings of the National Academy of Sciences* 114.4, pp. 645–650.

Bobinnec, Y. et al. (1998). "Centriole Disassembly In Vivo and Its Effect on Centrosome Structure and Function in Vertebrate Cells". In: *Journal of Cell Biology* 143.6, pp. 1575–1589.

Bohlin, Joakim et al. (2022). "Design and Simulation of DNA, RNA and Hybrid Protein–Nucleic Acid Nanostructures with oxView". In: *Nature Protocols* 17.8, pp. 1762–1788.

Bradley, D. F. et al. (1972). "Electric Birefringence and Dichroism of Acridine Orange and Methylene Blue Complexes with Polynucleotides". In: *Biopolymers* 11.3, pp. 645–652.

Braswell, Emory (1968). "Evidence for Trimerization in Aqueous Solutions of Methylene Blue". In: *The Journal of Physical Chemistry* 72.7, pp. 2477–2483.

Brenner, Sibylle et al. (2020). "Force Production of Human Cytoplasmic Dynein Is Limited by Its Processivity". In: *Science Advances* 6.15, eaaz4295.

Buck, Kenneth B. and Zheng, James Q. (2002). "Growth Cone Turning Induced by Direct Local Modification of Microtubule Dynamics". In: *Journal of Neuroscience* 22.21, pp. 9358–9367.

Bui, Hieu et al. (2010). "Programmable Periodicity of Quantum Dot Arrays with DNA Origami Nanotubes". In: *Nano Letters* 10.9, pp. 3367–3372.

Buskermolen, Alissa D. et al. (2024). "Towards Continuous Monitoring of TNF-α at Picomolar Concentrations Using Biosensing by Particle Motion". In: *Biosensors and Bioelectronics* 249, p. 115934.

Bussi, Giovanni, Donadio, Davide, and Parrinello, Michele (2007). "Canonical Sampling through Velocity Rescaling". In: *The Journal of Chemical Physics* 126.1, p. 014101.

Cash, Kevin J., Ricci, Francesco, and Plaxco, Kevin W. (2009). "An Electrochemical Sensor for the Detection of Protein–Small Molecule Interactions Directly in Serum and Other Complex Matrices". In: *Journal of the American Chemical Society* 131.20, pp. 6955–6957.

Castro, Carlos Ernesto et al. (2011). "A Primer to Scaffolded DNA Origami". In: *Nature Methods* 8.3 (3), pp. 221–229.

Chandrasekaran, Arun Richard (2021). "Nuclease Resistance of DNA Nanostructures". In: *Nature Reviews Chemistry* 5.4, pp. 225–239.

Chandrasekaran, Arun Richard et al. (2021). "DNA Nanoswitch Barcodes for Multiplexed Biomarker Profiling". In: *Nano Letters* 21.1, pp. 469–475.

Chew, Yean Ming and Cross, Robert A. (2023). "Taxol Acts Differently on Different Tubulin Isotypes". In: *Communications Biology* 6.1, p. 946.

Clark, Vincent, Pellitero, Miguel Aller, and Arroyo-Currás, Netzahualcóyotl (2023). "Explaining the Decay of Nucleic Acid-Based Sensors under Continuous Voltammetric Interrogation". In: *Analytical Chemistry* 95.11, pp. 4974–4983.

Dauphin-Ducharme, Philippe, Arroyo-Currás, Netzahualcóyotl, Adhikari, Ramesh, et al. (2018). "Chain Dynamics Limit Electron Transfer from Electrode-Bound, Single-Stranded Oligonucleotides". In: *The Journal of Physical Chemistry C* 122.37, pp. 21441–21448.

Dauphin-Ducharme, Philippe, Arroyo-Currás, Netzahualcóyotl, Kurnik, Martin, et al. (2017). "Simulation-Based Approach to Determining Electron Transfer Rates Using Square-Wave Voltammetry". In: *Langmuir* 33.18, pp. 4407–4413.

Dauphin-Ducharme, Philippe, Arroyo-Currás, Netzahualcóyotl, and Plaxco, Kevin W. (2019). "High-Precision Electrochemical Measurements of the Guanine-, Mismatch-, and Length-Dependence of Electron Transfer from Electrode-Bound DNA Are Consistent with a Contact-Mediated Mechanism". In: *Journal of the American Chemical Society*.

Dauphin-Ducharme, Philippe and Plaxco, Kevin W. (2016). "Maximizing the Signal Gain of Electrochemical-DNA Sensors". In: *Analytical Chemistry* 88.23, pp. 11654–11662.

Debiais, Mégane et al. (2020). "Splitting Aptamers and Nucleic Acid Enzymes for the Development of Advanced Biosensors". In: *Nucleic Acids Research* 48.7, pp. 3400–3422.

Doniger, Jay, Warner, Robert C., and Tessma, Irwin (1973). "Role of Circular Dimer DNA in the Primary Recombination Mechanism of Bacteriophage S13". In: *Nature New Biology* 242.114, pp. 9–12.

Doty, David, Lee, Benjamin L, and Stérin, Tristan (2020). "Scadnano: A Browser-Based, Scriptable Tool for Designing DNA Nanostructures". In: *DNA 2020: Proceedings of the 26th International Meeting on DNA Computing and Molecular Programming*. Ed. by Cody Geary and Matthew J. Patitz. Vol. 174. Leibniz International Proceedings in Infor-

matics (Lipics). Dagstuhl, Germany: Schloss Dagstuhl–Leibniz-Zentrum für Informatik, 9:1–9:17.

Douglas, Shawn M., Dietz, Hendrik, et al. (2009). “Self-Assembly of DNA into Nanoscale Three-Dimensional Shapes”. In: *Nature* 459.7245, pp. 414–418.

Douglas, Shawn M., Marblestone, Adam H., et al. (2009). “Rapid Prototyping of 3D DNA-origami Shapes with caDNAno”. In: *Nucleic Acids Research* 37.15, pp. 5001–5006.

Doye, Jonathan P. K. et al. (2023). “The oxDNA Coarse-Grained Model as a Tool to Simulate DNA Origami”. In: *DNA and RNA Origami*. Ed. by Julián Valero. Vol. 2639. New York, NY: Springer US, pp. 93–112.

Duckett, D. R., Murchie, A. I., and Lilley, D. M. (1990). “The Role of Metal Ions in the Conformation of the Four-Way DNA Junction”. In: *The EMBO journal* 9.2, pp. 583–590.

Duke, Thomas, Holy, Timothy E., and Leibler, Stanislas (1995). “"Gliding Assays" for Motor Proteins: A Theoretical Analysis”. In: *Physical Review Letters* 74.2, pp. 330–333.

Eichman, Brandt F. et al. (2000). “The Holliday Junction in an Inverted Repeat DNA Sequence: Sequence Effects on the Structure of Four-Way Junctions”. In: *Proceedings of the National Academy of Sciences of the United States of America* 97.8, pp. 3971–3976.

Endo, Masayuki et al. (2015). “Single-Molecule Visualization of the Activity of a Zn2+-Dependent DNAzyme”. In: *Angewandte Chemie International Edition* 54.36, pp. 10550–10554.

Fan, Chunhai, Plaxco, Kevin W., and Heeger, Alan J. (2003). “Electrochemical Interrogation of Conformational Changes as a Reagentless Method for the Sequence-Specific Detection of DNA”. In: *PNAS* 100.16, pp. 9134–9137.

Ferguson, Brian Scott et al. (2013). “Real-Time, Aptamer-Based Tracking of Circulating Therapeutic Agents in Living Animals”. In: *Science Translational Medicine* 5.213, 213ra165.

Fischer, Stefan et al. (2016). “Shape and Interhelical Spacing of DNA Origami Nanostructures Studied by Small-Angle X-ray Scattering”. In: *Nano Letters* 16.7, pp. 4282–4287.

Freeman, David M. E. et al. (2023). “Continuous Measurement of Lactate Concentration in Human Subjects through Direct Electron Transfer from Enzymes to Microneedle Electrodes”. In: *ACS Sensors* 8.4, pp. 1639–1647.

Fu, T. J. and Seeman, Nadrian C. (1993). “DNA Double-Crossover Molecules”. In: *Biochemistry* 32.13, pp. 3211–3220.

Funck, Timon et al. (2018). “Sensing Picomolar Concentrations of RNA Using Switchable Plasmonic Chirality”. In: *Angewandte Chemie International Edition* 57.41, pp. 13495–13498.

Gál, J. et al. (1999). “Directional Cloning of Native PCR Products with Preformed Sticky Ends (Autosticky PCR)”. In: *Molecular and General Genetics MGG* 260.6, pp. 569–573.

Ge, Zhilei et al. (2019). “Constructing Submonolayer DNA Origami Scaffold on Gold Electrode for Wiring of Redox Enzymatic Cascade Pathways”. In: *ACS Applied Materials & Interfaces* 11.15, pp. 13881–13887.

Gerson, Julian et al. (2023). “High-Precision Monitoring of and Feedback Control over Drug Concentrations in the Brains of Freely Moving Rats”. In: *Science Advances* 9.20, eadg3254.

Gibbons, Frank et al. (2001). “A Dynamical Model of Kinesin-Microtubule Motility Assays”. In: *Biophysical Journal* 80.6, pp. 2515–2526.

Gopinath, Ashwin et al. (2021). “Absolute and Arbitrary Orientation of Single-Molecule Shapes”. In: *Science* 371.6531, eabd6179.

Gosselin, Pierre et al. (2016). “On Complex, Curved Trajectories in Microtubule Gliding”. In: *Physica D: Nonlinear Phenomena*. Nonlinear Models in Molecular and Cell Biology 318–319, pp. 105–111.

Han, Shuo et al. (2019). “Facile and Label-Free Electrochemical Biosensors for MicroRNA Detection Based on DNA Origami Nanostructures”. In: *ACS Omega* 4.6, pp. 11025–11031.

Hancock, William O. and Howard, Jonathon (1998). “Processivity of the Motor Protein Kinesin Requires Two Heads”. In: *The Journal of Cell Biology* 140.6, pp. 1395–1405.

Hansen, Clinton H. et al. (2017). “Nanoswitch-Linked Immunosorbent Assay (NLISA) for Fast, Sensitive, and Specific Protein Detection”. In: *Proceedings of the National Academy of Sciences* 114.39, pp. 10367–10372.

Harmsen, M. M. and De Haard, H. J. (2007). “Properties, Production, and Applications of Camelid Single-Domain Antibody Fragments”. In: *Applied Microbiology and Biotechnology* 77.1, pp. 13–22.

Hegner, Martin, Wagner, Peter, and Semenza, Giorgio (1993). “Ultralarge Atomically Flat Template-Stripped Au Surfaces for Scanning Probe Microscopy”. In: *Surface Science* 291.1, pp. 39–46.

Holliday, Robin (1964). “A Mechanism for Gene Conversion in Fungi”. In: *Genetics Research* 5.2, pp. 282–304.

Hu, Jiaming et al. (2012). “Quantitation of Femtomolar Protein Levels via Direct Readout with the Electrochemical Proximity Assay”. In: *Journal of the American Chemical Society* 134.16, pp. 7066–7072.

Huang, Yike et al. (2018). “A DNA Origami-Based Chiral Plasmonic Sensing Device”. In: *ACS Applied Materials & Interfaces* 10.51, pp. 44221–44225.

Hudoba, Michael W. et al. (2017). “Dynamic DNA Origami Device for Measuring Compressive Depletion Forces”. In: *ACS Nano* 11.7, pp. 6566–6573.

Ibusuki, Ryota et al. (2022). “Programmable Molecular Transport Achieved by Engineering Protein Motors to Move on DNA Nanotubes”. In: *Science* 375.6585, pp. 1159–1164.

Idili, Andrea et al. (2022). “A Programmable Electrochemical Y-Shaped DNA Scaffold Sensor for the Single-Step Detection of Antibodies and Proteins in Untreated Biological Fluids”. In: *Advanced Functional Materials* 32.37, p. 2201881.

Jarczewska, Marta and Malinowska, Elżbieta (2020). “The Application of Antibody–Aptamer Hybrid Biosensors in Clinical Diagnostics and Environmental Analysis”. In: *Analytical Methods* 12.25, pp. 3183–3199.

Jeune-Smith, Yolaine and Hess, Henry (2010). “Engineering the Length Distribution of Microtubules Polymerized in Vitro”. In: *Soft Matter* 6.8, pp. 1778–1784.

Jia, Lili et al. (2004). “Microscale Transport and Sorting by Kinesin Molecular Motors”. In: *Biomedical Microdevices* 6.1, pp. 67–74.

Jones, Matthew R., Seeman, Nadrian C., and Mirkin, Chad A. (2015). “Programmable Materials and the Nature of the DNA Bond”. In: *Science* 347.6224, p. 1260901.

Jorgenson, Tyler D. et al. (2017). “Self-Assembly of Hierarchical DNA Nanotube Architectures with Well-Defined Geometries”. In: *ACS Nano* 11.2, pp. 1927–1936.

Kallenbach, Neville R., Ma, Rong-Ine, and Seeman, Nadrian C. (1983). “An Immobile Nucleic Acid Junction Constructed from Oligonucleotides”. In: *Nature* 305.5937, pp. 829–831.

Kawamura, Ryuzo et al. (2011). “Formation of Motile Assembly of Microtubules Driven by Kinesins”. In: *Smart Materials and Structures* 20.12, p. 124007.

Ke, Yonggang et al. (2012). “Three-Dimensional Structures Self-Assembled from DNA Bricks”. In: *Science* 338.6111, pp. 1177–1183.

Keefe, Anthony D., Pai, Supriya, and Ellington, Andrew (2010). “Aptamers as Therapeutics”. In: *Nature Reviews Drug Discovery* 9.7, pp. 537–550.

Kerssemakers, Jacob et al. (2006). “The Distance That Kinesin-1 Holds Its Cargo from the Microtubule Surface Measured by Fluorescence Interference Contrast Microscopy”. In: *Proceedings of the National Academy of Sciences* 103.43, pp. 15812–15817.

Keya, Jakia Jannat et al. (2018). “DNA-assisted Swarm Control in a Biomolecular Motor System”. In: *Nature Communications* 9.1 (1), p. 453.

Khoshouei, Ali et al. (2024). “Designing Rigid DNA Origami Templates for Molecular Visualization Using Cryo-EM”. In: *Nano Letters* 24.16, pp. 5031–5038.

Kim, Do-Nyun et al. (2012). “Quantitative Prediction of 3D Solution Shape and Flexibility of Nucleic Acid Nanostructures”. In: *Nucleic Acids Research* 40.7, pp. 2862–2868.

Kinoshita, Yoshimi et al. (2018). “Step Sizes and Rate Constants of Single-headed Cytoplasmic Dynein Measured with Optical Tweezers”. In: *Scientific Reports* 8.1, p. 16333.

Klonoff, David C., Ahn, David, and Drincic, Andjela (2017). “Continuous Glucose Monitoring: A Review of the Technology and Clinical Use”. In: *Diabetes Research and Clinical Practice* 133, pp. 178–192.

Koirala, Deepak et al. (2014). “Single-Molecule Mechanochemical Sensing Using DNA Origami Nanostructures”. In: *Angewandte Chemie International Edition* 53.31, pp. 8137–8141.

Komorsky-Lovrić, Šebojka and Lovrić, Milivoj (1995a). “Measurements of Redox Kinetics of Adsorbed Azobenzene by “a Quasireversible Maximum” in Square-Wave Voltammetry”. In: *Electrochimica Acta* 40.11, pp. 1781–1784.

– (1995b). “Square-Wave Voltammetry of Quasi-Reversible Surface Redox Reactions”. In: *Journal of Electroanalytical Chemistry* 384.1–2, pp. 115–122.

Kuzuya, Akinori, Sakai, Yusuke, et al. (2011). “Nanomechanical DNA Origami ’single-Molecule Beacons’ Directly Imaged by Atomic Force Microscopy”. In: *Nature Communications* 2.1 (1), p. 449.

Kuzuya, Akinori, Watanabe, Ryosuke, et al. (2014). “Nanomechanical DNA Origami pH Sensors”. In: *Sensors* 14.10 (10), pp. 19329–19335.

Kuzyk, Anton et al. (2014). “Reconfigurable 3D Plasmonic Metamolecules”. In: *Nature Materials* 13.9, pp. 862–866.

LaBean, Thomas H. et al. (2000). “Construction, Analysis, Ligation, and Self-Assembly of DNA Triple Crossover Complexes”. In: *Journal of the American Chemical Society* 122.9, pp. 1848–1860.

Lai, Rebecca Y., Plaxco, Kevin W., and Heeger, Alan J. (2007). "Aptamer-Based Electrochemical Detection of Picomolar Platelet-Derived Growth Factor Directly in Blood Serum". In: *Analytical Chemistry* 79.1, pp. 229–233.

Leaist, Derek G. (1988). "The Effects of Aggregation, Counterion Binding, and Added NaCl on Diffusion of Aqueous Methylene Blue". In: *Canadian Journal of Chemistry* 66.9, pp. 2452–2457.

Lee, Chong Sung, Davis, Ronald W., and Davidson, Norman (1970). "A Physical Study by Electron Microscopy of the Terminally Repetitious, Circularly Permuted DNA from the Coliphage Particles of *Escherichia Coli* 15". In: *Journal of Molecular Biology* 48.1, pp. 1–22.

Lee, Jae Young, Lee, Jae Gyung, et al. (2021). "Rapid Computational Analysis of DNA Origami Assemblies at Near-Atomic Resolution". In: *ACS Nano* 15.1, pp. 1002–1015.

Levy, Nicolas and Schabanel, Nicolas (2021). "ENSnano: A 3D Modeling Software for DNA Nanostructures". In: *LIPIcs, Volume 205, DNA 27* 205, 5:1–5:23.

Li, Chao, Hu, Xiaolu, et al. (2017). "Design of DNA Nanostructure-Based Interfacial Probes for the Electrochemical Detection of Nucleic Acids Directly in Whole Blood". In: *Chemical Science* 9.4, pp. 979–984.

Li, Jieming, Johnson-Buck, Alexander, et al. (2018). "Exploring the Speed Limit of Toehold Exchange with a Cartwheeling DNA Acrobat". In: *Nature Nanotechnology* 13.8 (8), pp. 723–729.

Li, Zhe, Liu, Minghui, et al. (2010). "Molecular Behavior of DNA Origami in Higher-Order Self-Assembly". In: *Journal of the American Chemical Society* 132.38, pp. 13545–13552.

Lian, Yen-Ling and Lin, Yu-Chun (2024). "The Emerging Tools for Precisely Manipulating Microtubules". In: *Current Opinion in Cell Biology* 88, p. 102360.

Liu, Dage, Park, Sung Ha, et al. (2004). "DNA Nanotubes Self-Assembled from Triple-Crossover Tiles as Templates for Conductive Nanowires". In: *Proceedings of the National Academy of Sciences* 101.3, pp. 717–722.

Liu, Grace Y, Chen, Shiau-Chi, et al. (2022). "Precise Control of Microtubule Disassembly in Living Cells". In: *The EMBO Journal* 41.15, e110472.

Liu, Haiqing, Spoerke, Erik D., et al. (2008). "Biomolecular Motor-Powered Self-Assembly of Dissipative Nanocomposite Rings". In: *Advanced Materials* 20.23, pp. 4476–4481.

Liu, Hao, Matthies, Michael, et al. (2024). "Inverse Design of a Pyrochlore Lattice of DNA Origami through Model-Driven Experiments". In: *Science* 384.6697, pp. 776–781.

Liu, Wenyan, Zhong, Hong, et al. (2011). "Crystalline Two-Dimensional DNA-Origami Arrays". In: *Angewandte Chemie International Edition* 50.1, pp. 264–267.

Love, John J. et al. (1995). "Structural Basis for DNA Bending by the Architectural Transcription Factor LEF-1". In: *Nature* 376.6543, pp. 791–795.

Lubin, Arica A. and Plaxco, Kevin W. (2010). "Folding-Based Electrochemical Biosensors: The Case for Responsive Nucleic Acid Architectures". In: *Accounts of Chemical Research* 43.4, pp. 496–505.

Macfie, Gavin, Atherton, John H., and Compton, Richard G. (2002). "Using Microelectrode Square-Wave Voltammetry to Monitor the Progress of Complex Homogeneous Chemical Reactions". In: *Electroanalysis* 14.7–8, pp. 479–485.

Maffeo, Christopher and Aksimentiev, Aleksei (2020). "MrDNA: A Multi-Resolution Model for Predicting the Structure and Dynamics of DNA Systems". In: *Nucleic Acids Research* 48.9, pp. 5135–5146.

Mahshid, Sahar Sadat, Camiré, Sébastien, et al. (2015). "A Highly Selective Electrochemical DNA-Based Sensor That Employs Steric Hindrance Effects to Detect Proteins Directly in Whole Blood". In: *Journal of the American Chemical Society* 137.50, pp. 15596–15599.

Mahshid, Sara, Mepham, Adam H., et al. (2016). "Mechanistic Control of the Growth of Three-Dimensional Gold Sensors". In: *The Journal of Physical Chemistry C* 120.37, pp. 21123–21132.

Mao, Chengde, Sun, Weiqiong, and Seeman, Nadrian C. (1999). "Designed Two-Dimensional DNA Holliday Junction Arrays Visualized by Atomic Force Microscopy". In: *Journal of the American Chemical Society* 121.23, pp. 5437–5443.

Maune, Hareem T. et al. (2010). "Self-Assembly of Carbon Nanotubes into Two-Dimensional Geometries Using DNA Origami Templates". In: *Nature Nanotechnology* 5.1, pp. 61–66.

Meselson, M S and Radding, C M (1975). "A General Model for Genetic Recombination." In: *Proceedings of the National Academy of Sciences of the United States of America* 72.1, pp. 358–361.

Mihai, Doina Andrada et al. (2021). "Continuous Glucose Monitoring Devices: A Brief Presentation (Review)". In: *Experimental and Therapeutic Medicine* 23.2, p. 174.

Mohammed, Abdul M. and Schulman, Rebecca (2013). "Directing Self-Assembly of DNA Nanotubes Using Programmable Seeds". In: *Nano Letters* 13.9, pp. 4006–4013.

Mohammed, Abdul M., Šulc, Petr, et al. (2017). "Self-Assembling DNA Nanotubes to Connect Molecular Landmarks". In: *Nature Nanotechnology* 12.4 (4), pp. 312–316.

Murphy, R.M. et al. (1988). "Size and Structure of Antigen-Antibody Complexes. Electron Microscopy and Light Scattering Studies". In: *Biophysical Journal* 54.1, pp. 45–56.

Nelson, Aaron L. (2010). "Antibody Fragments: Hope and Hype". In: *mAbs* 2.1, pp. 77–83.

Neupane, Dharmendra and Stine, Keith J. (2021). "Electrochemical Sandwich Assays for Biomarkers Incorporating Aptamers, Antibodies and Nanomaterials for Detection of Specific Protein Biomarkers". In: *Applied Sciences* 11.15 (15), p. 7087.

Ni, Heng et al. (2022). "Direct Visualization of Floppy Two-Dimensional DNA Origami Using Cryogenic Electron Microscopy". In: *iScience* 25.6, p. 104373.

Niu, Lin et al. (2016). "Effects of Structural Flexibility on the Kinetics of DNA Y-Junction Assembly and Gelation". In: *Langmuir* 32.48, pp. 12862–12868.

Nordén, Bengt and Tjerneld, Folke (1982). "Structure of methylene blue–DNA complexes studied by linear and circular dichroism spectroscopy". In: *Biopolymers* 21.9, pp. 1713–1734.

Oktay, Esra et al. (2023). "DNA Origami Presenting the Receptor Binding Domain of SARS-CoV-2 Elicit Robust Protective Immune Response". In: *Communications Biology* 6.1, pp. 1–11.

Ouldridge, Thomas E., Louis, Ard A., and Doye, Jonathan P. K. (2011). "Structural, Mechanical, and Thermodynamic Properties of a Coarse-Grained DNA Model". In: *The Journal of Chemical Physics* 134.8, p. 085101.

Owczarzy, Richard et al. (2008). "Predicting Stability of DNA Duplexes in Solutions Containing Magnesium and Monovalent Cations". In: *Biochemistry* 47.19, pp. 5336–5353.

Pandey, Richa et al. (2021). “Integrating Programmable DNAzymes with Electrical Readout for Rapid and Culture-Free Bacterial Detection Using a Handheld Platform”. In: *Nature Chemistry* 13.9 (9), pp. 895–901.

Pei, Hao et al. (2011). “Regenerable Electrochemical Immunological Sensing at DNA Nanostructure-Decorated Gold Surfaces”. In: *Chemical Communications* 47.22, p. 6254.

Pellitero, Miguel Aller, Shaver, Alexander, and Arroyo-Currás, Netzahualcóyotl (2019). “Critical Review—Approaches for the Electrochemical Interrogation of DNA-Based Sensors: A Critical Review”. In: *Journal of The Electrochemical Society* 167.3, p. 037529.

Pensa, Evangelina et al. (2022). “Single DNA Origami Detection by Nanoimpact Electrochemistry”. In: *ChemElectroChem* 9.4, e202101696.

Phillips, James C. et al. (2020). “Scalable Molecular Dynamics on CPU and GPU Architectures with NAMD”. In: *The Journal of Chemical Physics* 153.4, p. 044130.

Pitikultham, Piyawat et al. (2022). “Stimuli-Responsive DNA Origami Nanodevices and Their Biological Applications”. In: *ChemMedChem* 17.1, e202100635.

Poppleton, Erik et al. (2020). “Design, Optimization and Analysis of Large DNA and RNA Nanostructures through Interactive Visualization, Editing and Molecular Simulation”. In: *Nucleic Acids Research* 48.12, e72.

Qian, Lulu, Soloveichik, David, and Winfree, Erik (2011). “Efficient Turing-Universal Computation with DNA Polymers”. In: *Lecture Notes in Computer Science (including subseries Lecture Notes in Artificial Intelligence and Lecture Notes in Bioinformatics)* 6518 LNCS, pp. 123–140.

Radding, Charles M. et al. (1977). “Uptake of Homologous Single-Stranded Fragments by Superhelical DNA: IV. Branch Migration”. In: *Journal of Molecular Biology* 116.4, pp. 825–839.

Rangel, Alexandra E. et al. (2020). “Engineering Aptamer Switches for Multifunctional Stimulus-Responsive Nanosystems”. In: *Advanced Materials* 32.50, p. 2003704.

Reck-Peterson, Samara L. et al. (2006). “Single-Molecule Analysis of Dynein Processivity and Stepping Behavior”. In: *Cell* 126.2, pp. 335–348.

Ross, Tyler D. et al. (2022). “Ray Optics for Gliders”. In: *ACS Nano* 16.10, pp. 16191–16200.

Rothemund, Paul W. K. (2006). “Folding DNA to Create Nanoscale Shapes and Patterns”. In: *Nature* 440.7082, pp. 297–302.

Rothemund, Paul W. K. et al. (2004). “Design and Characterization of Programmable DNA Nanotubes”. In: *Journal of the American Chemical Society* 126.50, pp. 16344–16352.

Sample, Matthew et al. (2024). “Hairygami: Analysis of DNA Nanostructures’ Conformational Change Driven by Functionalizable Overhangs”. In: *ACS Nano* 18.43, pp. 30004–30016.

Schickinger, Matthias, Zacharias, Martin, and Dietz, Hendrik (2018). “Tethered Multifluorophore Motion Reveals Equilibrium Transition Kinetics of Single DNA Double Helices”. In: *Proceedings of the National Academy of Sciences* 115.32, E7512–E7521.

Schmidt, Helgo et al. (2015). “Structure of Human Cytoplasmic Dynein-2 Primed for Its Power Stroke”. In: *Nature* 518.7539, pp. 435–438.

Scott, Alexander et al. (2022). “A Smartphone Operated Electrochemical Reader and Actuator That Streamlines the Operation of Electrochemical Biosensors”. In: *ECS Sensors Plus* 1.1, p. 014601.

Seeman, Nadrian C. (1982). “Nucleic Acid Junctions and Lattices”. In: *Journal of Theoretical Biology* 99.2, pp. 237–247.

Seeman, Nadrian C. and Sleiman, Hanadi F. (2017). “DNA Nanotechnology”. In: *Nature Reviews Materials* 3.1, pp. 1–23.

Selnihhin, Denis et al. (2018a). “Multifluorophore DNA Origami Beacon as a Biosensing Platform”. In: *ACS Nano* 12.6, pp. 5699–5708.

– (2018b). “Multifluorophore DNA Origami Beacon as a Biosensing Platform”. In: *ACS Nano* 12.6, pp. 5699–5708.

Shaver, Alexander, Curtis, Samuel D., and Arroyo-Currás, Netzahualcóyotl (2020). “Alkanethiol Monolayer End Groups Affect the Long-Term Operational Stability and Signaling of Electrochemical, Aptamer-Based Sensors in Biological Fluids”. In: *ACS Applied Materials & Interfaces* 12.9, pp. 11214–11223.

Shen, Luyao, Wang, Pengfei, and Ke, Yonggang (2021). “DNA Nanotechnology-Based Biosensors and Therapeutics”. In: *Advanced Healthcare Materials* 10.15, p. 2002205.

Shen, Qi, Feng, Qingzhou, et al. (2023). “Modeling HIV-1 Nuclear Entry with Nucleoporin-Gated DNA-origami Channels”. In: *Nature Structural & Molecular Biology* 30.4, pp. 425–435.

Shrestha, Prakash et al. (2021). “Single-Molecule Mechanical Fingerprinting with DNA Nanoswitch Calipers”. In: *Nature Nanotechnology* 16.12, pp. 1362–1370.

Simmel, Friedrich C., Yurke, Bernard, and Singh, Hari R. (2019). “Principles and Applications of Nucleic Acid Strand Displacement Reactions”. In: *Chemical Reviews* 119.10, pp. 6326–6369.

Slattery, Matthew et al. (2014). “Absence of a Simple Code: How Transcription Factors Read the Genome”. In: *Trends in Biochemical Sciences* 39.9, pp. 381–399.

Snodin, Benedict E. K. et al. (2015). “Introducing Improved Structural Properties and Salt Dependence into a Coarse-Grained Model of DNA”. In: *The Journal of Chemical Physics* 142.23, p. 234901.

Soheilypour, Mohammad et al. (2015). “Buckling Behavior of Individual and Bundled Microtubules”. In: *Biophysical Journal* 108.7, pp. 1718–1726.

Somasundaram, Subramaniam and Easley, Christopher J. (2019). “A Nucleic Acid Nanostructure Built through On-Electrode Ligation for Electrochemical Detection of a Broad Range of Analytes”. In: *Journal of the American Chemical Society*.

Stoltenburg, Regina, Nikolaus, Nadia, and Strehlitz, Beate (2012). “Capture-SELEX: Selection of DNA Aptamers for Aminoglycoside Antibiotics”. In: *Journal of Analytical Methods in Chemistry* 2012.1, p. 415697.

Šulc, Petr et al. (2012). “Sequence-Dependent Thermodynamics of a Coarse-Grained DNA Model”. In: *The Journal of Chemical Physics* 137.13, p. 135101.

Suma, Antonio et al. (2019). “TacoxDNA: A User-friendly Web Server for Simulations of Complex DNA Structures, from Single Strands to Origami”. In: *Journal of Computational Chemistry* 40.29, pp. 2586–2595.

Sun, Huidan et al. (2018). “Electrochemical Sandwich Immunoassay for Insulin Detection Based on the Use of Gold Nanoparticle-Modified MoS2 Nanosheets and the Hybridization Chain Reaction”. In: *Microchimica Acta* 186.1, p. 6.

Tang, Marco S. L. et al. (2018). "An Aptamer-Enabled DNA Nanobox for Protein Sensing". In: *Nanomedicine: Nanotechnology, Biology and Medicine* 14.4, pp. 1161–1168.

Thubagere, Anupama J. et al. (2017). "A Cargo-Sorting DNA Robot". In: *Science* 357.6356.

Tikhomirov, Grigory, Petersen, Philip, and Qian, Lulu (2017). "Fractal Assembly of Micrometre-Scale DNA Origami Arrays with Arbitrary Patterns". In: *Nature* 552.7683, pp. 67–71.

– (2018). "Triangular DNA Origami Tilings". In: *Journal of the American Chemical Society* 140, jacs.8b10609.

Uzawa, Takanori et al. (2010). "A Mechanistic Study of Electron Transfer from the Distal Termini of Electrode-Bound, Single-Stranded DNAs". In: *Journal of the American Chemical Society* 132.45, pp. 16120–16126.

Vaisocherová, Hana, Brynda, Eduard, and Homola, Jiří (2015). "Functionalizable Low-Fouling Coatings for Label-Free Biosensing in Complex Biological Media: Advances and Applications". In: *Analytical and Bioanalytical Chemistry* 407.14, pp. 3927–3953.

VanDelinder, Virginia, Imam, Zachary I., and Bachand, George (2019). "Kinesin Motor Density and Dynamics in Gliding Microtubule Motility". In: *Scientific Reports* 9.1, p. 7206.

Van Mameren, Joost et al. (2009). "Leveraging Single Protein Polymers to Measure Flexural Rigidity". In: *The Journal of Physical Chemistry. B* 113.12, pp. 3837–3844.

Vardevanyan, P. O. et al. (2013). "Mechanisms for Binding between Methylene Blue and DNA". In: *Journal of Applied Spectroscopy* 80.4, pp. 595–599.

Verma, Vikash, Wadsworth, Patricia, and Maresca, Thomas J. (2024). "Human Dynein-Dynactin Is a Fast Processive Motor in Living Cells". In: *eLife* 13.

Vu, Cong Quang et al. (2017). "Oligonucleotide Hybridization Combined with Competitive Antibody Binding for the Truncation of a High-Affinity Aptamer". In: *ACS Combinatorial Science* 19.10, pp. 609–617.

Wada, Akira (2013). "Development of Next-Generation Peptide Binders Using In Vitro Display Technologies and Their Potential Applications". In: *Frontiers in Immunology* 4, p. 224.

Wagenbauer, Klaus F., Sigl, Christian, and Dietz, Hendrik (2017). "Gigadalton-Scale Shape-Programmable DNA Assemblies". In: *Nature* 552.7683, pp. 78–83.

Wang, Shuang et al. (2020). "DNA Origami-Enabled Biosensors". In: *Sensors (Basel, Switzerland)* 20.23, p. 6899.

Watkins, Zach et al. (2023). "Week-Long Operation of Electrochemical Aptamer Sensors: New Insights into Self-Assembled Monolayer Degradation Mechanisms and Solutions for Stability in Serum at Body Temperature". In: *ACS Sensors* 8.3, pp. 1119–1131.

Watson, Jeffrey, Hays, Franklin A., and Ho, P. Shing (2004). "Definitions and Analysis of DNA Holliday Junction Geometry". In: *Nucleic Acids Research* 32.10, pp. 3017–3027.

Wei, Bryan, Dai, Mingjie, and Yin, Peng (2012). "Complex Shapes Self-Assembled from Single-Stranded DNA Tiles". In: *Nature* 485.7400 (7400), pp. 623–626.

Weiss, Emily A. et al. (2007). "Si/SiO2-Templated Formation of Ultraflat Metal Surfaces on Glass, Polymer, and Solder Supports: Their Use as Substrates for Self-Assembled Monolayers". In: *Langmuir* 23.19, pp. 9686–9694.

White, Ryan J. and Plaxco, Kevin W. (2010). "Exploiting Binding-Induced Changes in Probe Flexibility for the Optimization of Electrochemical Biosensors". In: *Analytical chemistry* 82.1, pp. 73–76.

White, Ryan J., Rowe, Aaron A., and Plaxco, Kevin W. (2010). "Re-Engineering Aptamers to Support Reagentless, Self-Reporting Electrochemical Sensors". In: *Analyst* 135.3, pp. 589–594.

Wild, David, ed. (2013). *The Immunoassay Handbook (Fourth Edition)*. Oxford: Elsevier.

Williamson, Paul, Ijäs, Heini, et al. (2021). "Probing the Conformational States of a pH-Sensitive DNA Origami Zipper via Label-Free Electrochemical Methods". In: *Langmuir* 37.25, pp. 7801–7809.

Williamson, Paul, Piskunen, Petteri, et al. (2023). "Signal Amplification in Electrochemical DNA Biosensors Using Target-Capturing DNA Origami Tiles". In: *ACS Sensors* 8.4, pp. 1471–1480.

Wintersinger, Christopher M. et al. (2023). "Multi-Micron Crisscross Structures Grown from DNA-origami Slats". In: *Nature Nanotechnology* 18.3, pp. 281–289.

Woo, Sungwook and Rothemund, Paul W. K. (2011). "Programmable Molecular Recognition Based on the Geometry of DNA Nanostructures". In: *Nature Chemistry* 3.8 (8), pp. 620–627.

– (2014). "Self-Assembly of Two-Dimensional DNA Origami Lattices Using Cation-Controlled Surface Diffusion". In: *Nature Communications* 5.1, p. 4889.

Woods, Damien et al. (2019). "Diverse and Robust Molecular Algorithms Using Reprogrammable DNA Self-Assembly". In: *Nature* 567.7748 (7748), pp. 366–372.

Wu, Juncen, Liu, Yuqing, et al. (2023). "A New Generation of Sensors for Non-Invasive Blood Glucose Monitoring". In: *American Journal of Translational Research* 15.6, p. 3825.

Wu, Yuyang, Ranallo, Simona, et al. (2023). "Using Spectroscopy to Guide the Adaptation of Aptamers into Electrochemical Aptamer-Based Sensors". In: *Bioconjugate Chemistry* 34.1, pp. 124–132.

Xiao, Yi, Lubin, Arica A., Baker, Brian R., et al. (2006). "Single-Step Electronic Detection of Femtomolar DNA by Target-Induced Strand Displacement in an Electrode-Bound Duplex". In: *Proceedings of the National Academy of Sciences* 103.45, pp. 16677–16680.

Xiao, Yi, Lubin, Arica A., Heeger, Alan J., et al. (2005). "Label-Free Electronic Detection of Thrombin in Blood Serum by Using an Aptamer-Based Sensor". In: *Angewandte Chemie International Edition* 44.34, pp. 5456–5459.

Xiao, Yi, Piorek, Brian D., et al. (2005). "A Reagentless Signal-On Architecture for Electronic, Aptamer-Based Sensors via Target-Induced Strand Displacement". In: *Journal of the American Chemical Society* 127.51, pp. 17990–17991.

Xuan, Jinnan et al. (2023). "Engineering of Interfaces with Tetrahedra DNA Nanostructures for Biosensing Applications". In: *Analysis & Sensing* 3.5, e202200100.

Yan, Hao et al. (2003). "DNA-Templated Self-Assembly of Protein Arrays and Highly Conductive Nanowires". In: *Science* 301.5641, pp. 1882–1884.

Yang, Kyung-Ae, Pei, Renjun, and Stojanovic, Milan N. (2016). "*In Vitro* Selection and Amplification Protocols for Isolation of Aptameric Sensors for Small Molecules". In: *Methods*. In Vitro Selection and Evolution 106, pp. 58–65.

Yin, Peng et al. (2008). “Programming DNA Tube Circumferences”. In: *Science* 321.5890, pp. 824–826.

Yun, Minseong et al. (2014). “Stable Organic Field-Effect Transistors for Continuous and Nondestructive Sensing of Chemical and Biologically Relevant Molecules in Aqueous Environment”. In: *ACS Applied Materials & Interfaces* 6.3, pp. 1616–1622.

Yurke, Bernard et al. (2000). “A DNA-fuelled Molecular Machine Made of DNA”. In: *Nature* 406.6796 (6796), pp. 605–608.

Zeng, Yang C. et al. (2024). “Fine Tuning of CpG Spatial Distribution with DNA Origami for Improved Cancer Vaccination”. In: *Nature Nanotechnology* 19.7, pp. 1055–1065.

Zettl, Thomas et al. (2020). “The Structural Ensemble of a Holliday Junction Determined by X-ray Scattering Interference”. In: *Nucleic Acids Research* 48.14, pp. 8090–8098.

Zhang, David Yu, Hariadi, Rizal F., et al. (2013). “Integrating DNA Strand-Displacement Circuitry with DNA Tile Self-Assembly”. In: *Nature Communications* 4.1, p. 1965.

Zhang, Fei, Jiang, Shuoxing, et al. (2015). “Complex Wireframe DNA Origami Nanostructures with Multi-Arm Junction Vertices”. In: *Nature Nanotechnology* 10.9, pp. 779–784.

Zhang, Jichun, Huang, Yue, et al. (2005). “Electrochemical Array Microsystem with Integrated Potentiostat”. In: *2005 IEEE SENSORS*. 2005 IEEE SENSORS.

Zhang, Yang, Lai, Bo Shiun, and Juhas, Mario (2019). “Recent Advances in Aptamer Discovery and Applications”. In: *Molecules* 24.5 (5), p. 941.

Zhou, Chao et al. (2018). “Dynamic Plasmonic System That Responds to Thermal and Aptamer-Target Regulations”. In: *Nano Letters* 18.11, pp. 7395–7399.

Zwang, Theodore J., Tse, Edmund C. M., and Barton, Jacqueline K. (2018). “Sensing DNA through DNA Charge Transport”. In: *ACS Chemical Biology* 13.7, pp. 1799–1809.

Appendix A

SQUARE WAVE VOLTAMMETRY

The voltage profile of a single square wave voltammetry measurement is shown at left. A step function is superimposed on a slower voltage ramp and an electric current is measured on both ends (i_{for} and i_{rev}) of each step. The difference Δi between these two currents, as a function of E is the raw IV Data. To compensate for a tilted, rising baseline at more negative voltage (due to oxygen reduction) the raw IV data is processed as follows. A first approximation to the tilted baseline is made by drawing a line between the current measured at -0.18 V and at -0.40 V of the raw data. This line is then subtracted from the data, to compensate roughly for the tilted baseline. The left and right shoulders of the resulting curve are smoothed with a 7-point moving average, and the maxima of each of these shoulders is found, resulting in a pair of voltages, V_l and V_r, which define the voltage range for data processing. The currents in the original IV data at V_l and V_r are used to define a better approximation to the tilted baseline, and this is subtracted from the raw data. This new baseline-subtracted data is fit to a Gaussian curve (between V_l and V_r). The peak height is defined as the maximum current of this Gaussian fitted curve. The open state of the sensor (black curve) provides a baseline for each experimental condition wherein we expect some fraction of the sensors to be closed (red curve). To determine the sensor signal for a particular experimental condition, the baseline and experimental curves are fit with Gaussians and their peaks are found. The sensor signal or peak current is then defined as Δi_{peak}, the difference between the Δi for the respective peaks of the two curves.

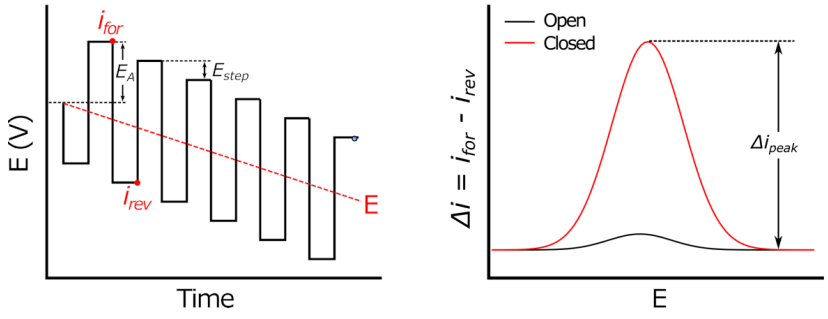

Figure A.1: Square wave voltammetry

Appendix B

NOTES ON TRANSLATING ELECTRICAL CURRENTS TO CONCENTRATIONS

Sensors that employ an electrochemical readout method, such as EDNA, E-AB, or our lilypad detector, need a way to convert the measured electrical current to an analyte concentration value in order to be quantitative. If initially one might be tempted to directly link an absolute current value to a concentration, the architecture and fabrication of the sensor can play an important role in the measured values. For example, both the off and on signal are reasonably supposed to be proportional to the number of the detectors on the electrode. While obviously using a larger electrode would result in higher electrical currents, even our current fabrication methods can cause significant chip-to-chip differences. For example, the size of our electrode is effectively determined by the silicone gasket that we stick on the template-stripped gold surface, and the aperture of the gasket is affected by how strongly it is manually pressed on the chip, creating intrinsic and inevitable variability. Different batches of DNA lilypad origami, thiolated linkers, or passivation agents will also result in variability of the density of detectors on the surface, further decreasing the meaning of absolute current values. Throughout most of the EDNA/E-AB literature, an approach called Kinetic Differential Measurements (KDM) has proven successful (Arroyo-Currás, Dauphin-Ducharme, et al., 2020; Ferguson et al., 2013). Here a sensor is interrogated with square wave voltammetry at multiple frequencies in both the on and off state, similarly to what we showed in Section 2.11. The frequency that yields the highest SWV signal is dependent on electron transfer rate and it will thus change between the on and off state. By looking at these two curves (square wave voltammetry peak over frequency for both off and on signal), the measurement frequencies are chosen as the ones that maximize the contrast between the two states (there will thus be an "on frequency" and an "off frequency"). The current is then measured as the difference of two relative currents. The first term is the current measured at the on frequency after target addition normalized by the current at the on frequency when no target is added, the second term is the same current fraction, but measured at the off frequency. The off frequency is historically found to be lower than the on frequency, as the electron transfer rate should be lower when no analyte is present. Alternatively the off frequency can be replaced by a second "off"

electrode that is not responsive to the target, but is just as sensitive to background and degradation, an approach that has been used to calibrate *in vivo* E-AB sensors Arroyo-Currás, Somerson, et al., 2017. However, in our design the electron transfer rate appears to be at the low end of the frequency spectrum even in the on state, and we were not able to find a lower "off" frequency. We employ a variant of this approach in Section 2.7, where we divide the on signal by the off signal. However, there are systems where the off signal is so low to be effectively indistinguishable from the noise floor of the instrument (for example Hu et al., 2012) where such an approach cannot be employed as it is effectively impossible to measure an off signal. The lilypad detector lies somewhere in between these two cases, with an off signal that is effectively very low at 10^{-10} A, but still measurable.

In our experience, we often observed both off and on signals to be very reproducible without needing to normalize each reading. Given the relatively high gain measured in our system compared to EDNA detectors, we found that even with comparable absolute on signals, small fluctuations in off signal could result in large fluctuations in relative increase, suggesting that KDM could yield a sensor curve that cannot distinguish between different concentrations when applied to different chips. There are indeed physical reproducibility issues that can disproportionately affect the off signal and not contribute to the on signal. The most obvious one, and one we controlled for, is temperature. We believe that in the off state, where detectors are tethered to the surface through the double-stranded linker but somewhat free to diffuse in solution, the signal we read comes mostly from collisions with the surface due to Brownian motion. Their rate, and thus the off signal, is highly dependent on temperature, but in the on state most of the signal comes from detectors closed on the surface through analyte binding, a phenomenon where temperature plays almost no role at equilibrium.

To give a more complete picture of the behavior of our sensor, we have chosen to use absolute values when studying its geometry and properties, as we found that many design parameters have an effect on both the off and on signal. However, we have not yet settled on a definitive way to translate currents to concentrations, and we have shown advantages and disadvantages of either approach. A more complete answer would require further studies and a deeper understanding of the physical origins of chip-to-chip variability.

Appendix C

SYNTHESIS OF DOUBLE-STRANDED DNA LINKERS FOR LILY PAD STALKS

Linkers were created via two rounds of the polymerase chain reaction (PCR). The first (extension) round allowed selection of the length of the final linker (from a 48 kb Lambda DNA template) and added appropriate primers for the next round. The second round, an autosticky (Gál et al., 1999), used primers with 40 or 47 nt extensions blocked by abasic sites; polymerase encountering these abasic sites dissociated from the templates without extending to the end of the primers, thus leaving a single-stranded tail at each end of an otherwise dsDNA linker.

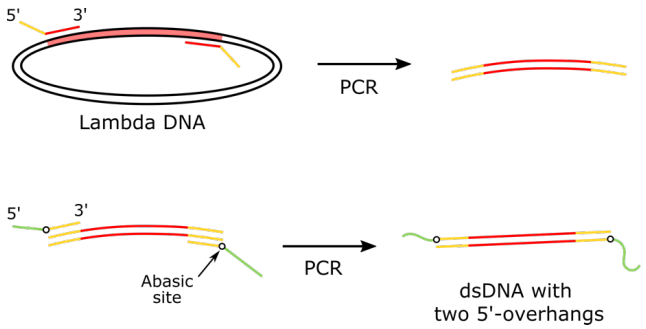

Figure C.1: **Synthesis of dsDNA linkers for lily pad stalks. Top:** a first round of PCR was performed with a pair of primers designed to selectively amplify a subsection of Lambda DNA, having a particular length. **Bottom:** a second round of PCR with primers designed to add single-stranded overhangs was performed. An abasic site between primer sequence and the green single-stranded overhangs caused polymerase to dissociate.

Name	Sequences
ForPr-extension	CTACTTAGATTGCCACGCATCTGCCTAGGAATTGGTTAGC
RevPr-252bp-extension	GTAGCATCAGGAATCTGAACGTTTCAGCAGCTACAGTCAG
RevPr-957bp-extension	GTAGCATCAGGAATCTGAACATGCTCGGAAGGTATGATGC
RevPr-2903bp-extension	GTAGCATCAGGAATCTGAACAAGTCCGTGGCTATCTATCG
ForPr-idSp-DSbind	CACCATCAATATGATATTCAATTTAAATTGTAAACGTTA ATATTTTT/idSp/CTACTTAGATTGCCACGCAT
RevPr-idSp-40ntOH	CGGTGGGAGTATTCATCGTGGTGAAGACGCTGGGTTTACG/idSp/GTA GCATCAGGAATCTGAAC

Table C.1: **Names and sequences of primers used for synthesis of different lengths of dsDNA linkers for lily pad stalks.**

Name	Sequences
14nt binder 5' extension on origami (top)	TCCGTACCATTCAG
14nt binder 3' anchored on surface (bottom)	thiol-TTTTT AGCTTTGATATCTG
28nt DNA analyte *xy*	CTGAATGGTACGGA CAGATATCAAAGCT
28nt DNA analyte *yx*	CAGATATCAAAGCT CTGAATGGTACGGA
28nt DNA analyte *dT28*	TTTTTTTTTTTTTT TTTTTTTTTTTTTT
20 nt 5′ staple extension; binds 20 nt MB reporters	GTTGTAGTGGTATGAGGTTG
20 nt 3′ MB-functionalized; for 20 nt MB curtain	CAACCTCATACCACTACAAC-MB
40 nt binder for dsDNA linker on surface (bottom)	CGTAAACCCAGCGTCTTCACCACGATGAATA CTCCCACCGTTTTT-thiol
Biotin strand with 5nt toehold (top)	CTGAATGGTACGGA-CAACG-biotin
Biotin strand with 5nt toehold (bottom)	biotin-CCATC-CAGATATCAAAGCT
Invader strand (top)	CGTTGTCCGTACCATTCAG
Invader strand (bottom)	AGCTTTGATATCTGGATGG
PDGF-BB-Aptamer (top)	CTGAATGGTACGGA CAGGCTACGGCACGTAGAGCAT CACCATGATCCTG
PDGF-BB-Aptamer (bottom)	CAGGCTACGGCACGTAGAGCATCACCATGATCCTG CA GATATCAAAGCT

Table C.2: **Names and sequences of strands having various functional roles for the lily pad sensors.** Strands labeled with "bottom" are used on the surface side of the sensor; strands labeled with "top" are used on the origami side of the sensor.